Université de Montréal

SEARCH FOR RESONANT WZ PRODUCTION IN THE FULLY LEPTONIC FINAL STATE WITH THE ATLAS DETECTOR

par
Benjamin Freund

Département de physique
Faculté des arts et des sciences

Thèse présentée à la Faculté des études supérieures
en vue de l'obtention du grade de Philosophiæ Doctor (Ph.D.)
en physique

Juillet, 2019

Université de Montréal
Faculté des études supérieures

Cette thèse intitulée:

SEARCH FOR RESONANT WZ PRODUCTION IN THE FULLY LEPTONIC FINAL STATE WITH THE ATLAS DETECTOR

présentée par:

Benjamin Freund

a été évaluée par un jury composé des personnes suivantes:

François Schiettekatte,	président-rapporteur
Georges Azuelos,	directeur de recherche
Jean-François Arguin,	codirecteur
Leroy Claude,	membre du jury
Simon Viel,	examinateur externe

Thèse acceptée le: . . . . . .

RÉSUMÉ

Les recherches de résonances di-boson constituent un test essentiel des théories de brisure de symétrie électrofaible au-delà du modèle standard (MS). Plusieurs scénarios, comme les théories de grande unification, les modèles Little Higgs, les modèles de Higgs Composés ou celles avec un secteur de Higgs élargi (par example SUSY ou le two-Higgs-doublet model), prédisent des résonances vectorielles ou scalaires. Cette thèse présente une recherche de résonances lourdes se désintégrant en WZ dans le canal leptonique $WZ \to \ell\nu\,\ell\ell$ ($\ell = e$ ou μ). Deux modes de production sont considérés : par fusion de quark-antiquark ou par fusion de boson vectoriels. Se basant sur les récentes données recueillies par le détecteur ATLAS lors de collisions pp à 13 TeV au LHC au cours des années 2015 et 2016, avec une luminosité intégrée de 36.1 fb^{-1}, on établira des contraintes sur des modèles allant au-delà du MS de la physique des particules.

Puisqu'on considère la désintégration leptonique des bosons WZ, on sélectionne les événements ayant trois leptons et une grande énergie transverse manquante. Des régions de signal sont choisies pour chaque mode de production : fusion par quarks ou par bosons vectoriels. Pour les résonances produites par fusion de quark, on considère des résonances vectorielles lourdes. On sélectionne donc des événements où les boson W et Z portent une fraction importante de l'énergie de masse de la résonance ($p_{\mathrm{T}}^{W}/m_{WZ} > 0.35$ et $p_{\mathrm{T}}^{Z}/m_{WZ} > 0.35$). Les résonances produites par fusion de bosons sont caractérisées par deux jets ayant une grande séparation en pseudorapidité et une grande masse invariante. Pour la région de signal, dans ce cas, on requiert alors au moins deux jets avec une masse invariante supérieure à $m_{jj} > 500$ GeV et une grande séparation en pseudorapidité $|\Delta\eta_{jj}| > 3.5$. Pour les deux régions, la distribution en masse invariante du système WZ sera examinée pour déterminer la présence ou non de nouvelles résonances qui se manifesteraient par un excès localisé.

En fin de compte, aucun excès significatif n'a été observé dans les régions de signal, ce qui permet d'établir des limites sur le produit de la section efficace et du rapport d'embranchement d'un boson massif vectoriel dans les deux canaux de production. Des contraintes sont également obtenues sur la masse et le couplage d'un boson de Higgs

chargé du modèle Georgi-Machacek, produites par fusion de bosons vectoriels.

Mots clés: Physique des particules, ATLAS, VBS, VBF, bosons de jauge, brisure de symétrie électrofaible

ABSTRACT

Diboson resonance searches are an essential test of electroweak symmetry breaking theories beyond the Standard Model (SM) of particle physics. Vector or scalar resonances decaying to dibosons are predicted by various models going beyond the SM, such as Grand Unified theories, Little Higgs models, Composite Higgs models or models with extended Higgs sector (such as Super Symmetry (SUSY) or two-Higgs-doublet models). This thesis presents a search for resonant WZ production in the fully leptonic decay channel $\ell\nu\ \ell\ell$ ($\ell = e$ or μ) with two production modes : quark-antiquark fusion or vector-boson fusion. Using 36.1 fb^{-1} of recent data collected by the ATLAS detector in pp collisions delivered by the Large Hadron Collider (LHC) at 13 TeV, constraints are obtained on models going beyond the SM.

Since this analysis considers the fully leptonic decays of the vector bosons, events with exactly three leptons in the final state and a substantial missing transverse energy are selected. One signal region is established for each production mode of the resonance, either by quark-antiquark or vector boson fusion. For heavy vectorial resonances produced by quark fusion the W and Z bosons are required to carry a substantial fraction of the resonance energy ($p_{\mathrm{T}}^{W}/m_{WZ} > 0.35$ and $p_{\mathrm{T}}^{Z}/m_{WZ} > 0.35$)). Events with resonances produced by vector boson fusion are characterised by two jets with a large invariant mass and a large separation in pseudorapidity. Therefore, in the search for this production mode, events are required to have at least two jets with an invariant mass (m_{jj}) greater than 500 GeV and a separation in pseudorapidity ($\Delta\eta_{jj}$) of at least $|\Delta\eta_{jj}| > 3.5$. In each signal region the distribution of the invariant mass of the WZ system will then be examined to determine the presence or absence of new resonances that manifest themselves as localised excesses in the invariant mass of the diboson system (m_{WZ}).

No significant excess was observed in the signal regions. Limits have then been set on the cross section times branching ratio for a heavy vector resonance produced by either quark-antiquark or vector boson fusion. Additionally, limits on the coupling parameters and masses are obtained for a charged Higgs boson in the Georgi-Machacek produced by vector boson fusion.

Keywords : Particle physics, ATLAS, VBS, VBF, Gauge Bosons, Electroweak Symmetry Breaking.

CONTENTS

LIST OF TABLES

LIST OF FIGURES

ACRONYMES

$\upsilon ev\upsilon$ vacuum expectation value. xiii, 10, 22, 29

ALICE A Large Ion Collider Experiment. 32

ANN Artificial Neural Network. xi, xii, xxi, 109, 114, 115, 116, 118, 119, 121

ATLAS A Large LHC ApparatuS. xiii, xiv, xxviii, 1, 2, 12, 32, 33, 34, 35, 36, 37, 38, 40, 41, 42, 44, 47, 49, 50, 51, 52, 57, 59, 60, 72, 73, 101, 103, 123, 126, 127

BDT Boosted Decision Tree. xxi, 65, 109, 112, 114, 118, 119, 121, 123

BSM Beyond Standard Model. 23

CERN Conseil Européen pour la Recherche Nucléaire. 12, 32, 42

CMS Compact Muon Spectrometer. xix, 1, 2, 12, 32, 57, 59, 101, 103

CPU Central Processing Unit. 60

DAQ data acquisition. 42

EF event filter. 41, 42

EM electromagnetic. 40, 41, 43

EW electroweak. xv, xix, 12, 57, 84, 103, 105

EWSB electroweak symmetry breaking. 1, 2, 12, 13, 22, 23

GM Georgi-Machacek. xi, xii, xv, xvi, xix, xxi, xxix, 1, 2, 28, 30, 57, 59, 63, 70, 71, 88, 95, 98, 101, 103, 108, 115, 121, 123, 126, 127

HL-LHC High Luminosity LHC. 50, 51

HVT Heavy Vector Triplet. xi, xv, xvi, xviii, xix, xx, xxix, 1, 57, 62, 63, 71, 72, 73, 86, 88, 95, 98, 103, 105, 106, 115, 123, 126, 127

IBL Insertable B-Layer. xiv, xxviii, 37, 38

ID Inner Detector. 37, 38, 40, 43

IP Interaction Point. 35

ITk Inner Tracker. xiv, xxviii, 49, 51, 52, 56

L1 Level-1 trigger. 41, 42

L2 Level-2 trigger. 41, 42

LAr liquid Argon. 40

LEP Large Electron-Positron Collider. 4, 12, 32

LH likelihood-based. 43

LHC Large Hadron Collider. v, xiii, xiv, 1, 2, 4, 8, 13, 15, 17, 25, 26, 30, 32, 33, 34, 35, 38, 42, 45, 49, 50, 51, 52, 59, 127

LHCb LHC Beauty. 32

LO leading order. xxi, 61, 86, 108, 123

LS2 Long Shutdown 2. 49, 50

MC Monte Carlo. xv, xvi, xix, 2, 60, 61, 66, 68, 72, 73, 74, 75, 77, 78, 83, 84, 86, 90, 94, 101, 108

MCHM Minimal Composite Higgs Model. 1, 20, 21, 23, 126

ML maximum likelihood. 92, 93

MLP Multi-Layer Perceptron. 109

MS Muon Spectrometer. 40

MVA Multivariate Analysis. 2, 108, 109, 127

NAG Nesterov's Accelerated Gradient. 116, 117

NLO Next-to-leading order. xii, xxi, xxix, 61, 63, 108, 121, 123, 127

NNLO Next-to-next-to-leading order. 61, 62

NSW New Small Wheel. 50

PDF probability density function. xi, xvii, 43, 62, 79, 82, 84, 86, 88, 93, 95

PDF parton distribution function. xiii, 8

QCD Quantum Chromodynamics. xv, 4, 5, 8, 12, 17, 18, 20, 35, 57, 61, 70, 79, 82, 84

QED Quantum Electrodynamics. 9

RoI Regions-of-Interest. 41, 42

RPC Resistive Plate Chamber. 41

SCT silicon microstrip. xiv, 37, 38

SM Standard Model. v, xiii, xv, xvi, xvii, xviii, 1, 2, 4, 5, 6, 10, 12, 13, 14, 15, 17, 19, 20, 21, 22, 24, 25, 27, 28, 36, 47, 57, 61, 62, 68, 70, 72, 74, 75, 79, 82, 83, 84, 95, 101, 103, 121, 126

SR Signal Region. xviii, 74, 84, 94, 95, 101

SUSY Super Symmetry. v

TGC Thin Gap Chambers. 41

TRT Transition Radiation Tracker. xiv, 37, 38

VBF Vector Boson Fusion. xi, xii, xvi, xvii, xviii, xix, xx, xxi, 2, 13, 25, 26, 57, 59, 63, 68, 70, 71, 72, 74, 75, 79, 82, 84, 86, 87, 88, 90, 94, 95, 98, 95, 98, 101, 103, 105, 106, 108, 109, 114, 119, 121, 123, 127

VBS Vector Boson Scattering. xiii, xv, xxi, 13, 63, 70, 123, 126

vdm van der Meer. 88

ACKNOWLEDGMENTS

I had the privilege to work with many talented people who greatly contributed to the work presented in this thesis. I especially want to thank my supervisors, Georges Azuelos and Jean-François Arguin for giving me the opportunity to work on this exciting project. With his vast knowledge of the theoretical models and various aspects of the ATLAS experiment and his passion for physics, Georges helped me to tackle various challenges I had when producing these results. Without his constant guidance this work would not have been possible. Thanks to the many detailed discussion with my co-supervisor Jean-François, his critical thinking and great insight in various experimental aspects of the ATLAS detector, I was able to push my studies further.

I would like to thank the WZ-analysis team, mainly Samira Hassani, Joani Manjarres, Miaoran Lu and Salah-Eddine Dahbi with whom I was able to do the analysis and publish the paper. Thank you for your hard work on the analysis framework, Miaoran, and to always provide me with all the necessary input samples for my studies.

A special thanks also to various members of the UdeM ATLAS group who helped me with various problems in my analysis, including Tuan, Otilia and Chloé. I also would like to thank the summer student with whom I worked on some aspects of the analysis, Simon and Alex. A special thanks to my colleagues Kazuya and Jérôme, thanks for all the help with various frameworks and with your help in getting started with the analysis. Louis-Guillaume was incredibly helpful with my authorship task and it is thanks to him that I developed a special interest in Machine Learning. He was always there to discuss issues regarding neural networks and various aspects of Machine Learning. I also want to mention various students with whom I had the honour to do classes and enjoy my student life, for example Mirjam, Eric, Victor and Antoine, just to name a few. Finally, I would like to thank Annabelle for keeping me motivated and listen to my various student problems.

On a more personal basis, I would like to thank my parents for providing all the support in my long life as a student. Without them, all this would not have been possible.

The biggest thanks goes to my wonderful wife Cynthia ! Without you, I would not

have moved to Montreal and without your continuous support I would not have endured my long graduate studies.

STATEMENT OF PERSONAL CONTRIBUTIONS

The ATLAS experiment is a large collaboration in which thousands of people make significant contributions. The results in this thesis required the help of many members and groups of the ATLAS collaboration. Analyses rely on the work of many people and are therefore published in the name of the whole collaboration. Here are some of my personal contributions.

In my first year as a member of ATLAS, I worked on the implementation and optimisation of neural networks for the newly added Insertable B-Layer (IBL) detector as well as for the upcoming replacement of the inner detector, the Inner Tracker (ITk). This work was done as part of my authorship work, to become a qualified author of the ATLAS collaboration. For some time, neural networks have been used to assist in tracking (see [1] for a general description and a more recent technical note [2]). In a dense environment, as for example inside high-p_{T} jets, charge clusters left by ionising particles in the ATLAS pixel detector can merge, compromising the tracking efficiency. Neural networks are used to identify clusters produced by multiple particles and to measure the hit positions of all particles within these clusters. This allows to recover optimal performance. Previously, neural networks had been optimised using the three layer setup of the pixel detector before the IBL detector was installed. My task was therefore to study if the performance of the neural networks could be improved by re-optimising the hyperparameters of the network when including the IBL layer in the setup.

As the inner detector will be completely replaced after run-3 by the ITk detector, the neural network had to be adapted to work with the new detector setup. I successfully trained the neural network on simulations with the new ITk detector. Since the ITk detector is still being developed and the design is still prone to change, no publication was foreseen using the trained neural networks. Therefore, this work has not been included in this thesis.

As most ATLAS members, I performed shifts for the experiments. This included shift in the data quality group, where I had to check the overall quality of the data and the performance of the detectors to either signal problems or sign off runs to be used

for analyses. Later, I became contact person for the handling of data set reproduction request of the ATLAS Exotic group. In this role I was in charge of producing derived data sets from data or Monte Carlo samples with specific run conditions and specific reconstructed objects. I worked together with the analysers if there were problems related to derivations in their analysis. The ATLAS collaboration has a credit system to value the work performed for the collaboration. Based on this credit system, conference speakers are selected to present new results on behalf of the collaboration. In this context I was invited to present new electroweak results of the Standard Model group at the Kruger2018 conference in South Africa.

My main data analysis contribution has been on the search for a WZ resonance described in this thesis, which I performed together with the contact editors Georges Azuelos, Samira Hassani and Joany Manjarres, as well as Miaoran Lu, Salah-Eddine Dahbi and Kazuya Mochizuki. I touched on almost all parts of the analysis, from the signal and background simulation, selection optimisation and signal region definition, analysis framework development, systematic uncertainties calculation and the writing of the internal note and the published papers. I presented the results at various group meetings and at the LHCP 2018 conference, see also the proceedings published here [3]. With my expertise in Monte Carlo event generation I also performed many studies for the Exotics group, I studied for example the interference between Heavy Vector Triplet (HVT) and Georgi-Machacek (GM) signal samples (see Chapter 3) and the Standard Model background, as well as t-channel contribution in the HVT benchmark model. I also studied the possibility to simulate large-width samples for the HVT and GM benchmark models.

In the continuing effort to update the WZ resonance analysis using data collected in 2017 and 2018, I started a study to use neural networks and Boosted Decision Trees to define one of the signal regions of the analysis. A large improvement in the sensitivity by using these modern machine learning algorithms is expected (see Chapter 6.1). I also contributed by the preparation of the simulation for the signal samples at Next-to-leading order.

CHAPITRE 1

INTRODUCTION

The Large Hadron Collider (LHC) is the largest current particle physics experiment exploring both the Standard Model (SM) of particle physics and what is lying beyond. The SM provides our current understanding of all fundamental particles and their interactions, except those due to gravity. Two major experiments, CMS and ATLAS, have been designed to measure precisely certain parameters of the SM and to look for signs of new physics at the LHC. One of their main goals is the study of the electroweak symmetry breaking (EWSB) mechanism.

A brief overview of the theory will be presented in Chapter 2. Given a basic set of parameters, the theory is able to predict particle couplings, decay widths and cross sections and has been verified by numerous experiments. A recent success was the discovery of the Higgs boson at the LHC [4, 5], the last missing particle in the SM. The Higgs boson of the SM is linked to the EWSB mechanism, which generates the W and Z masses via the Higgs mechanism. Despite its obvious success, some fundamental flaws in the theory call for a more general theory. The *fine-tuning* of the Higgs boson or *hierarchy* problem, will be discussed in Chapter 2 along with some other experimental observations that the SM fails to explain, such as the dominant mass-energy content of the Universe.

Because of the aforementioned fine-tuning problem, it is generally thought that the SM may not be the complete story and the exact nature of EWSB is still to be determined. One example of a possible SM extension which addresses the fine-tuning problem, the composite Higgs models, will be presented in Chapter 3. These models hypothesise the Higgs as a composite particle of a new strong interaction. Electroweak symmetry breaking would then occur dynamically and the fine-tuning problem is avoided. These models predict the existence of new resonances, for example vector-like fermions, and heavy vector resonances at energies accessible to the LHC. The Minimal Composite Higgs Model (MCHM) model will be presented in some details to illustrate how composite

Higgs models address the hierarchy problem. Since it is impossible to cover all the available theoretical models and parameter space, so-called benchmark models are used instead for searches at colliders. Two benchmark models, one related to the class of composite Higgs models (Model B) like the MCHM and the other to an extended gauge symmetry model (Model A), are based on a Heavy Vector Triplet (HVT) parametrisation of the Lagrangian. A third benchmark model, the Georgi-Machacek (GM) model, assumes an extended Higgs sector predicting charged Higgs bosons.

Two major experiments, CMS and ATLAS, have been designed to measure precisely certain parameters of the SM and to look for signs of new physics at the LHC. One of their main goals is the study of the EWSB mechanism. Chapter 4 will present relevant parts of the ATLAS experiment, one of the two major experiments of the LHC. It will be shown how the different parts of the detector allow to precisely measure and study SM particles.

Searches for diboson resonances are an essential tool to look for extensions of the SM. As aforementioned, vector and scalar resonances are predicted in various models that go beyond the SM, which would be produced by either vector boson or quark/gluon fusion. After summarising the present status of searches for such phenomena in Chapter 5, a new search for resonant WZ production is presented, targetting both the quark/gluon fusion and Vector Boson Fusion (VBF) production modes, extending the previous analysis. Here, data collected in 2015 and 2016 with the ATLAS detector are used to look for scalar or vector resonances predicted by the three benchmark models presented in Chapter 3, the models A, B and the GM model.

In Chapter 6 the ongoing work to prepare the analysis with the full run-2 data set is presented, which nearly quadruples the available data. The updated analysis will not only incorporate the additional data but will also feature several improvements designed to increase the sensitivity. A Multivariate Analysis (MVA) selection using machine learning algorithms for the VBF selection has been shown to greatly improve the selection efficiency and background rejection compared to the cut-based analysis used in the previous analysis. Better signal models and backgrounds are generated to improve the Monte Carlo (MC) predictions and new algorithms are studied to increase the selection

efficiency for large invariant resonance masses.

Finally, a conclusion and outlook are presented in Chapter 7.

CHAPITRE 2

THE STANDARD MODEL

The Standard Model (SM) [6–8] of particle physics is a quantum field theory describing the behaviour of particles under the influence of Quantum Chromodynamics (QCD), and the electroweak interactions, the latter unifying the electromagnetic and weak force. It sets the foundation of the current understanding of fundamental particles and their interactions. It has been developed in the 1960s and 1970s and has been confirmed at an extraordinary level of precision by numerous experiments, e.g. at the Large Electron-Positron Collider (LEP) or the Large Hadron Collider (LHC).

This Chapter presents the most important aspects of this model and its predictions. At the end of the Chapter some limitations of the SM are highlighted which motivate the development of extensions of the SM providing possible solutions. Some examples of such theories are presented in Chapter 3.

2.1 The Standard Model : A Field Theory

Quantum field theory is the language with which the laws of particle physics are described combining relativity and quantum mechanics. Quantum operators in a quantum field theory *live* in the Hilbert space and the Hamiltonian H describes the time evolution of these operators.

Any physical theory is based on several fundamental principles [9, pp.7]. These include for example unitarity (the sum of all probabilities over all events must be equal to one), as well as Lorentz invariance. An additional condition that is imposed on the SM is renormalisability : the theory must be able to predict physical interactions at all energies. The SM has been shown to be renormalisable [10].

2.2 Gauge Symmetries

Symmetries play a crucial role in the SM. In classical physics a symmetry is a transformation that preserves measurable physical properties. This is equivalent to say that a system is invariant under a transformation if it leaves the Lagrangian invariant. There are both global and local symmetries. A global symmetry has parameters that are constant throughout space-time whereas for a local transformation the parameters do depend on the position. One example for a global symmetry are phase transformations of a field which are described by a $U(1)$ group of the form

$$\phi(x) \rightarrow \mathrm{e}^{\mathrm{i}\alpha}\phi(x) \; . \tag{2.1}$$

The complex phase of a field is not measurable and the Lagrangian is invariant under such transformations. The symmetry is a local gauge if the parameter α depends on the position x, $\alpha \rightarrow \alpha(x)$. A massless gauge boson is associated with each of the generators of the local gauge symmetry group. Global symmetries do not have such associated gauge bosons. The gauge symmetry of the SM is given by :

$$SU_c(3) \times SU_L(2) \times U_Y(1) \; . \tag{2.2}$$

$SU_c(3)$ denotes the colour symmetry of QCD, the subscript "c" denotes "colour", and $SU_L(2) \times U_Y(1)$ refers to the gauge symmetry of the electroweak force. The subscript "L" indicates that only left-handed fermions carry this quantum number. The subscript "Y" refers to the weak hypercharge. There is no deeper understanding as to why the gauge group has this particular form and it is taken as an observed fact.

2.3 Particle content of the Standard Model

Existing fundamental particles can be grouped by their quantum numbers such as the spin, colour etc. All non-gravitational experiments seem to be describable by particles with spin zero through one. Particles with half-integer spin are called *fermions* and particles with integer spin are called *bosons*.

2.3.1 Gauge Bosons

The interactions of SM particles are the results of four fundamental forces : the strong, weak, electromagnetic and gravitational forces. Since the SM does not account for the theory of gravity, only three of the four fundamental forces are treated here. The strong, weak and electromagnetic interactions arise due to the exchange of *gauge bosons*. As seen in the previous section, each generator of the gauge group is associated with a massless gauge boson. The spin-one particles associated with the strong force are called *gluons*. The colour symmetry $SU_c(3)$ is a gauge symmetry with 8 generators. Therefore there are eight different gluons carrying the colour charge of the strong interaction. Any particle which couples to the gluons is strongly interacting. As the gluons are themselves carriers of the colour charge, they can self-interact.

There are four spin one bosons associated with the electroweak group as the associated local electroweak symmetry $SU_L(2)\times U_Y(1)$ has four degrees of freedom. Four bosons are associated with the electroweak symmetry, three W^i_μ which are associated with $SU_L(2)$ and one B_μ associated with $U_Y(1)$. How these are related to the $W^\pm$, Z^0 and γ bosons of the SM mediating the weak and electromagnetic force will also be discussed in the context of the Higgs mechanism, see section 2.5. In addition to the above mentioned physical bosons, the SM predicts another spinless boson, which has recently been observed by both the ATLAS and CMS experiments, named the Higgs particle. The masses of quarks and leptons are generated by interactions with the Higgs field. Without this field and its associated boson, all particles in the SM would be massless. An overview of the elementary particles with their properties can be found in Figure 2.1.

2.3.2 Fermions

Fermions are spin-half particles and they come in three generations. Each generation couples identically to the bosons, and is more massive than the previous one. Fermions are furthermore divided into two sectors : leptons and quarks. There are six leptons : the electron e, the muon μ, the tau τ and three associated neutrinos : ν_e, ν_μ and ν_τ. Each lepton is represented in quantum electrodynamics by a 4-component Dirac spinor, for

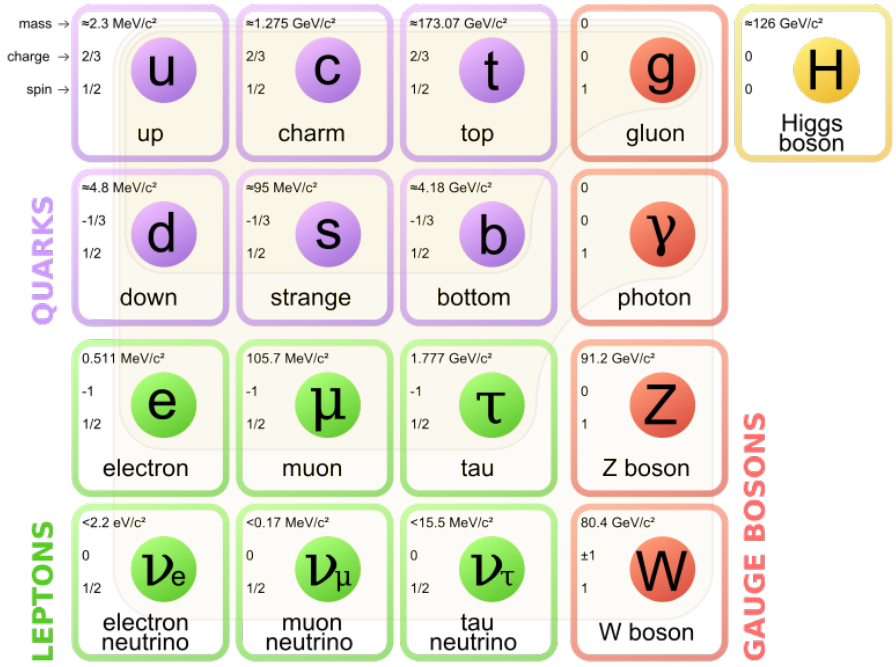

FIGURE 2.1: Table of elementary particles with their masses, charges spins and names. [11]

example $e(x)$ for the electron field. They represent a particle and an antiparticle, which, in the Weyl representation, correspond to two chiral components denoted e_L and e_R for the left- and right-handed component.

The left-handed components are doublets of $SU(2)_L$ whereas the right-handed are singlets. Charged leptons are subject to all fundamental forces except the strong force, but only the left-handed component is subject to the weak force. Neutrinos are very light. They do not carry electrical charge and therefore only interact via the weak force. For every fermion there exists a particle with the same mass but opposite quantum numbers. These particles are referred to as anti-particles.

Quarks on the other hand interact primarily via the strong force by the exchange of gluons but can also interact with any of the other bosons. Quarks come in six flavours, which are denoted the up u, down d, charm c, strange s, top t and bottom b quark. They have fractional charges of either $\frac{2e}{3}$ or $-\frac{e}{3}$, where e denotes the electric charge of the proton : $1.602 \cdot 10^{-19}$ Coulomb. Quarks carry the colour charge which comes in three

flavours : red, green and blue. Bound states are colourless. This can either be satisfied by combining all colour charges or by combining a quark with an anti-quark carrying the opposite colour charge, e.g. red and anti-red. A quark bound to an anti-quark is called a meson. One example is a bound state of an up and anti-down quark $u\bar{d}$, forming a π^+ pion, where u and $\bar{d}$ carry opposite colour charge. Fermions made up of three quarks are called baryons. One example is a proton, which has the quark content uud, two up quarks and one down quark.

2.4 Quantum Chromodynamics

Underlying the physics of proton-proton collisions, occurring for example at the LHC, is the theory of QCD. The proton is a hadron, a composite particle held together by the strong force, composed of quarks and gluons and QCD describes the strong interactions of these particles.

An important feature of QCD is *asymptotic freedom*, which refers to the fact that the QCD coupling strength, α_s decreases with increasing energy. At high enough energies or short enough distances, α_s becomes small so that coloured particles can effectively be treated as free. However, the QCD potential energy between colour quarks increases as they are separated. When enough potential energy becomes available, a quark-anti-quark pair can be produced in order to bind and neutralise the colour charge. As a result, only colour neutral hadrons rather than isolated colour charges can be observed. This property of QCD is known as *confinement*.

The proton is a bound state of strongly interacting quarks and gluons (partons), confined within the proton. When colliding two protons, interactions take place between the partons of the two protons giving rise to hard scattering.

The content of the proton can be summarised by a set of probability distributions of quarks and gluons, named parton distribution function (PDF), which are independent of what particle is used to probe the proton. These PDF determine the probability of finding a parton of a given flavour and momentum inside the proton at given virtuality q^2 [12], as illustrated in figure 2.2. In figure 2.3 the production of a $W^{\pm}Z$ pair in a hard interaction

is illustrated.

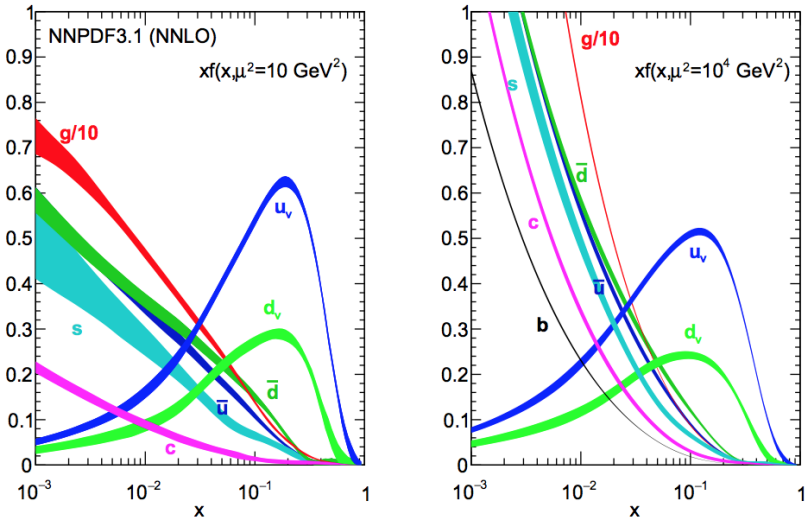

FIGURE 2.2: One popular PDF set called NNPDF3.1 for NNLO calculations, evaluated at virtuality $q^2 = 10\ \text{GeV}^2$ (left) and $q^2 = 10^4\ \text{GeV}^2$ (right). [13]

In addition to the hard scattering process, high energy quarks and gluons can be produced in the interaction. These high energy virtual partons will produce additional quarks and gluons which, in their turn, radiate other quarks and gluons as they travel. This is known as fragmentation. Finally, these quarks and gluons hadronise to neutralise the free colour charge. The end product is a collimated spray of hadrons which is known as a jet.

2.5 The Weak Sector and the Higgs mechanism

The electroweak interaction unifies Quantum Electrodynamics (QED), describing the interaction of charged particles, and the weak force. With the success of QED, in predicting for example the value of the fine structure constant to an astonishing accuracy [14], physicists developed a model for the weak interaction analogous to QED. In 1954 Yang and Mills [15] developed a non-Abelian gauge theory based on the SU(2) symmetry, which was extended in 1961 by Glashow [16] to a $SU(2)\times U(1)$ group, that should describe both the electromagnetic and weak interactions. This gauge group has four associated

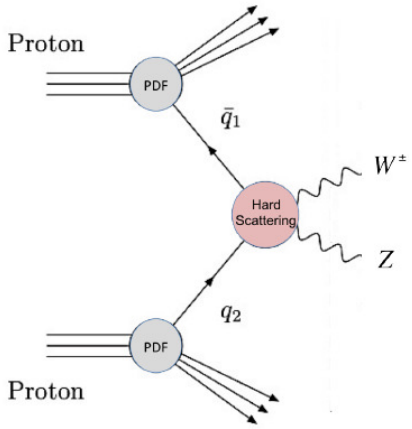

FIGURE 2.3: $W^{\pm}Z$ production at p-p colliders. [12]

massless gauge bosons W^i_μ, $i = 1, 2, 3$, and B_μ for the $SU(2)$ and $U(1)$ group respectively as well as the corresponding gauge coupling constants g and g'. A gauge invariant symmetry model analogous to QED was preferred as QED is renormalisable. However this requires the gauge boson to be massless as a mass term of the form $m^2 A_\mu A^\mu$ destroys the gauge symmetry of the Lagrangian and makes the theory non-renormalisable.

One solution to the experimental fact that the W and Z bosons are in fact not massless is to introduce a mechanism of spontaneous gauge symmetry breaking in a gauge invariant field theory, the commonly named Higgs mechanism. By the Goldstone theorem, the spontaneous breaking of a continuous symmetry implies the existence of massless scalars, the Goldstone Bosons [17]. A new degree of freedom is introduced to the theory, the complex $SU(2)$ doublet Higgs field $\phi \equiv \begin{pmatrix} \phi^+ \\ \phi^0 \end{pmatrix}$. The SM Higgs potential is given by, following the notation of Particle Data Group [18] :

$$V(\phi) = \mu^2 \phi^\dagger \phi + \frac{\lambda^2}{2} (\phi^\dagger \phi)^2 \, . \tag{2.3}$$

For a negative value of μ^2 the potential resembles a Mexican hat, see figure 2.4. It develops non-zero minimum energy or vacuum expectation value (vev) of $vev/\sqrt{2} = \mu/\lambda \approx 246/\sqrt{2}$ GeV. When the Higgs doublet acquires the vev, it induces a spontaneous symmetry breaking.

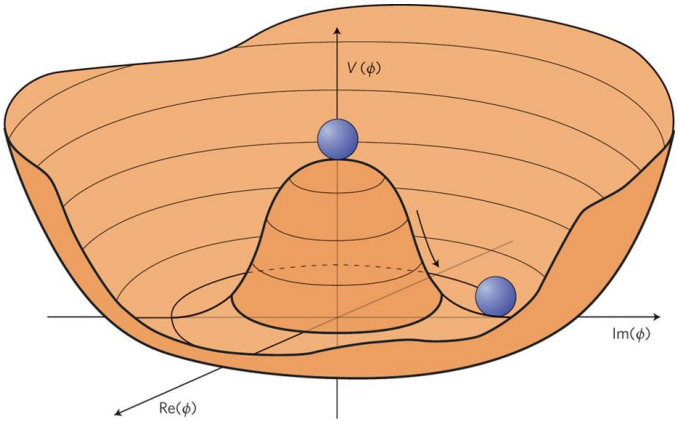

FIGURE 2.4: Illustration of the Higgs potential acquiring a *vev*. [19]

The Higgs mechanism is described as a spontaneous symmetry breaking of the $SU_L(2) \times U(1)$ symmetry to a $U(1)$ subgroup. When the symmetry is broken, three of the four components of the Higgs field are Goldstone bosons which are absorbed (eaten) by the massless gauge bosons. A massless particle, which has only two transverse components of polarisation, acquires a mass when the Higgs boson field is eaten and becomes its longitudinal component of polarisation. The fourth generator remains unbroken since it is the one associated with the conserved $U(1)$ gauge symmetry, and its corresponding gauge field, the physical photon, remains massless. As a result, three of the four gauge bosons (the W^+,W^- and Z boson) become massive while the photon remains massless. The $W^\pm$, Z boson as well as the photon field (γ) are then given by

$$
\begin{aligned}
W^\pm &\equiv (W^1 \mp iW^2)/\sqrt{2} \\
Z &\equiv -B \sin\theta_W + W^3 \cos\theta_W \\
A &\equiv B \cos\theta_W + W^3 \sin\theta_W \ .
\end{aligned}
$$

Here $\theta_W \equiv \tan^{-1}(g'/g)$ is the weak (Weinberg) angle. At tree level the boson masses are given by

$$M_H = \lambda v, \tag{2.4}$$

$$M_W = \frac{1}{2} g v = \frac{e v}{2 \sin \theta_W}, \tag{2.5}$$

$$M_Z = \frac{1}{2} \sqrt{g^2 + g'^2}\, v = \frac{M_W}{\cos \theta_W}, \tag{2.6}$$

$$M_\gamma = 0. \tag{2.7}$$

Here $e = g \sin \theta_W$ is the positron electric charge.

In this model not only the gauge bosons become massive. Fermions get their mass as they couple to the Higgs field via Yukawa interactions. The mass terms contain the left- and right-handed components of the Dirac spinor, and since the neutrinos have no right-handed component in the SM, they remain massless. After symmetry breaking, one degree of freedom of the Higgs field remains, which forms the massive Higgs scalar H.

This mechanism gives an accurate description of the unification of the weak and electromagnetic interaction and its predictions are validated by experimental results. The predicted neutral current was found at CERN in 1973. The W and Z were found in 1983 and up to 2001, at LEP and Stanford Linear Collider (SLC), precision electroweak (EW) measurements were performed allowing to constrain the mass of a hypothetical Higgs boson [20]. Finally, in the summer of 2012 both ATLAS and CMS announced the discovery of the Higgs boson, the last missing particle in the SM.

2.6 Multi Boson Interactions

In the SM the electroweak gauge bosons, the $W^\pm$ and Z bosons, carry the weak charge. Therefore self-interactions are possible. The SM contains interaction vertices with three bosons (triple gauge coupling) or four bosons (quartic gauge coupling). The possible self-interaction is linked to the non-Abelian nature of the EW sector, so by testing multi-boson interactions, the non-Abelian character of the gauge group can be directly tested [21]. This has already been done in the context of QCD, but it is much more interesting in the case of the EW sector because of the link between EW gauge

bosons and the electroweak symmetry breaking (EWSB) discussed above. The $W^{\pm}$, Z boson have the strongest coupling to the Higgs other than the top quark and provide a much cleaner signature.

The historical connection between multiple vector boson production and EWSB is the role of the Higgs in unitarising the amplitude of $WW \rightarrow WW$ Vector Boson Scattering (VBS) (see figure 2.5). Without the inclusion of a Higgs field, the WW scattering process violates unitarity, making the theory incomplete [22]. One of the main goals of the LHC is to validate the SM and to show the effects of the Higgs on VBS. Additionally, there could still be small deviations in the EWSB that would manifest themselves in Vector Boson Fusion (VBF) or VBS either as obvious deviations in the differential cross section or by new resonances appearing in VBS processes. In the case of $WZ \rightarrow WZ$ scattering, the SM Feynman diagrams contributing to the amplitude are shown in figure 2.6.

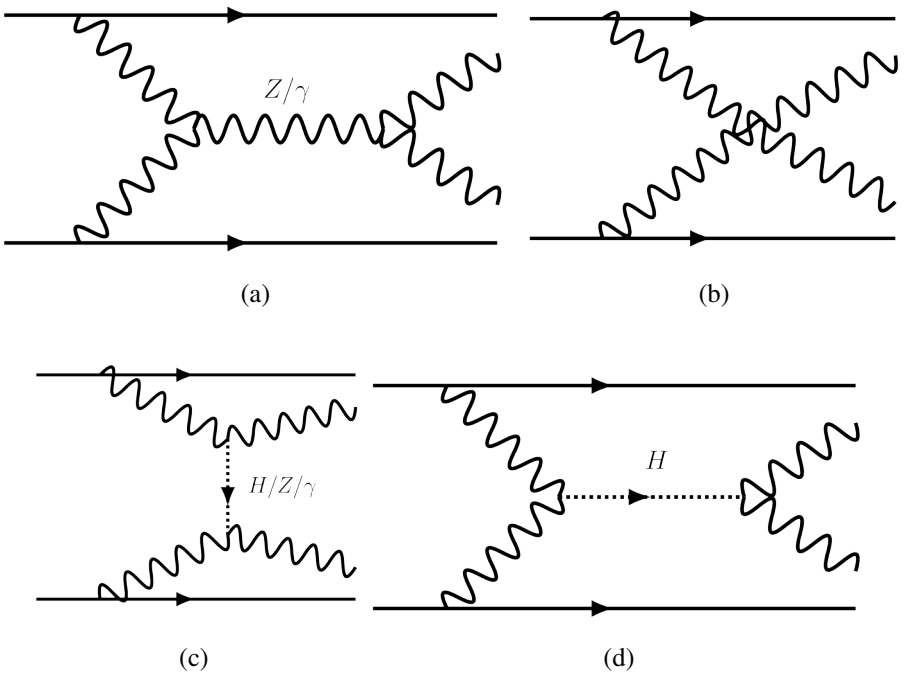

FIGURE 2.5: VBS in the SM with the exchange of gauge bosons (Z, γ) in the diagrams (a), (b) and (c), and the Higgs in diagrams (c) and (d) needed to preserve perturbative unitarity in the SM.

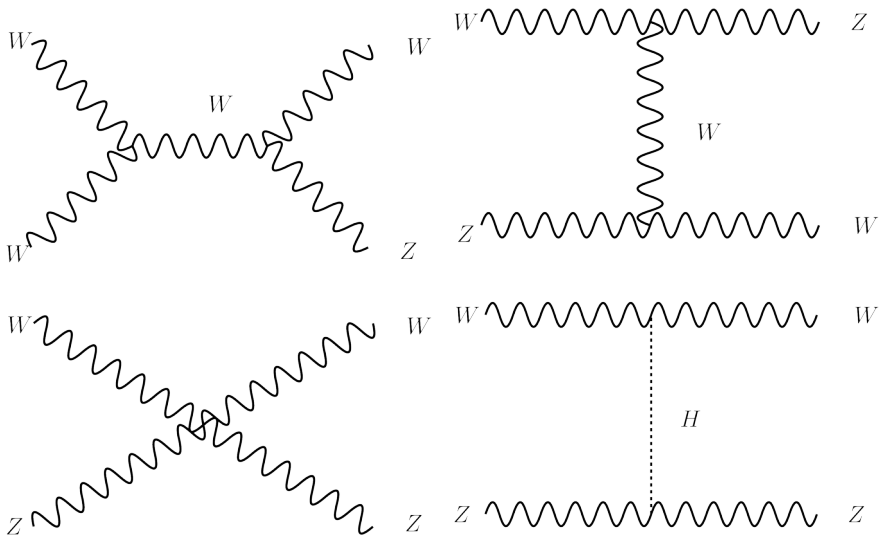

FIGURE 2.6: Feynman diagrams that contribute to the ($WZ \rightarrow WZ$) tree level amplitude in the SM.

2.7 Limitations of the Standard Model

Even if the current SM can successfully describe most of all current particle physics experiments, there are still observations where this model fails to provide a good explanation, such as neutrino oscillations. The SM predicts massless and stable neutrinos. Several experiments, for example those observing solar neutrinos, have shown however that neutrinos oscillate between flavours [23]. An oscillation would only be possible if the neutrinos were in fact not massless [9].

The SM has the obvious shortcoming of not incorporating gravity. Gravity could in principle be incorporated by quantising the Einstein-Hilbert action. This however introduces non-renormalisable interaction operators involving gravitons, which will lead to divergences in scattering amplitudes at the Planck scale $M_P \approx 10^{19}$ GeV [24]. Therefore some new particles or interactions beyond the SM have to be present to describe physics at this scale. However the scale at which new physics become apparent could be as high as the Planck scale, which is unfortunately completely beyond the energy reach of current experiments.

Another striking shortcoming of the SM is its inability to describe 95% of the energy content of the Universe. Current observations strongly suggest that dark matter ($\approx$ 23%) and dark energy ($\approx$ 72%) completely dominate the Universe [25, 26]. There is no massive weakly coupled particle in the SM that could act as dark matter. In principle, dark energy could be explained in the framework of the SM by non-zero vacuum energy of scalar and fermionic fields [9, pp.437]. But when doing the calculations, the predictions differ from observations by some 122 orders of magnitude ! This is the biggest discrepancy known in physics between predictions and observations. The SM also does not provide an explanation for its gauge symmetry structure, particle content (for example why there are three generations of fermions with a large hierarchy in their masses) and it has 19 free parameters that need to be measured by experiment. A well-known shortcoming of the SM is its inability to describe physics at very high energies near the Planck Scale. Here, the grand unification theory is supposed to combine all forces of the SM, which would just be different aspects of a unified interaction. [27]

It could be assumed that the SM is a low energy limit of a more fundamental higher energy theory. It is desired that the physical content of this effective theory follow naturally from the properties of the higher energy theory without the need for fine tuning the parameters so that they fit the description at low energies. At high energies, heavy particles from a not yet fully known high-energy theory would contribute to various processes. Let's assume that the SM is valid up to some scale Λ_{SM}, say Λ_{SM} = 10 TeV. To be able to compute loop diagrams, we would cut the integration around Λ_{SM}. The hierarchy problem arises because the contributions of diagrams with this cut-off to the Higgs mass are quadratically divergent and have to be cancelled by "fine-tuned" counter terms (see also figure 2.7 for a few examples of SM contributions to the Higgs mass). As recently discovered at the LHC, the Higgs is relatively light : its mass is measured to be around 125 GeV [28]. To explain this experimental result, with Λ_{SM} = 10 TeV, fine tuning of about one part in 100 among the tree-level parameters is required. If we want the SM to be valid up to energies of Λ_{SM} = 100 TeV, the fine-tuning required is much greater, about one part in 10000, thus making the theory "unnatural" [29]. If on the other hand, we expect new physics to take over at around Λ_{SM} = 1 TeV, the need for fine-tuning

can disappear.

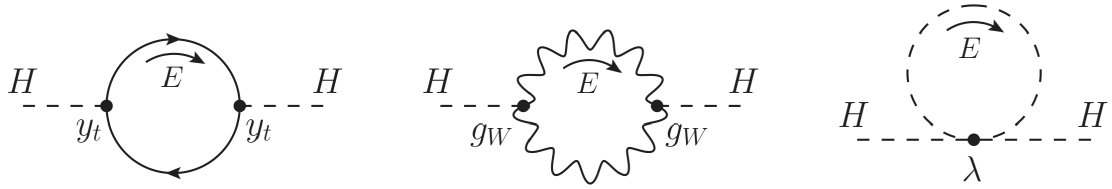

FIGURE 2.7: Some representative top, gauge and Higgs boson loop diagrams that contribute to the Higgs mass. [24]

There exist several solutions to get around this fine-tuning problem. One solution is to introduce theories with additional symmetries. With these new symmetries, the high energy particle contributions cancel naturally. One of these theories with additional symmetries is supersymmetry [18] [30], which relates bosons to fermions. Supersymmetry also provide solutions to other problems mentioned above, it has for example a dark matter candidate and the coupling constant of the forces meet at a single point at high energy, therefore facilitating a grand unification. This theory, although very elegant, will not be discussed in more detail since it is not subject of this thesis. There is however another possibility to avoid fine-tuning problem : a class of theory models called composite Higgs models. In these models, quantum corrections are cancelled at the compositeness scale of this theory. A more detailed description of the composite Higgs models is given in the next Chapter.

CHAPITRE 3

MODELS BEYOND THE STANDARD MODEL

As described in section 2.7, there are many limitations to the Standard Model (SM) and therefore the search for a more complete theoretical model continues. In this section, some theories and concrete models which go beyond the SM are introduced. First, a class of theory models, referred to as composite Higgs models, is presented, which try to give sense to the observed Higgs mass and therefore avoid the fine-tuning problem of the SM. It is difficult or rather impossible to cover all possible models that can be searched at the Large Hadron Collider (LHC). The only viable option is to search for benchmark models, which can then in turn be interpreted in more general models. In sections 3.3 and 3.4 of this Chapter three benchmark models are introduced which are related to the class of composite Higgs models or to extended symmetry models. Also models with an extended Higgs sector, predicting charged scalar, can be a potential signal. These benchmark models aim at providing concrete predictions for searches done at the LHC, which can in turn put limits on fundamental model parameters.

3.1 Composite Higgs

As seen in section 2.5, the electroweak symmetry breaking is explained by the introduction of new degrees of freedom : the Higgs field. This does not, however, explain why the Higgs Boson is relatively light. This is linked to the fine-tuning problem, mentioned in the previous Chapter. The composite Higgs theory was developed to give a physical explanation of the Higgs mass. In this theory, the Higgs boson would be a bound state of a new strongly-interacting dynamics not much above the weak scale [22]. The composite Higgs model builds on the idea of simple Technicolour models, presented in the following section.

3.1.1 Technicolour Models

Besides the Higgs mechanism, there is another historically important model which was proposed to explain the electroweak gauge symmetry breaking, the Technicolour model, inspired by Quantum Chromodynamics (QCD). QCD is assumed to be asymptotically free at very high energies and to become strong and confining as the energy decreases to the electroweak scale of 246 GeV. When neglecting the quark masses, the QCD Lagrangian respects a global symmetry called chiral symmetry, $SU(2)_L \times SU(2)_R$. This symmetry is spontaneously broken into its vectorial subgroup $SU(2)_V$ by QCD condensates. Assuming massless u and d quarks, the spontaneous symmetry breaking would result in four associated Goldstone bosons. Three of these can be identified as pions π^α. In the limit of vanishing quark masses and before turning on the weak interactions, the pions are exact Goldstone bosons of the global chiral symmetry and are therefore massless. The pions are then eaten to give mass to the W and Z bosons. The surviving unbroken group is the electromagnetic $U(1)_{em}$ group. The prediction of the W mass through this process ($m_W \approx 29$ MeV [22]) are well below experimental values, but illustrates how $SU(2)_L \times U(1)_Y$ can be broken without using Higgs scalars. The electroweak symmetry breaking dynamics could in principle be a scaled-up version of the QCD process to give the correct W and Z masses. In this context, a Technicolour gauge group with global $SU(2)_L \times SU(2)_R$ symmetry would be broken down to $SU(2)_V$ similar to QCD at low energy due to confinement. This kind of symmetry breaking mechanism is referred to as dynamical symmetry breaking. In the Technicolor theories there could possibly be more than three colours for techniquarks, and more than three generations of fermions. The Technipion fields would be an admixture of the longitudinal component of W and Z and a mass-eigenstate of Technipion π_{TC} [31] :

$$|V_L\rangle = \sin\alpha|\pi_{QCD}\rangle + \cos\alpha|\pi_{TC}\rangle \ . \tag{3.1}$$

The physical pions are formed by the orthogonal combination. The Technicolour sector would also lead to vectorial resonances, for example the state with the lowest mass, the 'technirho'. As the new interaction is asymptotically free at high energies, an

electroweak scale is introduced in analogy to the QCD scale. The Technicolour theories avoid the fine-tuning problem, mentioned in section 2.7, as the Higgs is absent in this theory.

In Technicolour theories, assuming that the colour group and Technicolour are embedded in a larger Extended Technicolour (ETC) group which is broken spontaneously, the exchange of broken ETC gauge bosons connects quarks with techniquarks and thus generates their masses. These same exchanges would however also give rise to flavour changing neutral current processes, on which stringent limits have been set [32]. One mechanism which avoids this problem is referred to as walking Technicolour [33, 34]. In these models, the gauge coupling is a slowly running (thus "walking") constant, producing a cascade of symmetry breaking at several scales explaining the hierarchy observed in the quark masses. Experimental data still leaves room for this model.

3.1.2 The Higgs as a Composite Boson

The composite Higgs models build on the strong symmetry breaking mechanism. The Higgs boson would no longer be an elementary field but a bound state of the strongly interacting sector. A good introduction to the subject can be found in [24], or [22, 35, 36] for a more detailed description. As an illustration on how this solves the fine-tuning problem let's assume the Higgs, rather than being a point-like particle as in the SM, is instead an extended object with finite geometric size l_H. It is assumed that it is the bound state of a new strong force with a confinement scale $m_* = 1/l_H$ of TeV order. For a complete theory, the physical Higgs mass would be predicted in terms of its true input parameters "p_{true}" by the following formula [24] :

$$m_H^2 = \int_0^\infty dE \frac{dm_H^2}{dE}(E; p_{true}) \tag{3.2}$$

The integral over energy in this formula stands for the contributions to m_H^2 from all the virtual quanta in loops and it extends up to infinity, or up to a very high cutoff of the complete theory itself. In the SM the virtual contributions are divergent : going to very high energies results in the fine-tuning problem (see section 2.7). In this new theory

however, the $\frac{dm_H^2}{dE}$ integrand in the Higgs mass formula 3.2, which stands for the virtual quanta with a given energy, behaves as shown in figure 3.1. Low energy quanta have a large wavelength to resolve the Higgs size l_H. Therefore the Higgs behaves like an elementary particle and the integrand grows linearly with E like in the SM. However, this growth gets cancelled by the finite size effects that start becoming visible when E approaches and eventually overcomes m_*. The composite Higgs is transparent to high-energy quanta and the integrand decreases. The linear SM behaviour is thus replaced by a peak at $E \approx m_*$ followed by a steep fall. The Higgs mass is now insensitive to much higher energies. This would solve the fine-tuning problem as the mass of this composite state would not be sensitive to virtual effects above the compositeness scale.

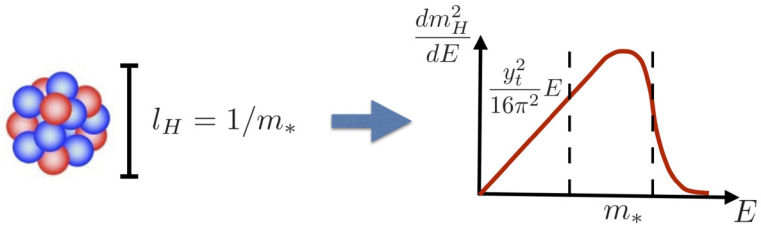

FIGURE 3.1: Pictorial representation of the Composite Higgs solution to the Naturalness problem. [24]

Implementing this idea in practice requires three basic elements, a "Composite Sector" (CS), an "Elementary Sector" (ES) and a set of interactions "$\mathcal{L}_{int}$" connecting the two. The Composite Sector contains the new particles and interactions that form the Higgs as a bound state and it should be viewed as analogous to the QCD theory of quarks and gluons. The CS gives physical origin to the Higgs compositeness scale m_*. The Elementary Sector contains all the particles which we know by phenomenology, cannot be composite at the TeV scale, with the possible exception of the right-handed component of the top quark. The most relevant operators in the ES Lagrangian are thus just the ordinary $d = 4$ SM gauge and fermion kinetic terms and gauge interactions. Since there is no SM Higgs in the ES the theory is natural. The lack of a Higgs forbids Yukawa couplings and a different mechanism will have to be in place to generate fermion masses and mixing.

There is however one problem, if the Higgs is a generic bound state of the CS

dynamics, one generically expects its mass to be of the order of the CS confinement scale m_*, namely $m_H \approx m_*$. Since the mass of the Higgs is around $m_H \approx 100$ GeV and no new particles have been observed at the same mass scale, m_* must be of the TeV or multi-TeV order and some mechanism must be in place to explain why $m_H \ll m_*$. One solution would be that the composite Higgs boson would be a pseudo Goldstone boson of an enlarged symmetry of the strong dynamics, which would explain its light mass [22]. The new strong sector naturally adds composite states, which can either be fermions (vector-like quarks), vector bosons (W', Z') or scalars (Higgs). There exists a great variety of models that differ in the mechanism that generates the Yukawa coupling, e.g. little Higgs model, holographic composite Higgs, minimal composite Higgs. In order to avoid details that go beyond the scope of this work, the following section will mainly concentrate on the Minimal Composite Higgs Model (MCHM) [37] as an illustration of how such a theory works and what the observable features are.

3.1.2.1 The Minimal Composite Higgs Model

In the MCHM the Higgs is a composite pseudo-Goldstone boson arising from the strongly interacting sector. In this case, the Higgs mass is a direct result of the symmetry breaking and is protected from loop correction, which solves the hierarchy problem. A global symmetry $SO(5)$ is spontaneously broken to $SO(4)$ at a scale $f_\pi \sim (\sqrt{N}/4\pi)m_\rho$ [37]. Here N refers to the number of "colours" of the new strong sector and m_ρ defines the scale of new resonances. The SM gauge bosons and fermions are external to the new strong interaction. However, in the MCHM the top quark constitutes an exception and will be mostly composite. In this model, the electroweak symmetry is dynamically broken. The number of Goldstone Bosons will be four since $SO(5)$ has ten generators and $SO(4)$ has 6 generators. This is exactly what is needed to build a complex Higgs doublet. The Higgs boson field can then be identified as Goldstone bosons forming a real bidoublet of $SU(2)_L \times SU(2)_R$.

As long as the global SO(5) symmetry is unbroken the Higgs field is an exact Goldstone Boson and therefore massless. When the interactions of the new strong sector and the SM field violate the symmetry the Higgs becomes a composite pseudo Goldstone

Boson and acquires a mass. However, these interactions do not trigger EWSB. It will be the fermion interactions, especially from the top that trigger the $SU(2)_L \times U(1)_Y$ symmetry breaking. Fermions Ψ in this model contain two doublets, one transforming under $SU(2)_L$, (q_L), and the other transforming under $\mathrm{SU}(2)_R$, (u_R, d_R). Fermions are assumed to couple linearly to the new strong sector operators $\mathcal{O}$:$\mathcal{L} = \lambda\bar{\Psi}\mathcal{O}$.

The electroweak symmetry breaking (EWSB) scale can be related in this theory to the strong scale f_π by :

$$\upsilon \equiv f_\pi \sin\frac{\langle h\rangle}{f_\pi} = 246 \text{ GeV}\,, \tag{3.3}$$

where h is the norm of the Higgs field parametrised along the broken generators $T^a, a = 1, 2, 3, 4$, so $h = \sqrt{(h^a)^2}$. When the Higgs acquires a vacuum expectation value ($\upsilon e \upsilon$), the fermions get a mass

$$m_{u,d} = y_{u,d}\upsilon\,, \tag{3.4}$$

where $y_{u,d} \sim \lambda_{u,d}\lambda_q\sqrt{N}/4\pi$. Light fermions couple weakly to the new strong sector. In this theory, the smallness and hierarchical structure of light fermions arise naturally. The top quark is mostly composite.

The Higgs potential in this model can be approximated by :

$$V(h) \cong \alpha\cos\frac{h}{f_\pi} - \beta\sin^2\frac{h}{f_\pi} \tag{3.5}$$

This potential has a minimum at $\cos h/f_\pi = -\alpha/(2\beta)$, and a minimum value ϵ of :

$$\epsilon = \sqrt{1 - \left(\frac{\alpha}{2\beta}\right)^2}\,. \tag{3.6}$$

In this model, the EWSB occurs dynamically for suitable parameters α and β. The physical Higgs mass can then be calculated by :

$$m^2_{\text{Higgs}} \backsimeq \frac{2\beta\epsilon^2}{f_\pi^2}\,. \tag{3.7}$$

We see that the Higgs mass is fixed by the parameters of the models. Loop corrections

to the Higgs mass do not diverge as is the case in the SM [37], therefore the fine-tuning problem is avoided.

3.1.2.2 Comparison with other Composite Higgs Models

There is a wide variety of theoretical models in the composite Higgs class. The global symmetry and the exact nature of the EWSB mechanism differ in these alternative models. However, all these models share the idea of a new strong sector with similar phenomenological features like additional vector resonances etc. Some popular examples are the "Little Higgs" or "Littlest Higgs" models [38][39]. These are similar to the MCHM model discussed in the previous section in that the Higgs is once again a pseudo-Goldstone boson of an extended symmetry ($SU(5)$). In these models, additional particles are predicted, including vector states W', heavy photons A_H and doubly charged Higgs boson ϕ^{++}. Another type of models are Holographic composite Higgs models [40], which relate the strong interaction to a weakly coupled interaction in extra dimensional models. For a more detailed comparison of the various models also refer to [41]. Here models are classified by their Higgs potential and the mechanism that generates the fermion masses.

3.2 Simplified Lagrangian

Since there is no single explicit complete model of Beyond Standard Model (BSM) physics which allows precise predictions of experimental observables, it is useful to provide motivated generic frameworks based on broad assumptions on the BSM physics [42]. Examples of such frameworks are the composite Higgs framework mentioned earlier or Supersymmetry. Within each framework, robust qualitative predictions can be made but making quantitative comparison with data requires some explicit implementations of the general idea. Since in general many models can be constructed within each framework and since there is no indication of which model is the right one, all would need to be compared with data. This is impractical, and many models depend on so many free parameters that a full parameter scan would be impossible. One example is the Minimal Supersymmetric Standard Model (MSSM) [43], where a full parameter scan is not feasible

and only restricted versions can be used to compare to data.

It is however easier to try to search for narrow new particles. Here the "Simplified Model" strategy can be adopted as has been for example used in Supersymmetry searches. The idea is that resonant searches are less sensitive to all the details and free parameters of the full model, but they are sensitive only those parameters that control the mass of the resonance and the interactions involved in its production and decay. It is therefore useful to employ phenomenological Lagrangian where only relevant couplings and mass parameters are kept. Aside from symmetry constraints, a simplified model Lagrangian does not need to fulfil the same theoretical requirements as the complete model Lagrangian. Its goal is to provide a parametrisation of a set of explicit models where only those terms are kept which are necessary to describe the resonances. Experimental results with limits on this phenomenological Lagrangian can then be translated to any specific model where the phenomenological parameters can be computed explicitly.

The simplified Lagrangian therefore serves as a bridge between fundamental theories and experimental data. Experimental limits on the phenomenological parameters $\boldsymbol{c}$ can be translated into free parameters $\boldsymbol{b}$ of any explicit model by computing the parameter relations $\boldsymbol{c}(\boldsymbol{b})$.

Even though the simplified models make the experimental search much easier, some care is required when using these models. For example, the simplified models are constructed to describe only the on-shell resonance production. Therefore searches should focus around the peak, as many new physics effects can enter in the tail regions of the signal mass distribution, which are not properly described by the simplified models.

In the following section, an example of such a Simplified Lagrangian is presented describing electroweak-charged spin one resonances. These are included for example in weakly coupled Z' or W' models, or strongly coupled Composite Higgs or Technicolour models.

3.3 Heavy Vector Triplets

In this simplified model, in addition to the SM content, a real vector V_μ^a, $a = 1, 2, 3$, in the adjoint representation of $\mathrm{SU}(2)_L$ is added to the SM. This vector forms one charged and one neutral heavy spin-one particle with the charge Eigenstate defined by :

$$V_\mu^\pm = \frac{V_\mu^1 \mp i V_\mu^2}{\sqrt{2}},\ V_\mu^0 = V_\mu^3 \tag{3.8}$$

Similar to [42], the phenomenological Lagrangian can be written as :

$$\begin{aligned}\mathcal{L}_V = &-\frac{1}{4}(D_\mu V_\nu^a - D_\nu V_\mu^a)(D^\mu V^{\nu a} - D^\nu V^{\mu a}) + \frac{m_V^2}{2} V_\mu^a V^{\mu a} \\ &+ i g_V c_H V_\mu^a \left(H^\dagger \frac{\sigma^a}{2} D^\mu H - D^\mu H^\dagger \frac{\sigma^a}{2} H \right) + \frac{g^2}{g_V} c_F V_\mu^a J_F^{\mu\ a} \\ &+ \frac{g_V}{2} c_{VVV} \epsilon_{abc} V_\mu^a V_\nu^b (D^\mu V^{\nu c} - D^\nu V^{\mu c}) + g_V^2 c_{VVHH} V_\mu^a V^{\mu\ a} H^\dagger H \\ &- \frac{g}{2} c_{VVW} W^{\mu\nu\ a} V_\mu^b V_\nu^c \ .\end{aligned} \tag{3.9}$$

Here, g denotes the $\mathrm{SU}(2)_L$ gauge coupling and $J_F^{\mu\ a}$ is the SM left-handed fermionic currents :

$$J_F^{\mu\ a} = \sum_f \bar{f}_L \gamma^\mu \frac{\sigma^a}{2} f_L \ . \tag{3.10}$$

The parameter c_H controls the V interaction with the SM vectors and with the Higgs and is therefore responsible for Vector Boson Fusion (VBF) production and the decay to vector bosons. The parameter c_F describes the direct couplings to fermions, responsible for the Drell-Yan production and its fermionic decays. Here it is assumed that the coupling is universal to all fermions. It can be generalised to a situation with different coupling to leptons, light quarks and third generation quarks :

$$c_F V \cdot J_F \rightarrow c_l V \cdot J_l + c_q V \cdot J_q + c_3 V \cdot J_3 \ . \tag{3.11}$$

Finally, the parameters c_{VVV}, c_{VVHH}, and c_{VVW} do not contain vertices of a single V

with light SM fields and are therefore not relevant for LHC searches like the one present in this thesis. The phenomenology can then be entirely described by the four parameters c_H, c_l, c_q and c_3 and the mass term m_V.

Looking back to equation 3.9, we see that it includes two couplings constants, g_V and g. The coupling g_V represents the typical strength of V interactions, while the dimensionless coefficients (c_F, c_H) parametrise the departure from the typical size. The fermion couplings include an extra factor of g^2/g_V. The factors c_F, c_H are usually taken to be of order one whereas g_V can vary over one order of magnitude depending on the scenario. The parameter g_V is useful at the theoretical level but is redundant and could be absorbed in the c parameters.

The model is an example of a simplified Lagrangian approach. It aims to describe new vectors with masses at or above the TeV scale. The charged and neutral states are expected to be practically degenerate and have therefore comparable production rates at the LHC.

3.3.1 Decay width

Relevant decays are to di-leptons, di-quarks and di-bosons. We have seen that the coupling to fermions is controlled by the combination of parameters $g^2 c_F/g_V$. The partial width to fermions can be calculated and it depends on the same combination of parameters [42]

$$\Gamma_{V_\pm \to f\bar{f}'} \simeq N_c[f] \left(\frac{g^2 c_F}{g_V}\right)^2 \frac{M_V}{48\pi} \tag{3.12}$$

Similarly, the partial width of the $V_\pm$ can also be calculated for the decays to the Vector Bosons W and Z which is given by

$$\Gamma_{V_\pm \to W_L^\pm Z_L} \simeq \frac{g_V^2 c_H^2 M_V}{192\pi} \tag{3.13}$$

3.3.2 Production rate

There are two main production mechanisms, either by quark-fusion, also referred to as Drell-Yan, or by VBF. The cross-section for both processes is found to be proportional to the partial width $\Gamma_{V\to ij}$

$$\sigma(pp \to V + X) \propto \sum_{i,j\in p} \frac{\Gamma_{V\to ij}}{M_V}\,, \tag{3.14}$$

where $i, j = \{q, \bar{q}, W, Z\}$ denotes the colliding partons in the two protons.

3.3.3 Explicit Models

In this section, two examples of explicit models as suggested in ref [42] are presented. The first one, called model A, describes the vector triplet emerging from an extended gauge symmetry, and a second model B as an example of a simplified minimal composite Higgs model (see section 3.1.2.1).

3.3.3.1 Model A : extended gauge symmetry

In this model, the gauge theory is extended to $SU(2)_1 \times SU(2)_2 \times U(1)_Y$. The SM fermions are charged under $\mathrm{SU}(2)_1$ and $\mathrm{U}(1)_Y$. An additional scalar field Φ is added transforming as a real bidoublet $(\mathbf{2},\mathbf{2})_0$. When Φ acquires a vacuum expectation value f, the $\mathrm{SU}(2)_1{\times}\mathrm{SU}(2)_2$ gauge symmetry is broken into the SM $\mathrm{SU}(2)_L$ gauge group. The fields can be redefined to yield the SM W boson field and the heavy vector V triplet. In this model, the couplings are of the order

$$c_H \sim -g^2/g_V^2 \text{ and } c_F \sim 1\,. \tag{3.15}$$

With this choice of parameters the partial width of the $V_\pm$ to fermions and gauge bosons (eq. 3.12 and eq. 3.13) become comparable ($g^2 c_F/g_V \sim g_v c_H$).

3.3.3.2 Model B : minimal composite Higgs model

Model B is designed to represent models where the Higgs emerges as a pseudo Nambu-Goldstone boson from an underlying strong dynamic, see for example the Minimal Composite Higgs model detailed in section 3.1.2.1. It predicts the existence of a heavy vector resonance with electroweak quantum numbers with strong coupling to gauge bosons, as for example the Minimal Composite Higgs Model described in section 3.1.2.1. The lightest of the new vector resonances can be described by the Simplified Lagrangian Model. In model B both the couplings to bosons and fermions are comparable and of the order one

$$c_H \sim c_F \sim 1 \, . \tag{3.16}$$

Here, the partial width to gauge bosons will dominate over the partial width to fermions ($g^2 c_F / g_V < g_v c_H$).

3.4 Georgi-Machacek Model

The Georgi-Machacek (GM) Model [44] is one example of a model going beyond the SM with an extended Higgs sector and can be reproduced by composite Higgs model [44]. It therefore contains additional scalars arranged in higher multiplets beyond the single SM isospin doublet. The GM model is the preservation of custodial symmetry at tree level by imposing a global $SU(2)_L \times SU(2)_R$ symmetry on the scalar potential. In this way, it avoids stringent constraints from the ρ parameter. The ρ-parameter is a measure of the relative strengths of neutral and charged-current interaction in four-fermion processes at zero momentum transfer. In the SM it is related at tree level to the W and Z boson masses by the relation :

$$\rho = \frac{M_W^2}{c_W^2 M_Z^2} = 1 \, , \tag{3.17}$$

where $c_W = \cos\theta_W$ [45]. In the standard model $\rho = 1$ is a consequence of an "accidental" SU(2) symmetry of the vector boson mass matrix. The GM model contains

a real triplet $(\xi^+, \xi^0, -\xi^{+*})^T$ with $Y = 0$, a complex triplet $(\chi^{++}, \chi^+, -\chi^0)^T$ with $Y = 2$ in addition to the usual SM Higgs doublet $(\phi^+, \phi^0)^T$. The doublet generates the fermion masses as in the SM.

This symmetry becomes apparent when writing the bidoublet and the triplets in the following form [46] :

$$\phi = \begin{bmatrix} \phi^{0*} & \phi^+ \\ \phi^- & \phi^0 \end{bmatrix}, \; X = \begin{bmatrix} \chi^{0*} & \xi^+ & \chi^{++} \\ \chi^- & \xi^0 & \chi^+ \\ \chi^{--} & \xi^- & \chi^0 \end{bmatrix} \tag{3.18}$$

The *vevs* are given by $\langle\phi\rangle = \frac{v_\phi}{\sqrt{2}} I_{2\times2}$ and $\langle X\rangle = \frac{v_\chi}{\sqrt{2}} I_{3\times3}$ with the W and Z boson mass constraint

$$v_\phi^2 + 8v_\chi^2 \equiv v^2 = \frac{1}{\sqrt{2}G_F} \approx (246 \text{ GeV})^2 \tag{3.19}$$

The physical fields after symmetry breaking can be organised into a fiveplet, a triplet and two singlets. The fiveplet and triplet states are given by

$$\begin{aligned} H_5^{\pm\pm} = \chi^{\pm\pm}, \; H_5^{\pm} = \frac{\chi^{\pm} - \xi^{\pm}}{\sqrt{2}}, \; H_5^0 = \sqrt{\frac{2}{3}}\xi^{0,r} - \sqrt{\frac{1}{3}}\chi^{0,r}, \\ H_3^{\pm} = -s_H\phi^{\pm} + c_H\frac{\chi^{\pm} + \xi^{\pm}}{\sqrt{2}}, \; H_3^0 = -s_H\phi^0 + c_H\chi^{0,i} \end{aligned} \tag{3.20}$$

with the *vevs* given by

$$c_H \equiv \cos\theta_H = \frac{v_\phi}{v}, \; s_H \equiv \sin\theta_H = \frac{2\sqrt{2}v_\chi}{v}, \tag{3.21}$$

and the neutral fields are decomposed into real and imaginary parts according to

$$\phi^0 \to \frac{v_\phi}{\sqrt{2}} + \frac{\phi^{0,r} + i\phi^{0,i}}{\sqrt{2}}, \; \chi^0 \to v_\chi + \frac{\chi^{0,r} + i\chi^{0,i}}{\sqrt{2}}, \; \xi^0 \to v_\chi + \xi^{0,r}. \tag{3.22}$$

s_H is the fraction of the W and Z mass that is generated by the triplet χ. The masses (m_3, m_5) within each custodial multiplet are degenerate at tree level.

3.4.1 Theoretical and experimental constraints

Theoretical constraints come, for example, from perturbative unitarity of the scalar couplings [47]. Additional constraints also come from b-physics and electroweak precision data as described in [48].

3.4.2 The H5 Benchmark Plane

The H5plane [49] is designed to facilitate LHC searches for $H_5^\pm$ in vector boson fusion with decays to $W^\pm Z$. This benchmark ensures that the mass of the triplet m_3 is always bigger than the fiveplet mass m_5 so that the Higgs-to-Higgs decays $H_5 \to H_3 H_3$ and $H_5 \to H_3 V$ are kinematically forbidden, assuring a BR($H_5 \to VV$) = 100%. In addition, the benchmark region satisfies constraints from B physics as well as constraints by LHC measurements of the coupling of the 125 GeV Higgs boson.

In figure 3.2 the allowed region in the $m_5 - s_H$ plane for the full GM model (red points) and the allowed region for the H5plane benchmark scenario which covers nearly the whole theoretical allowed region. This makes the H5plane scenario a good benchmark for the interpretation of searches for $H_5^\pm$ in vector boson fusion, for which the signal rate and kinematics depend only on m_5 and s_H.

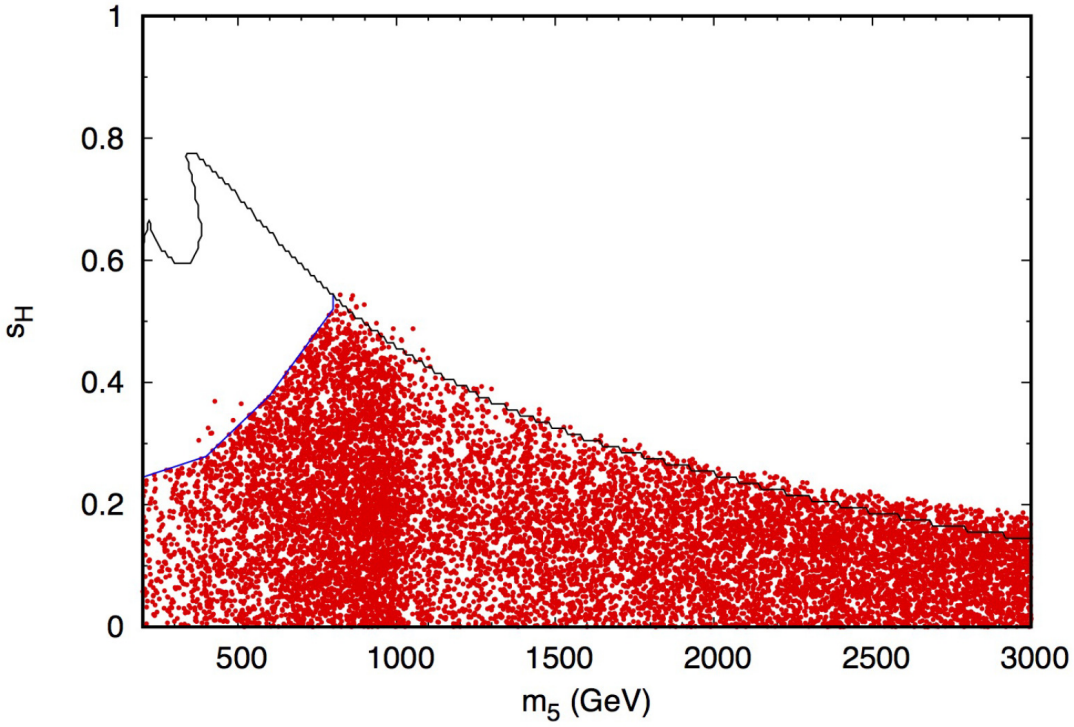

FIGURE 3.2: Theoretically and experimentally allowed parameter region in the $m_5 - s_H$ plane in the H5plane benchmark (entire region below black line) and the full GM model (red points) [49]. The black curve delimits the region allowed by theoretical constraints in the H5plane benchmark and the blue curve represents the upper bound on s_H from a direct search for $H_5^{\pm\pm}$ from Ref. [50].

CHAPITRE 4

THE ATLAS EXPERIMENT AT THE CERN LARGE HADRON COLLIDER

The Large Hadron Collider (LHC) is a circular superconducting hadron accelerator and collider located at the CERN in Geneva, Switzerland. It is primarily a proton-proton collider with a circumference of 27 kilometres providing up to 13 TeV collisions at a design luminosity of 10^{34} $cm^{-2}s^{-1}$. The LHC can also provide heavy ion collisions at 5.5 TeV per nucleon pair at a design luminosity of 10^{27} $cm^{-2}s^{-1}$. This unprecedented high energy and luminosity extend the frontier of particle physics.

The accelerator features four collision points where major detector experiments are located :

— ATLAS (A Toroidal LHC ApparatuS) and CMS (Compact Muon Solenoid) are general purpose detectors designed to be sensitive to a broad range of possible new physics signatures. These experiments provide precision measurements of the SM up to the TeV scale, study the electroweak symmetry breaking, search for the Higgs boson and the search for new physics beyond the Standard Model.

— ALICE (A Large Ion Collider Experiment) is primarily designed to study the lead-lead collisions of the LHC. The major goal of this experiment is the study of strongly interacting matter and to understand the properties of a new state of matter known as the quark-gluon plasma.

— LHCb (LHC Beauty) is designed to record the decay of particles containing b and anti-b quarks, also known as "B mesons". One of the major goals of LHCb is the search for signs of CP-symmetry violation in B decays in order to understand the particle/anti-particle asymmetry of the universe.

First, some basic aspects of the LHC complex are presented followed by a more detailed presentation of the ATLAS detector as this thesis relies on data collected with this detector.

4.1 The Large Hadron Collider

The LHC was installed in the existing tunnel that was constructed for the Large Electron-Positron Collider (LEP) experiment [51]. The tunnel lies between 45 and 170 m underground. The existing tunnel was then used to install the four major experiment of the LHC, ATLAS, CMS, ALICE and LHCb. The layout of the LHC can be seen in figure 4.1. The protons go through a sequence of accelerators before entering the LHC, first the LINAC 2 (LINear ACcelerator), the PS (Proton Synchrotron) and the SPS (Super Proton Synchrotron) to acquire initial energy of 450 GeV. The final acceleration up to 13 TeV is then performed in the LHC accelerator.

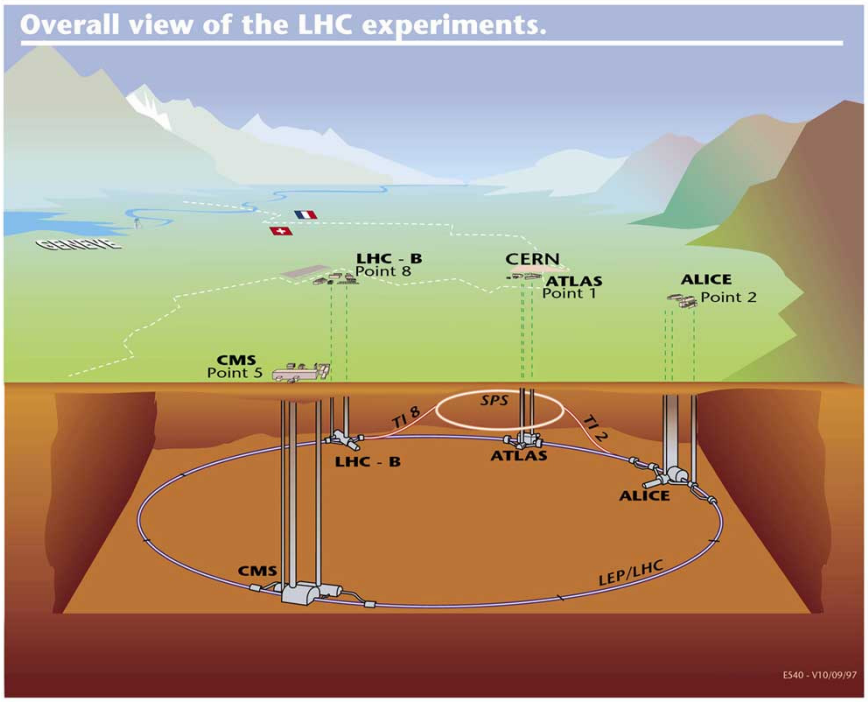

FIGURE 4.1: Overall view of the LHC experiments. [52]

The design objective of the LHC is to accelerate bunches of protons to 14 TeV and a peak luminosity of $10^{34}\text{cm}^{-2}\text{s}^{-1}$[51]. In 2008 however a mechanical failure in the superconducting magnets resulted in a huge release of helium into the tunnel [53] resulting in a prolonged shutdown. To minimise the risk of similar problems it was decided to lower the centre-of-mass energies to 7 TeV for 2010-2011. This was later

raised to 8 TeV in 2012 and further to 13 TeV in 2015. The period 2010-2012 with lower energies is referred to as run 1, the run periods with 13 TeV from 2015 to 2018 are referred to run 2. An overview of the delivered luminosity of all run years ranging from 2011 to 2018 is shown in figure 4.2. As can be seen from this figure, the recorded luminosity by the ATLAS experiment has been rapidly increasing every year.

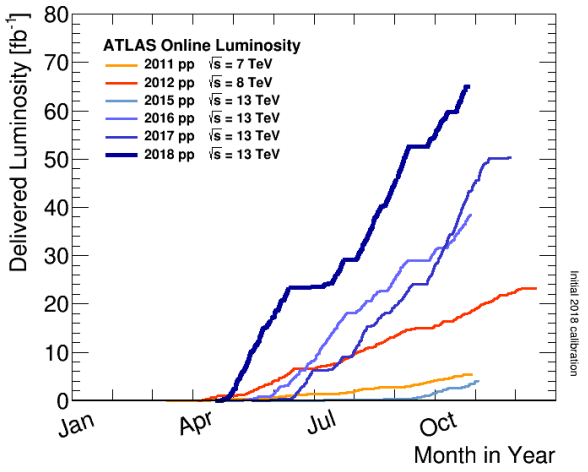

FIGURE 4.2: Cumulative integrated luminosity obtained in 8 years of data taking by the ATLAS experiment [54].

The LHC instantaneous luminosity can be calculated by the following equation [51] :

$$L = \frac{N_1 N_2 f_{\text{rev}} n_b}{4\pi\sigma_{x,y}^2}\,, \tag{4.1}$$

where $\sigma_{x,y} = \sqrt{\epsilon_n \beta^*}$ is the root mean square (RMS) cross-sectional size of the beam and ϵ_n the normalised transverse beam emittance, β^* the beta function (related to the transverse size of the beam) at the collision point. N_1 and N_2 are the number of particles in each colliding bunch, f_{rev} the revolution frequency, and n_b the number of bunches per beam. With an improved understanding of the LHC machine, the instantaneous luminosity was able to surpass the design goal in 2015, as seen in figure 4.3, and even consistently obtain peak luminosities of twice the design-value in 2018.

The increase in luminosity however also resulted in a substantial increase in the average number of interactions per bunch crossing $< \mu >$, as seen in figure 4.4, from

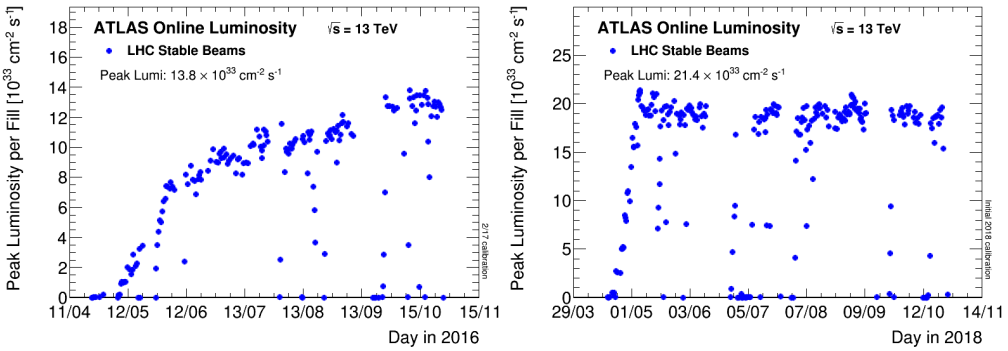

(a) (b)

FIGURE 4.3: Peak luminosity as a function of time obtained in 2015 (a) and 2018 (b) by the LHC. [54]

2015 ($< \mu >= 13.4$) to 2018 ($< \mu >= 37$). New techniques needed to be developed to reduce the undesirable effects of minimum-bias events overlaying the hard-scattering events. Some of these techniques will be discussed in Chapter 5.

Now that some of the basic concepts of the LHC operation have been presented, we will turn to a description of the ATLAS detector.

4.2 The ATLAS Detector

ATLAS is a general-purpose detector experiment at LHC [55]. The detector is designed to study a wide variety of physics at energies spanning several magnitudes, from low-energy diffractive Quantum Chromodynamics (QCD) to exploring the TeV scale in search of signs of new phenomena. The ATLAS detector is a detector with cylindrical geometry. The overall ATLAS detector layout is shown in figure 4.5, it is a huge detector with a length of 44 m and a height of approximately 25 m and a nearly 4π solid angle coverage [1]. The inner detector layers are built of silicon pixels, silicon strips and small drift tubes. All these layers are designed to measure the trajectory and momentum of

1. ATLAS uses a right-handed coordinate system with its origin at the nominal Interaction Point (IP) in the centre of the detector and the z-axis along the beam pipe. The x-axis points from the IP to the centre of the LHC ring and the y-axis points upwards. Cylindrical coordinates (r, ϕ) are used in the transverse plane, ϕ being the azimuthal angle around the z-axis. The pseudorapidity is defined in terms of the polar angle θ as $\eta = -\ln\tan(\theta/2)$. Angular distance is measured in units of $\Delta R \equiv \sqrt{(\Delta\eta)^2 + (\Delta\phi)^2}$.

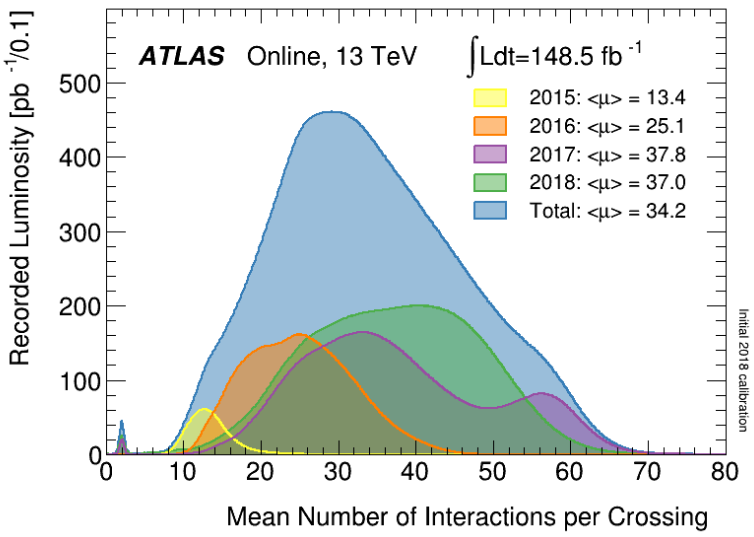

FIGURE 4.4: Average number of interactions per bunch crossing for the full run-2 data-taking period. [54]

charged particles in a 2 T magnetic field of the solenoidal magnet. Outside of the inner detector sits the calorimeter system. It is divided into an electromagnetic and hadronic calorimeter, using liquid argon and tile scintillator technologies, designed to measure the energy and direction of electrons, photons and hadrons. In addition, missing transverse momentum (perpendicular to the beam line) carried out of the detector by particles that interact little or not all with the detector, e.g. neutrinos, can be inferred by combining the measurement of all other particles and exploiting the fact that colliding protons have negligible transverse momentum. The muon spectrometer constitutes the outermost layers, which combines direction, momentum, and charge measurement (tracking) from monitored drift tubes and cathode strip chambers with resistive plates for triggering, and thin gap chambers in order to measure the trajectory and momentum of muons as they pass through a magnetic field. All specification are taken from [55].

4.2.1 Physics requirements

Requirements for the ATLAS detector system have been defined primarily in light of two important searches, the Standard Model (SM) Higgs boson and new phenomena

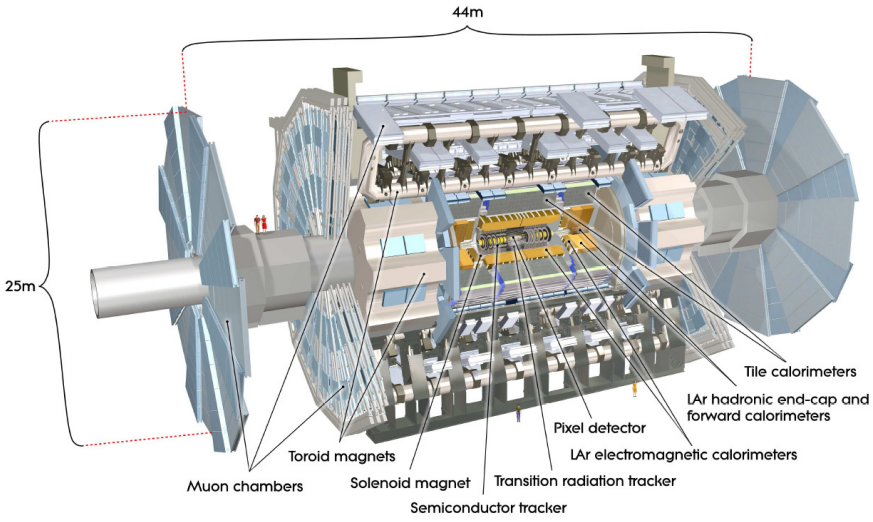

FIGURE 4.5: Overview of the ATLAS detector with its main components. [55]

hoped to be observed at the TeV scale [55]. Regarding new phenomena, searches for Higgs boson beyond the SM, for example, require sensitivity to processes involving τ-leptons and good identification of jets originating from bottom quarks (b-tagging). To be able to search for new heavy gauge bosons W' and Z' high-resolution lepton measurements and charge identification are needed in the transverse momentum (p_T) range of a few TeV. A high luminosity is needed as most of the processes mentioned above are expected to have very small cross-sections.

4.2.2 Inner Detector

The ATLAS Inner Detector (ID) is the primary detector for charged particle tracking and reconstruction of interaction points (vertexing). The layout of the ID can be found in figure 4.6. The ID has a cylindrical geometry directly surrounding the beam-pipe with a radius of 1150 mm and length a total length of about 7 meters. The ID is immersed in a 2 T solenoidal magnetic field that provides the bending necessary for momentum measurements. Three independent and complementary sub-detectors are used in the ID. The closest detector to the beam-pipe is the semiconductor pixel detector which is composed of silicon pixels and typically provides three high precision space-point

measurements. Surrounding the pixels are stereo pairs of silicon microstrip (SCT) layers, which is a silicon strip detector that typically provides eight high precision measurements along a particle's trajectory. Outside of the SCT is the Transition Radiation Tracker (TRT), which is built from a large number of small gaseous straw tubes with interleaved transition radiation material. This detector provides in average 36 measurements allowing continuous tracking and discrimination between electrons and pions. In 2013 a new pixel layer was installed at the ATLAS experiment, named Insertable B-Layer (IBL) [56]. The IBL is designed to maintain the performance in tracking, vertex reconstruction and b-tagging, hence the name, with regard to the high number of interaction per bunch-crossing, referred to as pile-up, when going to peak luminosity of $\mathcal{L} \approx 1x10^{34}\text{cm}^{-2}\text{s}^{-1}$. The IBL layer is now the closest detector to the beam pipe.

A Large LHC ApparatuS (ATLAS) parameterises its tracks using the following quantities to define their trajectory :

— the particle charge and the transverse momentum, q, pT ;

— longitudinal and transverse impact parameters, z_0 and d_0 ;

— polar and azimuthal angles, θ and ϕ.

The purpose of the ID is to provide accurate and efficient charged particle tracking for tracks with $p_T > 0.5$ GeV with nearly complete coverage out to $|\eta| < 2.5$ combined with pattern recognition in the dense environments of LHC collisions. The ID is also designed to allow for the reconstruction of primary vertices from pp collisions and secondary vertices from the decay of long-lived particles (such as K_s, Δ_0, τ, and heavy flavour quarks in jets). In order to achieve this performance, the ID is designed as a highly granular detector with radiation hardness. However, as for all tracking systems, the ID must maintain as low as possible material budget so as not to deteriorate tracking resolution from multiple scattering or cause significant energy loss before the energy measurements of the ATLAS calorimeters. Therefore the detector is split into a dense pixel and SCT detector, and a low material-budget TRT as a compromise between maximal precision and low material budget. The pixel detector provides precise η and ϕ measurements to allow for accurate determination of the location and angle with which tracks emerged from the collisions, while the TRT is optimised for momentum

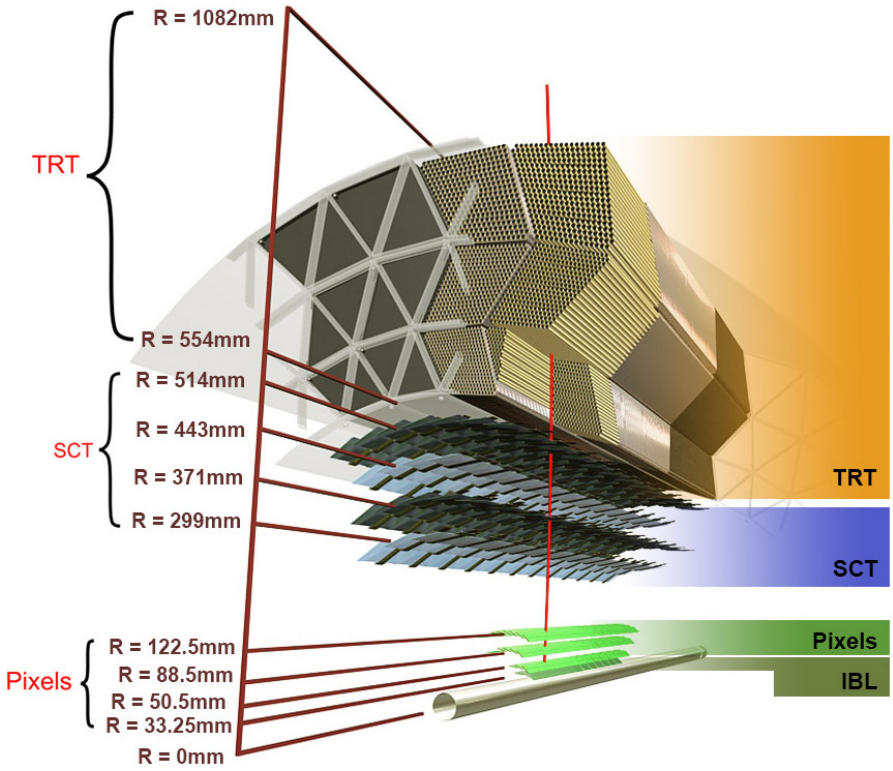

FIGURE 4.6: Cut-away view of the ATLAS inner detector showing the Pixel, including the IBL, SCT, and TRT detectors with their respective distance to the centre of the beam pipe. [57]

measurements by providing a large number of hits over a large bending radius.

4.2.3 Calorimeter

The ATLAS calorimeter is composed of an electromagnet and hadronic sampling detectors providing accurate energy measurements of various particles like electrons, photons, taus, hadrons and jets. The measurements of the calorimeter energy depositions are also used in the calculation of the transverse missing energy caused by very weakly-interacting particles escaping detection, such as neutrinos. The electromagnetic (EM) calorimeter sits directly outside of the ID and solenoid magnet. It is split into a barrel and end-cap and is composed of liquid Argon (LAr) with lead absorber plates. The EM calorimeter provides nearly complete coverage in ϕ and it covers $|\eta| < 3.2$. The hadronic calorimeter, sitting outside of the EM calorimeter, measures the energy and direction of charged and neutral hadrons in jets. The hadronic calorimeter utilises tile scintillators with steel absorbers for $|\eta| < 1.7$ while the end-cap uses LAr with copper absorber for $1.5 < |\eta| < 3.2$. To also have coverage in high η region, a forward calorimeter using LAr with tungsten absorber provides measurements from $3.1 < |\eta| < 4.9$. The layout of the whole calorimeter system can be seen in figure 4.7.

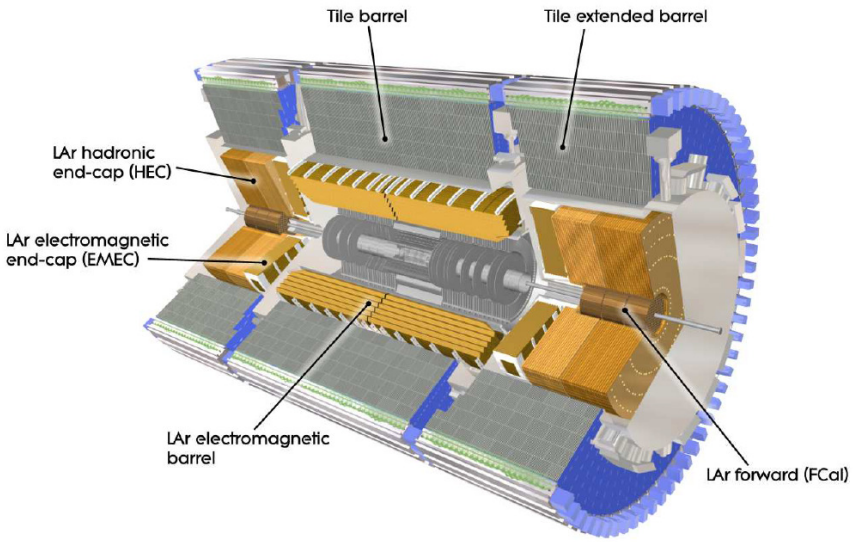

FIGURE 4.7: Cut-away view of the ATLAS calorimeter system. [55]

4.2.4 Muon Spectrometer

The design of the ATLAS Muon Spectrometer (MS) is based on four detector technologies with the aim of providing accurate muon direction and momentum measurements as well as efficient triggering on muons with momenta from a few GeV up to several TeV. The layout of the MS and toroid magnets can be found in figure 4.8. The MS sits outside of the calorimeter system and constitutes the overall envelope of the ATLAS detector. Measurements rely on the magnetic deflection of muon tracks in the large superconducting toroid magnets, which are instrumented with separate trigger and high-precision tracking chambers.

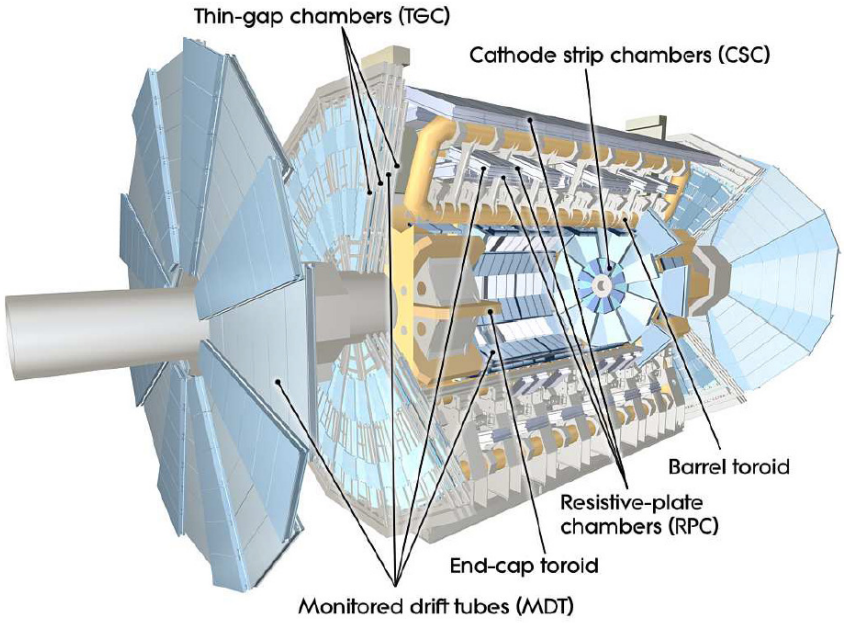

FIGURE 4.8: Cut-away view of the ATLAS muon system. [55]

The primary precision tracking measurements in the bending direction are provided by monitored drift tubes. In the forward region, where the particle flux is too high for drift tubes, cathode strip chambers are used. Triggering is provided by Resistive Plate Chamber (RPC) and Thin Gap Chambers (TGC). Both detectors have excellent time resolution and provide the first level of muon triggering.

4.2.5 Trigger and Data Acquisition

The ATLAS trigger is built in three levels : the Level-1 trigger (L1), the Level-2 trigger (L2), and the event filter (EF). The L1 trigger is hardware based, relying on the RPC and TGC for muon triggers and the calorimeter for triggering on EM clusters, jets, taus, and missing energy. The L1 system uses custom electronics to ensure fast triggering. The L1 trigger is designed to have a $\approx$ 100 kHz output rate. The L2 trigger and the event filter form the High-Level-Trigger, which is primarily based on commercially available computers and network hardware. The L2 trigger uses Regions-of-Interest (RoI) identified by the L1 trigger, which is a subset of the detector information and reduces the data volume to be handled by the L2 trigger. Fast reconstruction algorithms are performed on the data in the RoI to allow for more precise trigger decisions. The L2 has an output rate of $\approx$ 4 kHz. The EF uses the full detector information and is based on the analysis of fully reconstructed events. The current output rate of the EF is approximately 400 Hz.

The ATLAS data acquisition (DAQ) system controls the data flow, configures and controls the hardware, and monitors the detectors. The DAQ takes data selected by L1 and sends the data corresponding to RoI to the L2 trigger. Finally, the DAQ reconstructs events selected by L2 and sends them to EF. The DAQ system also allows monitoring of all of these steps.

4.2.6 Grid Computing

In order to cope with the enormous amount of data from the LHC detectors the Worldwide LHC Computing Grid (WLCG) [58] was developed to support LHC data processing and analysis. The ATLAS detector, for example, generates approximately 1 PB s^{-1} of data, however most of these are not interesting for data analysis, and the trigger system described in the previous section reduces this to a data rate of a few hundred megabytes per second which are sent to the CERN Computer Center for archiving. The LHC computing system must handle approximately 15 PB of new data every year of operation. The first distributed computing system was named the MONARC model [59], created in 1999.

Today the project is known as the Worldwide LHC Computing Grid (WLCG). The Tier 0 sites are located directly at CERN : 13 Tier 1 sites are distributed around the world and ≈150 Tier 2 sites are located at various institutes and laboratories. Tier 1 and 2 provide resources for all members of the experiment while Tier 3 may be national or local and available only to members of the experiment at that particular site. The Canadian Tier 1 site is located at TRIUMF.

4.2.7 Particle Reconstruction

Complex reconstruction algorithms are used to optimise the detector's response and accurately measure particle type, charge and 4-momenta. Some of the most important algorithms for the WZ resonance search performed in Chapter 5 are briefly described here.

4.2.7.1 Electron Reconstruction and Isolation

The calorimeter based reconstruction of electrons and photons are virtually identical. The obvious difference is that most photons are not associated with any ID track, except those that undergo conversion to electron-positron pairs in the ID. Since in the following analysis only electrons are used, we concentrate on the electron reconstruction.

Electron candidates are reconstructed from energy deposits in the EM calorimeter which are matched to a well-reconstructed ID track originating from the primary vertex. The electron identification is based on a likelihood-based (LH) method evaluated from a multivariate discriminant [60]. In order to select the electron candidates from background – such as hadrons and background (non-prompt) electrons originating predominantly from photon conversions and heavy flavour hadron decays – several sets of identification criteria are used with different levels of background rejection and signal efficiency. These identification criteria rely for example on the shapes of electromagnetic showers in the calorimeter as well as on tracking and track-to-cluster matching quantities. With these variables, signal and background probability density functions (PDFs) are built. Based on these PDFs, an overall probability is calculated for the object to be signal or

background. Three levels of operating points are provided for electron ID. These are referred to as *Loose, Medium,* and *Tight*. Each point uses the same variables but different LH discriminants. The operating points are defined such that the samples selected by them are subsets of one another. Therefore the *Medium* (*Loose*) selection includes all *Tight* (*Medium*) electrons.

Additionally, electrons can be required to be isolated from other activity in the calorimeter or inner detector to further distinguish them from background objects. The isolation variables quantify the energy of the particles produced around the electron candidate and allow to disentangle prompt electrons (from heavy resonance decays, such as $W \rightarrow e\nu$, $Z \rightarrow ee$) from other, non-isolated electron candidates such as electrons originating from converted photons or from jets, electrons from heavy flavour hadron decays, and light hadrons mis-identified as electrons. Two types of discriminating variables are commonly used :

— calorimetric isolation based on the variable $E_{\mathrm{T}}^{\mathrm{cone0.2}}$, defined as the sum of transverse energies of topological clusters in a cone of radius $R = 0.2$, where R is defined according to footnote 1 ;

— a track isolation, $p_{\mathrm{T}}^{\mathrm{varcone0.2}}$, defined as the sum of transverse momenta of all tracks, satisfying the quality requirements, which are within a cone of $\Delta R = \min(0.2, 10\ \mathrm{GeV}/E_{\mathrm{T}})$ around the electron, excluding the track of the electron itself and which are originating from the reconstructed primary vertex.

Several operating points have been defined both for $E_{\mathrm{T}}^{\mathrm{cone0.2}}$ and $p_{\mathrm{T}}^{\mathrm{varcone0.2}}$:

— efficiency targeted operating points : varying requirements are used to obtain a given isolation efficiency e_{iso} in simulated $Z \rightarrow ee$ events. Typical e_{iso} values are 90 and 99%.

— fixed requirement operating points : in this case the upper thresholds on the isolation variables are constant. These operating points were optimised by maximising the expected sensitivities of $H \rightarrow 4\ell$ and multilepton supersymmetry searches.

4.2.7.2 Muon Reconstruction and Isolation

Muons are reconstructed by combining tracks from the inner detector with tracks from the muon spectrometer. As for the electrons there are three selections (*Loose, Medium* and *Tight*) [61]. The *Medium* operating point is the default selection for muons at ATLAS. *Loose* selection maximises reconstruction efficiencies while providing good-quality muon tracks. They are optimised for reconstructing Higgs boson candidates in the four-lepton final state. Lastly, *Tight* muons are selected to maximise the purity of muons at the cost of some efficiency. The efficiency measurements were obtained with simulated $Z \to \mu\mu$ and $J/\Psi \to \mu\mu$ events.

Prompt muons originating from the decay of heavy particles, such as W, Z, or Higgs bosons, are often produced isolated from other particles. Muons from semileptonic decays of heavy flavour mesons on the other hand are often embedded in jets. The measurement of the detector activity around a muon candidate, referred to as muon isolation energy, is therefore a powerful tool for background rejection in many physics analyses. As for the electrons, two variables are defined to assess the isolation of the muons, a track-based isolation variable and a calorimeter based isolation variable.

— a calorimetric isolation based on the variable $E_{\mathrm{T}}^{\mathrm{topocone20}}$, defined as the sum of transverse energies of topological clusters in a cone of size $\Delta R = 0.2$ around the muon ;

— a track isolation, $p_{\mathrm{T}}^{\mathrm{varcone30}}$, defined as the sum of transverse momenta of all tracks with $p_{\mathrm{T}} > 1$ GeV, satisfying the quality requirements, which are within a cone of $\Delta R = \min(0.3, 10\ \mathrm{GeV}/p_{\mathrm{T}}^{\mu})$ around the muon, excluding the track of the muon itself.

The track isolation gives 99% efficiency, independently of η or p_{T}^{μ}, in $Z \to \mu\mu$ samples.

4.2.7.3 Jet Reconstruction

Jet clustering algorithms are among the most important tools for analysing data from hadronic collisions. Several algorithms have been used at the LHC, which can essentially

be divided into two classes of jet reconstruction algorithms : cone-type algorithms (e.g. [62]) and clustering algorithms (for example the kt [63] and Cambridge/Aachen[64, 65] algorithm). In cone-type algorithms, jets are identified by maximizing the amount of energy which can be covered by cones of fixed size, whilst in clustering algorithms particles are assigned to jets iteratively.

Clustering algorithm have two main ingredients : a test variable y_{ij} and a combination procedure. The test variable is used to decide whether the objects i and j should be combined, according to whether $y_{ij} < y_{cut}$. For the test variable, a distance measure $y_{ij} = d_{ij}$ within a predefined jet radius R is defined as [66] :

$$d_{ij} = \min \left[\left(k_{ti}^2\right)^p, \left(k_{tj}^2\right)^p \right] \frac{\Delta_{ij}^2}{R^2}, \tag{4.2}$$

where $\Delta_{ij}^2 = (y_i - y_j)^2 + (\phi_i - \phi_j)^2$, y_i and ϕ_i are respectively the rapidity and azimuth of particle i, and k_{ti} is the transverse momentum of object i. The parameter p governs the relative power of the energy versus geometrical (Δ_{ij}) scales. For $p = 1$ one recovers the k_t algorithm. For $p = 0$, one obtains the Cambridge/Aachen algorithm [64, 65]. Negative values of p might seem arbitrary, but using negative values has some advantages over positive. The behaviour with respect to soft radiation is similar for all $p < 0$, and $p = -1$ is generally referred to as the "anti-kt" jet-clustering algorithm [66].

A second distance d_{iB} is defined, measuring the distance between entity i and the beam (B), to differentiate *hard final-state jets* from jets associated with the beam. In the anti-kt algorithm, it is simply defined as the momentum of object i, $d_{iB} = k_{ti}^{-2}$. Then, objects are combined as long as the smallest distance d_{ij} between object i and object j is smaller than d_{iB}. Object i is often called a *pseudojet*, since it is neither a particle, nor a full jet yet. If all distances $d_{ij} \geqslant d_{iB}$, then the pseudojet is called a jet and removed from the list of entities. This procedure is repeated until no entity is left.

Here a simple illustration of how one ends up with conical jets in the anti-kt algorithm. Consider an event with a few well-separated hard particles with transverse momenta $k_{ti}, k_{tj}, \ldots$ and many soft particles. The distance d_{1i} (eq. 4.2) between a hard particle 1 and a soft particle i is determined by the transverse momentum of the hard particle and

their separation Δ_{1i} and is in general small. The distance between similarly separated soft particles will instead be much larger, due to the inverse momentum relation. Therefore soft particles will tend to cluster with hard ones rather than among themselves. If a hard particle has no hard neighbours within a distance $2R$, then it will simply accumulate all the soft particles within a circle of radius R, resulting in a perfectly conical jet.

If another hard particle 2 is present such that $R < \Delta_{12} < 2R$ then there will be two hard jets. It is obviously not possible for both to be perfectly conical. If $k_{t1} \gg k_{t2}$ then jet 1 will be conical and jet 2 will be partly conical since it will miss the part overlapping with jet 1. Instead, if $k_{t1} = k_{t2}$ neither jet will be conical and the overlapping part will simply be divided by a straight line equally between the two. In a general situation, $k_{t1} \sim k_{t2}$, both cones will be clipped.

The key feature above is that the soft particles do not modify the shape of the jet, while hard particles do. This means the jet boundary is resilient with respect to soft radiation but flexible with respect to hard radiation. For an illustration of the various algorithms mentioned above see Figure 4.9. For each of the hard jets, the region is shown within which the random soft contributions are clustered into that jet. We can see that anti-k_t forms more circular jets compared to the other algorithms. Since it is also infrared [2] and collinear [3] safe it is the preferred algorithm for most ATLAS analysis.

4.2.7.4 $E_{\mathrm{T}}^{\mathrm{miss}}$ Reconstruction

The missing transverse momentum, $\boldsymbol{p}_{\mathrm{T}}^{\mathrm{miss}}$, and its magnitude $E_{\mathrm{T}}^{\mathrm{miss}}$ are the main physics quantities used to infer the presence of particles that leave no signal in the detector. Due to the complex structure of hadrons, the initial momentum of the colliding partons along the beam axis is not known, so only the conservation of momentum projected in the plane transverse of the colliding beams for each event can be exploited.

Particles leaving the detector without energy deposition result in an imbalance in the sum of visible transverse momenta of reconstructed physics objects. Large $E_{\mathrm{T}}^{\mathrm{miss}}$ results generally from SM neutrinos but is also a sign of new particles suggested in models

2. Infrared-safe : Jets reconstruction insensitive to soft parton emissions.
3. Collinear-safe : Jets reconstruction insensitive to collinear parton splitting.

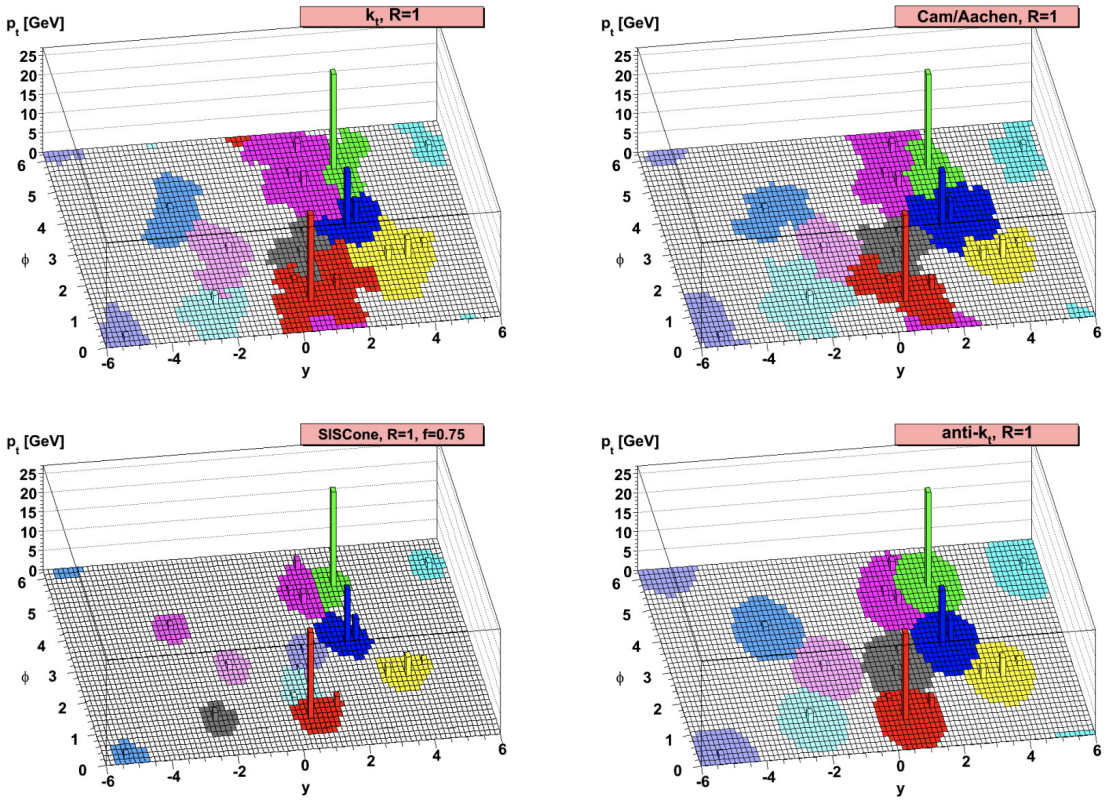

FIGURE 4.9: A few parton-level events together with many random soft contributions, clustered with four different jets algorithms, illustrating the "active" catchment areas of the resulting hard jets. [66]

for physics beyond the SM. The reconstruction is challenging since it involves all of the ATLAS detector subsystems.

The reconstructed $E_{\mathrm{T}}^{\mathrm{miss}}$in ATLAS is characterised by two contributions : The first from the *hard-event* signals, constituted by fully reconstructed and calibrated particles and jets and from *soft-events*, consisting of reconstructed charged-particle tracks associated with the hard-scatter vertex [67, 68]. The missing transverse momentum components $E_{x(y)}^{\mathrm{miss}}$ serve as the basic input for most of these observables given by :

$$E_{x(y)}^{\mathrm{miss}} = -\sum_{i\in\{\text{hard objects}\}} p_{x(y),i} - \sum_{j\in\{\text{soft objects}\}} p_{x(y),j} \tag{4.3}$$

From these, the observable $E_{\mathrm{T}}^{\mathrm{miss}}$can be constructed as :

$$\boldsymbol{p}_{\mathrm{T}}^{\mathrm{miss}} = (E_x^{\mathrm{miss}}, E_y^{\mathrm{miss}}), \tag{4.4}$$

$$E_{\mathrm{T}}^{\mathrm{miss}} = |\boldsymbol{E}_{\mathrm{T}}^{\mathrm{miss}}| \tag{4.5}$$

4.3 Future Upgrades of the Detector

A brief description is given here of future upgrades, in particular the Inner Tracker (ITk), for which I have worked on the optimisation of the track reconstruction.

The LHC has operated in Run 2 at 13 TeV centre-of-mass energy from 3 June 2015 and has progressively increased the luminosity attaining the nominal design luminosity of 1×10^{34} cm^{-2}s^{-1} on 26 June 2016 and surpassing it regularly ever since. Run-2 came to an end in December 2018 followed by the Long Shutdown 2 (LS2) (see schedule shown in figure 4.10). Excellent performance over the whole run period, together with high availability, allowed the LHC to deliver a total integrated luminosity of about 158 fb^{-1}, of which ATLAS recorded 149 fb^{-1} for the whole run-2 period. Run-2 is followed by a two-year LS2. This will be followed by run-3, where the centre-of-mass energy will likely be raised to 14 TeV and with a projected 2-3 times the nominal luminosity. A total integrated luminosity of 300 fb^{-1} would be collected in three years of operation ending in 2023. By then the ATLAS inner detector will have reached the end of its lifetime

due to the increased radiation damage. During the Long Shutdown 3 (LS3) the inner detector will therefore be completely replaced and the accelerator will be upgraded for High Luminosity operation. The goal is to run at 5 to 7 times the nominal luminosity and to obtain a total of 3000 fb^{-1} during a prolonged operation (Phase-II) until around 2035.

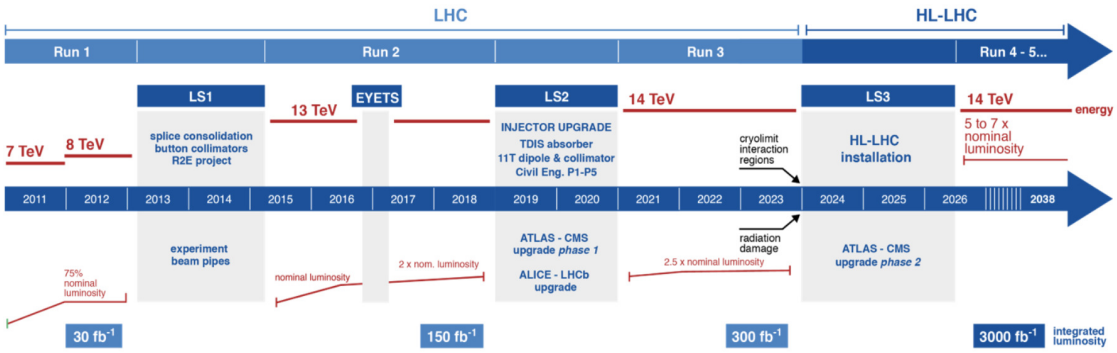

FIGURE 4.10: Project Schedule of the LHC going from LHC to HL-LHC [69].

4.3.1 Phase-I upgrade

During LS2 the main goal is to do maintenance and consolidation work to prepare the LHC for run-3 and beyond. The particle injectors will increase the intensity to be ready for High Luminosity LHC (HL-LHC) operation. ATLAS will perform the upgrade phase 1. The main project is the planned upgrade of the muon spectrometer. With the increased pile-up (mean interactions per beam crossing will be above 50), the muon spectrometer trigger rates, detector occupancy and momentum resolution would be highly affected [70]. In order to preserve tracking performance at high luminosity New Small Wheels (NSWs) are designed and built to replace the existing ones as part of the ATLAS Phase-I upgrade. The small wheel is located between the end-cap calorimeter and the end-cap toroid (see also figure 4.8). This new detector will provide track positions and angular resolution of better than 1 mrad to the Level-1 trigger.

The NSWs are disk-shaped arrangements of approximately 10 m in diameter. The NSW's sectors combine the small-strip Thin Gap Chamber (sTGC) [71] and Micromegas [72] technologies. Canada is contributing to the upgrade of the ATLAS NSW detector

with a consortium of four Canadian Universities (Carleton, McGill, SFU, and Victoria) as well as TRIUMF. Canada is building one-quarter of the sTGC chambers.

4.3.2 Phase-II upgrade

After Run 3 the statistical gain in running the accelerator without a significant luminosity increase beyond its design will become marginal. The running time necessary to halve the statistical error of a given measurement after 2020 will be more than ten years. Therefore, to maintain scientific progress and to exploit its full capacity, the LHC will need to have a decisive increase in its luminosity after 2020. The HL-LHC will start in the middle of 2026. The inner detector will be completely replaced during the LS3 as the current inner detector will have reached the end of its lifetime. The new ITk will be operational for more than 10 years and in that time ATLAS aims for a total data set of 3000 fb^{-1}. The HL-LHC will operate at an ultimate peak instantaneous luminosity up to $L = 7.5 \times 10^{34} cm^{-2} s^{-1}$ which corresponds to approximately 200 inelastic proton-proton collisions per beam crossing (pile-up). Meeting these requirements presents a unique challenge for the design of an all-silicon tracking system that will consist of a pixel detector at small radius close to the beam line and a large area strip tracker surrounding it [73]. A schematic view of the layout of the ITk is shown in figure 4.11.

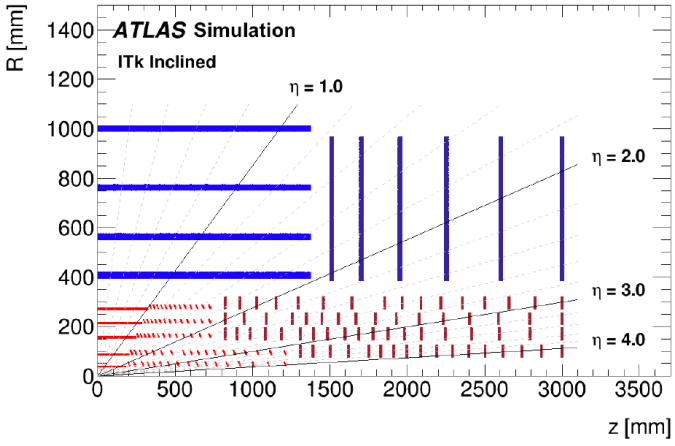

FIGURE 4.11: Schematic layout of the ITk for the HL-LHC phase of ATLAS. The horizontal axis is the axis along the beam line with zero being the interaction point. The vertical axis is the radius measured from the interaction point [73].

The general requirement for the ITk is to deliver equal or better tracking performance to that provided by the current ATLAS Inner Detector despite an average pile-up ($\langle\mu\rangle$) of up to 200 events. Tracks from the primary vertex need to be reconstructed up to a pseudorapidity (η) of 4.0. This will be achieved through a system of silicon barrel layers and disks (Strips) or rings (Pixels) with the possibility of inclined pixel modules to better cover the transition from the barrel to the end-cap regions. There are five layers in the barrel regions as well as four layers for the barrel strip-detector.

4.3.2.1 Expected tracking performance of the ITk detector

A comparison of the simulated efficiency for track reconstruction in $t\bar{t}$ events between the current (ATLAS - Run-2) and future detector (Inclined) assuming an average pile-up of 0 can be seen in figure 4.12(a). The tracking efficiency is defined as the fraction of prompt particles which are associated with tracks passing a track quality selection. More specifically it is the number of selected reconstructed tracks that match to a selected truth particle (from simulation), divided by the number of selected truth particles. We can conclude that the track efficiency is better than for the current detector for all values of η and the coverage is extended up to $|\eta|$ of 4.0. The dependence of the track reconstruction efficiency is small on the pile-up condition, as is shown in figure 4.12(b).

The resolutions for tracking parameters are obtained from simulation by comparing their reconstructed values for a given particle with the truth value. The resolution on track parameter d_0 and z_0 for single muons and various p_{T} values is shown in figure 4.13 for both the ITk and current detector. In general, the ITk resolution is better than for the current detector except for tracks with p_{T} of 100 GeV due to the usage of digital clustering and the larger inner radius of the first pixel detector layer.

4.3.2.2 Tracking in dense environment

The high centre-of-mass energy of the LHC leads to many very boosted objects, such as high-p_{T} jets. These jets produce high occupancy regions in the pixel detector where the separation between particles becomes comparable to the granularity of the pixel

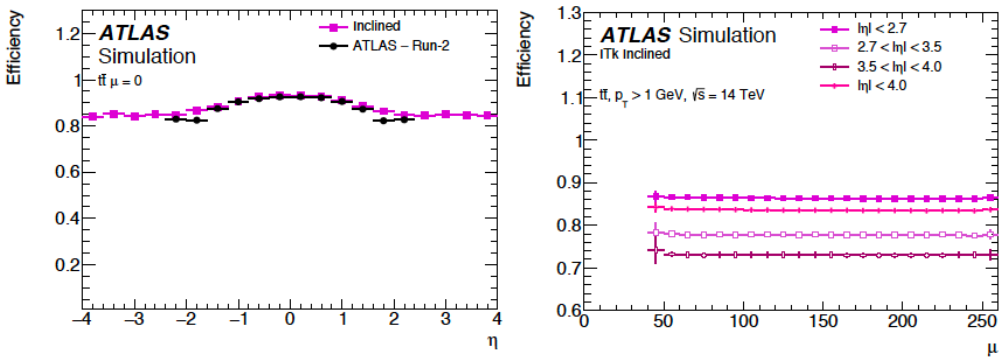

(a) (b)

FIGURE 4.12: Track reconstruction efficiency for particles as function of η in $t\bar{t}$ events with no pile-up (a) for the ITk detector (here referred to as Inclined) compared to the Run-2 efficiency. The dependence of the efficiency on μ is shown for different η-regions in (b) [73].

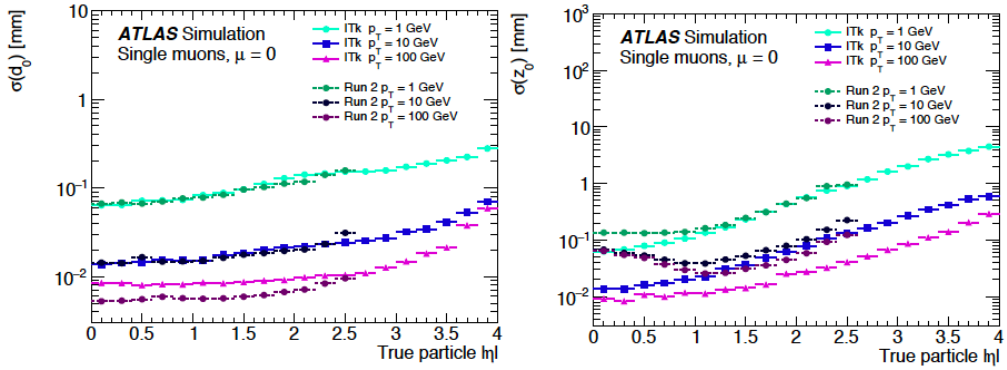

(a) (b)

FIGURE 4.13: Resolution on track parameters d_0 (a) and z_0 (b) as a function of true track η, for single muons with p_{T} of 1, 10, or 100 GeV, for $\langle\mu\rangle$. Results for Run 2 are shown for comparison [73].

detector. In these dense environments achieving high-performance tracking becomes challenging, as four precise charged-particle measurements (space-points) are needed. When a particle passes through the silicon detector, charge is commonly deposited in more that one pixel due to charge drift, creation of δ-rays, and the incident angle of the particle(see also Fig. 4.14). These charge depositions can overlap if the separation between the charged particles become small. This merging results in poor precision in the hit position estimate and degraded track reconstruction performance. To recover good performance neural networks are used to estimate the particle multiplicity, the hit position and the associated uncertainties respectively [1, 2].

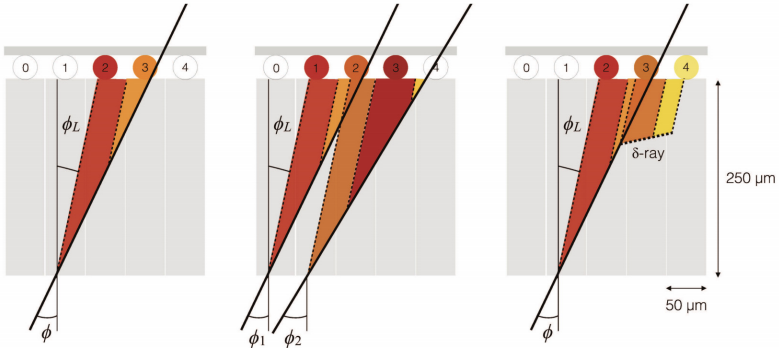

FIGURE 4.14: Production of charge clusters due to charge drift (left), small separation between charged particles (middle) and due to δ-rays (right) [2].

The track reconstruction is done in several steps : track seeding, track finding, ambiguity solving and lastly track fitting [2]. For the track seeding, track candidates are defined as sets of three space-points passing certain p_{T} and impact parameter cuts. The tracks are then found by using the Kalman filter to iteratively update track parameters starting from the seed and adding hits from other layers [74]. If more that one space-point on a layer is compatible with the track candidate, multiple candidates are created. Therefore there can be an excess of candidates which must be reduced using an ambiguity solver. Tracks are scored based on the quality of the track candidate if charge clusters are used by multiple tracks, the corresponding track candidates receive a penalty. In dense environment track sharing is however quite common, therefore neural networks are employed to identify clusters created by multiple particles and then allow the clusters to be shared

by the appropriate number of tracks. To perform track fits, position measurements must be performed for every particle in the cluster. This is done using a set of separate neural networks that estimate the local positions for each particle in a given cluster. A few examples of hit position estimated with neural networks are shown in figure 4.15.

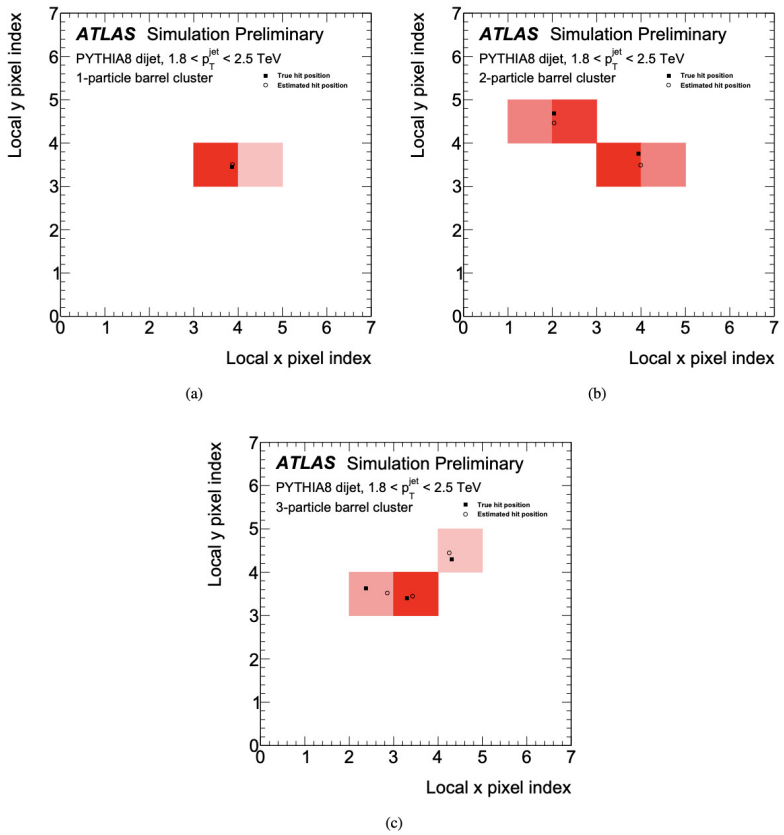

FIGURE 4.15: Examples of neural network hit position estimates for (a) 1-particle (b) 2-particle and (c) 3-particle clusters. The true hit positions are marked by full squares and the neural network estimations are marked by open circles [2].

Inputs to the neural networks are the measure of collected charge per pixel, the physical location of the pixels in the detector as well as the estimated incident angle of the particles. As the networks require the inputs to be in fixed dimensions, the charge is collected in rectangular 7×7 matrices. One example of the improved performance for high p_{T} jets is shown in figure 4.16, where the track reconstruction is compared for a baseline reconstruction without neural networks and for an optimised selection using neural networks. It is evident, that especially for high p_{T} jets, the reconstruction efficiency

is largely improved.

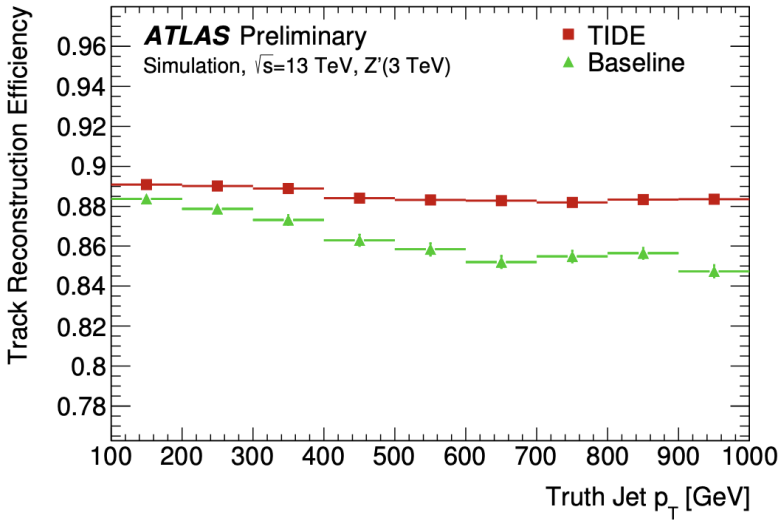

FIGURE 4.16: The average efficiency to reconstruct primary tracks in jets as a function of jet p_{T} . Two track reconstruction algorithms are shown : green triangles label the baseline reconstruction (no neural network) and red squares label the TIDE (tracking in dense environment) optimised reconstruction using neural networks [75].

Since the current inner detector will be completely replaced by the ITk detector in the Phase-II upgrade, the neural networks need to be adapted to the new geometry and retrained. This was my task during the first year in the collaboration. Neural networks were successfully trained with simulation using the ITk geometry and good performance was observed to estimate the number of particles in clusters and the hit position. However, since the layout of the detector was continuously evolving, no final performance figures and estimates were obtained.

CHAPITRE 5

SEARCH FOR WZ RESONANCES

This chapter describes the analysis for the search for resonant WZ production in the fully leptonic final state $\ell\nu\,\ell\ell$ (where $\ell = e, \mu$) with 36 fb^{-1} of data recorded by ATLAS in 2015 and 2016 with 13 TeV centre-of-mass energy.

The search has two distinct search regions corresponding to the two production modes of the resonances, either by quark-antiquark ($q\bar{q}$) fusion or by Vector Boson Fusion (VBF). The VBF category is a new addition compared to the run-1 analysis [76], since a large dataset and high centre-of-mass energy are necessary to have sensitivity in this channel. It searches for two benchmark models, the Georgi-Machacek (GM) model detailed in section 3.4 and the Heavy Vector Triplet (HVT) implementation detailed in section 3.3.

The fully leptonic final states provide very clean final states with good resolution. Therefore despite the low branching fraction, this decay mode has higher sensitivity at low resonance masses compared to semi- or fully-hadronic decays [77]. Hypothetical signals for both production modes are depicted in the Feynman diagrams in figure 5.2. The main backgrounds for WZ production and for electroweak (EW)- and Quantum Chromodynamics (QCD)-induced $WZjj$ production are shown in figure 5.1.

5.1 Phenomenology of the search and previous results

The two benchmarks that are considered in this search, HVT and GM, predict specific couplings that determine how one can look for the predicted resonances. In the following section, a short overview of the predictions is presented, which has already been mentioned in sections 3.3.3 and 3.4.

The relevant couplings of the HVT models are c_H, the coupling strength to vector bosons, c_f the couplings to fermions and the overall coupling strengths g_V and g. If c_f is non-zero, than the resonance can be produced via quark-antiquark fusion, as shown in figure 5.2(a). If a W' resonance can be produced by fermions, then it can of course

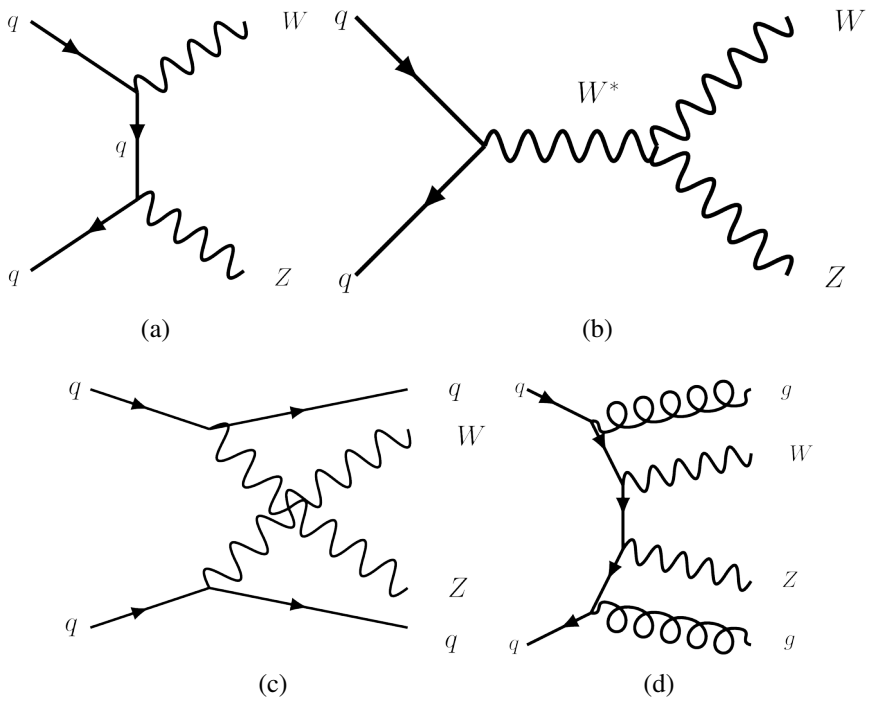

FIGURE 5.1: Some representative Feynman diagrams for WZ and $WZjj$ production in the SM. (a) and (b) shows two of the diagrams contributing to WZ production, $WZjj$ by EW-induced production includes quartic interaction (c) of the vector bosons and QCD-induced production (d).

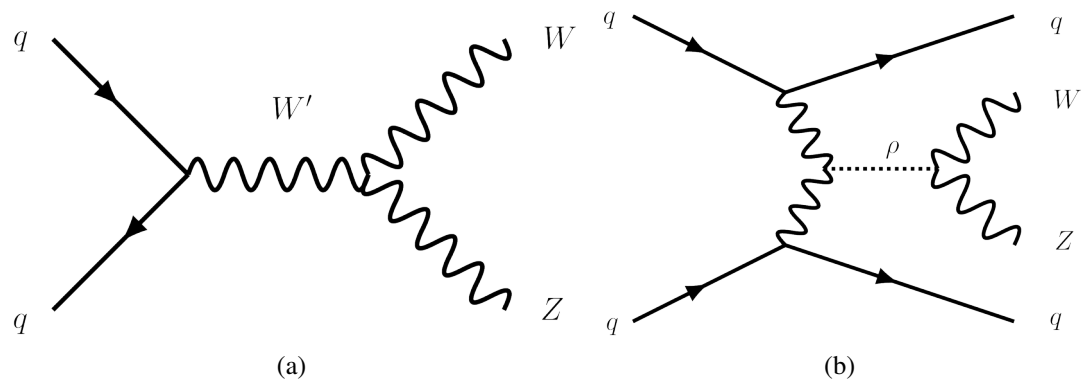

FIGURE 5.2: (a) shows a representative Feynman diagrams for resonant WZ production with a W' of the HVT benchmark model, (b) shows resonant $WZjj$ production via a resonance ρ, which could be either a W' of the HVT model or a and $H_5^{\pm}$ of the GM model.

also directly decay to these. Searches have therefore been performed looking for heavy resonances decaying to a pair of leptons ($\ell\nu$) by both ATLAS [78–80] and CMS [81, 82] as well as decaying to a pair of quarks [83, 84] with limits in the $\sim 3-5$ TeV range, when assuming couplings to other particles identical for the W' and for the Standard Model (SM) W boson. Resonance searches decaying to vector bosons become competitive for weakly coupled scenarios where c_H is important, as, for example, in HVT model B. Searches are performed in all of the decay channels of the WZ bosons, so the fully hadronic ($qqqq$) and semi-hadronic ($\ell\ell qq, qq\ell\nu, \nu\nu qq,$) [85, 86], as well as the fully leptonic ($\ell\nu\ell\ell$) final state, which is presented here. This analysis extends the Run 1 $WZ \rightarrow \ell\nu\ell\ell$ analysis performed by both ATLAS [76] and CMS [87] at $\sqrt{s} = 8$ TeV. Both these analyses put limits on parameters of the HVT A and HVT B model and exclude a W' below ~ 1.5 TeV.

For most parameter model values, the production rate via quark-fusion dominates over the VBF rate. Therefore, resonant searches in the VBF mode do not significantly add to the sensitivity of the search. If, however, the heavy resonance only couples to vector bosons, meaning $c_f = 0$, then the only possible production will be via VBF (see diagram 5.2(b)). As mentioned above, a new resonance search in the VBF-mode was added to the analysis compared to the run-1 analysis. In order to have sensitivity in this search, a new benchmark model was designed specifically for this production mode with the parameters $c_f = 0$ and $c_H = 1$.

In the case of the GM model, the members of the fiveplet only couples to vector bosons, therefore, VBF is the only possible production mode. Since all members of the fiveplet are degenerate at tree level, limits can be set on the same parameter s_H by looking for any member of the fiveplet. Searches for the singly and doubly charged member of the fiveplet ($H_5^{\pm}, H_5^{\pm\pm}$) have been conducted at $\sqrt{s} = 13$ TeV with an integrated luminosity of 36 fb^{-1} by the CMS collaboration [88, 89], and the ATLAS collaboration performed a search for the neutral H_5^0 [90]. Some of these results will be shown in section 5.9.1 for comparisons with the present analysis.

5.2 Data and Monte Carlo samples

5.2.1 Dataset

The data used in this analysis were collected during 2015 and 2016 with the ATLAS detector in pp collisions at a centre-of-mass energy of 13 TeV at the Large Hadron Collider (LHC) corresponding to a combined luminosity of 36.1 fb^{-1}. The minimum bunch crossing interval for this run period is 25 ns with a mean number of 23 additional interactions per bunch crossing. The events are required to pass a combination of single-electron or single-muon triggers.

5.2.2 Monte Carlo samples

Monte Carlo (MC) events are simulated using the GEANT4 [91] toolkit within the ATLAS software framework. GEANT4 is a toolkit to simulate the passage of particles through matter. The GEANT4 toolkit and the detailed description of the ATLAS geometry allow accurate simulation from the eV to TeV energy range. However, this comes at a high CPU time requirement up to several minutes per event. Up to 90% of the time is spent to simulate particles in the calorimeter system. In order to reduce the computational requirements and still provide accurate simulations, the FastCaloSim [92] package was developed. To save time a few simplifications were implemented in the simulation mode, for example, it parametrises the development of particle showers and limits the types of particles that are parametrised. FastCaloSim was extensively validated by the ATLAS collaboration and it was also checked that there were no significant deviations compared to fully simulated samples for the WZ analysis. Some of the samples were therefore obtained with the FastCaloSim package. Details of the used signal and background samples can be found in Appendix I.

Additional simulated inelastic pp collisions were overlaid in order to model both the in- and out-of-time effects from additional pp collisions (pile-up) in the same and neighbouring bunch crossings. The mean number of pile-up events in the MC samples was set to reflect the conditions in the data. In figure 4.4 we can see the mean number of interactions per crossing for the 2015 and 2016 run period. The 2016 run period had

a significantly higher mean number of interactions per crossing compared to 2015, 24.9 for 2016 compared to 13.7 for 2015.

The dominant WZ QCD-induced SM background process was modelled using SHERPA 2.2.2 [93]. SHERPA is a MC event generator allowing the simulation of Standard Model and various BSM processes. It can also take care of parton emission off the initial and final state as well as the fragmentation of partons into primary hadrons. The events were generated at Next-to-leading order (NLO). Up to three additional partons generated at tree level were merged with the parton shower. In order to estimate an uncertainty due to the parton shower modelling, two alternative WZ samples were produced using two MC generators similar to Sherpa : Powheg-Box v2 [94] interfaced with Pythia 8.186 for hadronisation and Herwig++ [95] respectively. The Powheg-Box provides an interface between NLO calculations and parton shower generators.

A sample of the purely electroweak process $WZjj \rightarrow \ell\nu\ \ell\ell\ jj$ (labelled $WZjj$), see figure 5.1a, with a matrix-element b-quark veto (at zero order in α_s) was generated separately with Sherpa 2.2.2. Contributions from $WZjb \rightarrow \ell\nu\ \ell\ell\ bj$ (labelled $WZbj$) are included in the tZj sample, see also figure 5.3. To estimate an uncertainty due to the parton shower modelling an alternative MadGraph+Pythia 8 sample was produced. This MadGraph sample includes b-quarks in the initial state and was split to provide a sample without (with) a b-quark in the final state to model the $WZjj$ ($tZ + WZbj$) background.

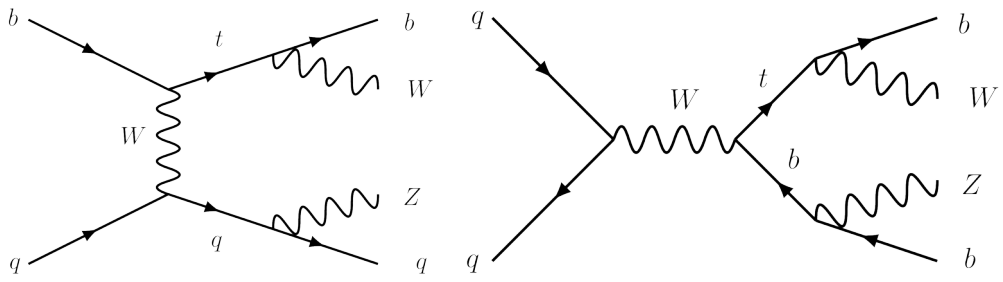

Figure 5.3: Feynman diagram depicting the tZ production with (left) and without (right) a b-quark in the initial state. The WZ-bosons decay to three leptons.

Processes of $q\bar{q} \rightarrow ZZ \rightarrow 4\ell$ or $q\bar{q} \rightarrow ZZ \rightarrow \ell\ell\ \nu\nu$ can be backgrounds if any of the

$ZZ \to 4\ell$ leptons is mis-identified or if an additional non-prompt lepton is measured in the $ZZ \to \ell\ell\,\nu\nu$ process in order to pass the three lepton preselection described below. Both samples were generated by Powheg-Box v2 at NLO, interfaced to Pythia 8.186 [96] and normalised to Next-to-next-to-leading order (NNLO) by K-factors evaluated in Ref. [97]. The $gg \to ZZ$ and tribosons were generated with Sherpa 2.1.1. The $t\bar{t}V$ and tZ processes were generated at leading order (LO) using MadGraph5_aMC@NLO, interfaced with Pythia 8.186 ($t\bar{t}V$) and Pythia 6.428 (tZ). The $t\bar{t}V$ samples were normalised to NLO predictions [98].

Finally, samples of SM backgrounds with at least one misidentified or non-prompt lepton, including $Z\gamma$, $W\gamma$, Drell–Yan $Z \to \ell\ell$, $W \to \ell\nu$ as well as top-pair and single-top, were generated to assist in the fake/non-prompt lepton background estimate. Events with $Z\gamma$ and $W\gamma$ in the final state were generated with Sherpa 2.1.1. Drell–Yan $Z \to \ell\ell, W \to \ell\nu$ as well as top-pair and single-top production channels were generated with Powheg-Box v2 and hadronised with Pythia8. To avoid double-counting the $Z\gamma$ events, Z events produced by the Drell–Yan process with a photon from final-state radiation with $p_{\mathrm{T}} > 10$ GeV were removed. The parton shower for processes with top quarks was modelled with Pythia 6.428. MadGraph5_aMC@NLO and Pythia 8.186 were used for background processes involving a pair of top quarks accompanied by a W boson or by a pair of charged leptons. The Z and single-top cross sections were normalised to NNLO by K-factors evaluated in Ref. [97, 99].

5.2.3 Signal samples

For the HVT interpretation in the $q\bar{q}$ channel, $W' \to WZ$ samples were generated. Two benchmark models are used, Model A and B as described in section 3.3.3.1 and 3.3.3.2. The parameter g_V was set to 1 for Model A and to 3 for Model B. For both models, the parameter c_F is assumed to be the same for all types of fermions. Simulated signal samples for the HVT benchmark Model A were generated for masses of vector resonances ranging from 250 GeV to 3 TeV with MadGraph5_aMC@NLO 2.2.2 with the NNPDF23LO probability density function (PDF) set. They were hadronised with Pythia 8.186. For the interpretation in terms of model B, the Model A cross sections

for masses above 800 GeV were simply scaled since the width of the resonances are well below experimental resolution and the angular distributions are identical for both models. Below 800 GeV, Model B violates theoretical constraints of the HVT parametrization.

For the VBF production channels signal samples were produced for both benchmark models. The HVT samples were generated with $g_V = 1$ for masses ranging from 250 to 2 TeV. The coupling parameter c_H was set to 1 whereas all other couplings of the heavy triplet, including c_F, were set to 0. The triplet therefore couples nearly exclusively to vector bosons. In order to reduce non-Vector Boson Scattering (VBS) diagrams, where the final quarks are produced by W or Z boson decays instead of coming from the initial quarks of the protons (see one example of a Feynman diagram in figure 5.4), a dijet invariant mass of at least 150 GeV was required during event generation.

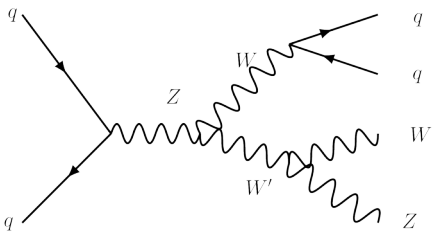

FIGURE 5.4: Example of a non-VBS production of WZ with two jets in the HVT model.

The GM $H_5^{\pm}$ samples (see section 3.4) were produced with MADGRAPH5_aMC@NLO 2.2.2 for the mass range between 200 and 900 GeV with model parameters defined by the H5plane (see section 3.4.2) and with $\sin\theta_H = 0.5$. To satisfy theoretical constraints, see section 3.4.1, the tool GMCALC [100] is used. GMCALC is a program that, given a set of input parameters, calculates the particle spectrum and tree-level couplings while checking if they satisfy theoretical model constraints. It generates param_card.dat files necessary for the MADGRAPH generation of signal samples. The samples were produced at leading order, but normalised to NLO according to Ref [101]. For these samples, a minimum p_{T} of 15 GeV (10 GeV) for jets (leptons) was required during event generation. In addition the pseudorapidity was required to be in the range $|\eta| < 5$ for jets and $|\eta| < 2.7$ for leptons.

5.3 Object selection

Events are required to have at least one primary vertex with at least two associated tracks, each with transverse momentum $p_{\mathrm{T}} > 0.4$ GeV. If there is more than one vertex reconstructed in the event, the one with the largest track $\sum p_{\mathrm{T}}^2$ is chosen as the hard-scatter primary vertex and is subsequently used for the reconstruction of electrons, muons, jets and missing transverse momentum.

The electron candidates are required to satisfy the *Medium* or the *Tight* reconstruction quality requirements, as defined in section 4.2.7.1. Only electrons with transverse energy $E_{\mathrm{T}} > 25$ GeV in the pseudorapidity range $|\eta| < 2.47$ are considered in this analysis.

The candidate electrons are required to pass the track isolation requirements outlined in section 4.2.7.1. The 99% operating point is used in this analysis. For *Tight* electrons, an isolation requirement is imposed, based on calorimeter as well as track variables, which varies as a function of transverse energy and yields an efficiency between 95% and 99% for electrons with p_{T} in the range 25–60 GeV. For a pair of electrons sharing the same ID-track, the electron with the highest cluster E_{T} is kept.

The muons are required to satisfy either *Medium* or *Tight* quality requirements, as defined in section 4.2.7.2. Only muons with $p_{\mathrm{T}} > 25$ GeV and $|\eta| < 2.7$ are considered in this analysis. Isolation requirements are also applied to all muons, based on the track isolation variable defined in section 4.2.7.2.

Electron and muon candidates are required to originate from the primary vertex. Thus, the significance of the track's transverse impact parameter calculated relative to the beam line, $|d_0/\sigma_{d_0}|$, must be less than three for muons and less than five for electrons, and the longitudinal impact parameter, z_0 (the difference between the value of z of the point on the track at which d_0 is defined and the longitudinal position of the primary vertex), is required to satisfy $|z_0 \cdot \sin(\theta)| < 0.5$ mm.

As outlined in section 4.2.7.3, jets are reconstructed using the anti-k_{T} algorithm. In this analysis a radius parameter $R = 0.4$ was chosen. Events with jets arising from detector noise or other non-collision sources are discarded [102]. This search considers jets with $p_{\mathrm{T}} > 30$ GeV in the range $|\eta| < 4.5$. Furthermore, to mitigate the pile-up

contamination, a jet vertex tagger [103], based on information about tracks associated with the primary vertex and pile-up vertices, is applied to jets with $p_{\mathrm{T}} < 60$ GeV and $|\eta| < 2.4$. The selected working point provides at least 92% efficiency. The energy of each jet is calibrated and corrected for detector effects using a combination of simulated events and in situ methods in 13 TeV data [104].

As lepton and jet candidates can be reconstructed from the same detector information, a procedure to resolve overlap ambiguities is applied. If an electron and a muon share the same ID track, the muon is selected. Reconstructed jets which overlap with electrons or muons in a cone of size $\Delta R = 0.2$ are removed.

Jets containing B hadrons are identified as *b-jets* by the MV2c10 b-tagging algorithm [105][106]. MV2 is a multivariate algorithm using Boosted Decision Tree (BDT), which will be presented in greater detail in section 6.1. The input variables of the MV2 BDT algorithm all exploit the relatively long B hadrons lifetime and high mass. The output of three basic algorithms are used as inputs, a likelihood-based combination of the transverse and longitudinal impact parameter significances, the presence of a secondary vertex and the reconstruction of the B hadrons decay chain using a Kalman filter to search for a common direction connecting the primary vertex to the bottom and charm decay vertices. A working point corresponding to 85% b-tagging efficiency on a sample of $t\bar{t}$ events is chosen [107], with a light-flavour jet rejection factor of about 34 and a c-jet rejection of about 3. Correction factors are applied to the simulated event samples to compensate for differences between data and simulation in the b-tagging efficiency for b-jets, c-jets and light-flavour jets.

5.4 Event selection

As a preselection, three prompt charged leptons (e or μ) are required of which two will be associated with the Z and one with the W boson. The Z boson candidate requires two leptons satisfying the *Medium* quality requirements described in section 5.3 of same flavour and of opposite charge and with an invariant mass m_{ll} close to the on-shell mass, m_Z, $|m_{ll} - m_Z| < 20$ GeV. The third lepton, associated with the W boson decay, is required

to satisfy the *Tight* quality requirement to enhance background rejection. To ensure a well-determined trigger efficiency at least one lepton is required to have $p_{\mathrm{T}} > 27$ GeV.

In order to suppress the background with at least four prompt leptons, as, for example, in ZZ production, events with a fourth lepton candidate satisfying looser selection criteria are rejected. The requirement of the minimum p_{T} of the leptons is lowered to $p_{\mathrm{T}} > 7$ GeV and *Medium* identification requirements are used for both the electrons and muons.

Control distributions, with the above preselection conditions applied, for the reconstructed Z and W bosons are presented in figure 5.5. The expected background and normalisation, including the *fake/non-prompt* background (see section 5.6.1), are directly obtained from the MC simulation. The WZ transverse mass (m_{T}^{WZ}) is obtained by taking the four-vectors of the final state leptons associated to the W and Z, and by projecting them on the transverse plane neglecting their longitudinal component ($\boldsymbol{p}_l = (p_{\mathrm{T}} \cos\phi_l, p_{\mathrm{T}} \sin\phi_l, 0)$). The transverse mass m_{T}^{WZ} is then defined as the invariant mass of the projected four-vectors of the three leptons combined with the $E_{\mathrm{T}}^{\mathrm{miss}}$. In general, a fair agreement is observed in the shapes of the distributions between data and simulations.

5.4.1 Invariant mass reconstruction

The WZ invariant mass is the final discriminant variable in this analysis. However, due to the presence of the neutrino in the final state only the transverse momentum of the W can be accurately measured by the detector. Due to the unknown momentum transfer between the hard scattering partons, the missing energy along the beam line is not measurable. The $E_{\mathrm{T}}^{\mathrm{miss}}$ is assumed to be the neutrino transverse momentum p_{T}^{ν}. The longitudinal component of the neutrino's momentum p_z^{ν} can be obtained by solving a quadratic equation and using the measured mass of the W boson m_W :

$$m_W = \sqrt{(p_\nu + p_\ell)^2} = 80.4 \text{ GeV} . \tag{5.1}$$

In this equation the neutrino and lepton mass can be neglected, so $p_\nu^2 = m_\nu^2 \approx 0$ and $p_\ell^2 = m_\ell^2 \approx 0$, and equation 5.1 simplifies too :

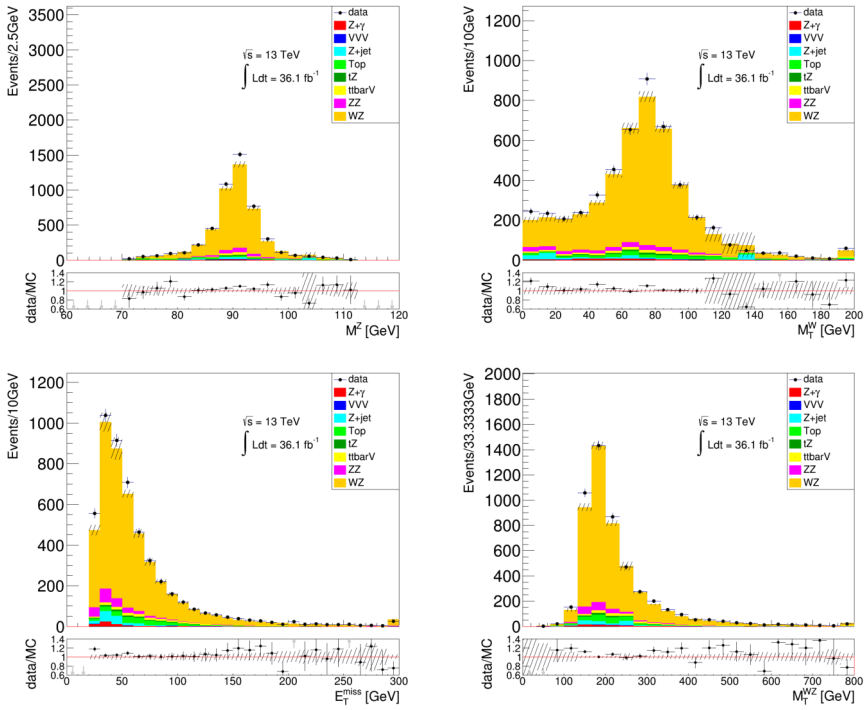

FIGURE 5.5: Control distributions for the sum of all channels, the Z boson invariant mass is shown on the top left, the W boson transverse mass on the top right, the $E_{\mathrm{T}}^{\mathrm{miss}}$ on the bottom left and the transverse mass of the WZ system on the bottom right. All MC expectations are scaled to the integrated luminosity of the data using the predicted MC cross sections of each sample.

$$m_W^2 \approx 2p_\nu p_\ell \Leftrightarrow \frac{m_W^2}{2} = E_\nu E_\ell - \boldsymbol{p}_\nu \cdot \boldsymbol{p}_\ell \,, \tag{5.2}$$

where $E_\nu = \sqrt{\left(p_{\mathrm{T}}^\nu\right)^2 + \left(p_z^\nu\right)^2}$ and $\boldsymbol{p}_\nu \cdot \boldsymbol{p}_\ell = p_{\mathrm{T}}^\nu p_{\mathrm{T}}^\ell \cos(\phi^\nu - \phi^\ell) + p_z^\nu p_z^\ell$.

With these definitions equation 5.2 can be written as :

$$\left(p_z^\nu\right)^2 \cdot (E_\ell^2 - (p_z^\ell)^2) - 2Ap_z^\nu \cdot p_z^\ell + \left(p_{\mathrm{T}}^\nu\right)^2 E_\ell^2 - A^2 = 0 \,, \tag{5.3}$$

where A is defined as $A = \frac{m_W^2}{2} + p_{\mathrm{T}}^\nu p_{\mathrm{T}}^\ell \cos(\phi^\nu - \phi^\ell)$.

Solving this quadratic equation for p_z^ν yields two solutions

$$p_z^\nu = \frac{Ap_z^\ell \pm E_\ell \sqrt{A^2 + (p_{\mathrm{T}}^\nu)^2((p_z^\ell)^2 - E_\ell^2)}}{E_\ell^2 - (p_z^\ell)^2} \tag{5.4}$$

There are two either real or complex solutions. As it is a priori arbitrary which solution is best, it has been studied which solution is closest to the truth invariant mass [12]. Figure 5.6 shows the WZ truth mass distribution and is compared to the reconstructed mass. On the left, the two real solutions for p_z^ν in equation 5.4 are shown along with the truth mass. The plot on the right compares the truth and reconstructed mass if the solutions are complex, here only the real part of the solution for p_z^ν is kept for the reconstructed mass. The difference between the reconstructed and truth mass is shown in figure 5.7 where it can be observed that the smaller solution provides a better agreement with the truth mass. Therefore for real solutions, the smaller one is chosen and for complex solutions, the real part is kept in this analysis.

5.5 Signal region optimisation

This search has two distinct search regions in order to discriminate between the $q\bar{q}$ and VBF production mode. The VBF production mode is characterised by two high-energetic jets in the forward regions of the detector. Therefore two or more jets are required in this category, which have significant η separation and a large di-jet invariant mass.

The two regions are set up as exclusive categories, meaning first, events are checked

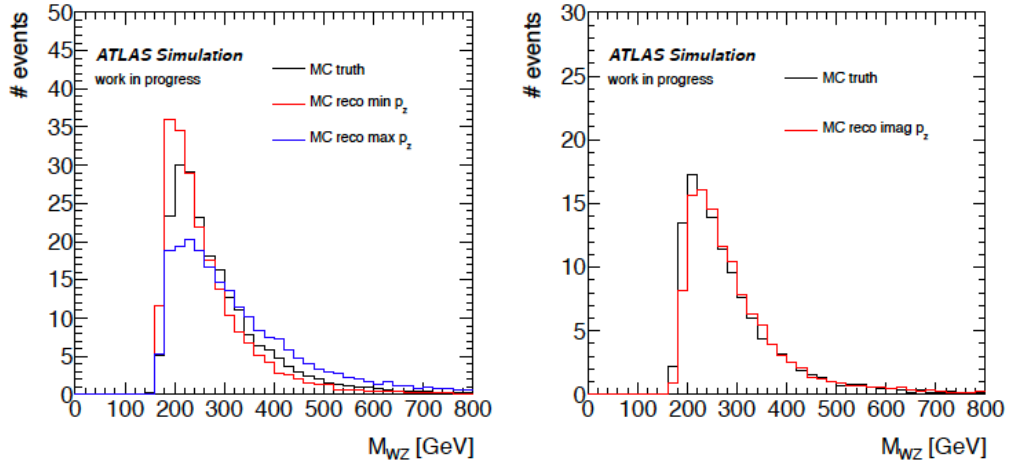

FIGURE 5.6: The plot on the left shows the reconstructed and truth WZ mass distribution obtained with MC. In black the truth WZ mass is shown, the red and blue curves show the reconstructed WZ mass when the minimum or maximum real solution of equation 5.4 are used. The plot on the right shows the truth and reconstructed WZ mass for complex solutions, in this case only the real part of the p_z^ν solution is kept. [12]

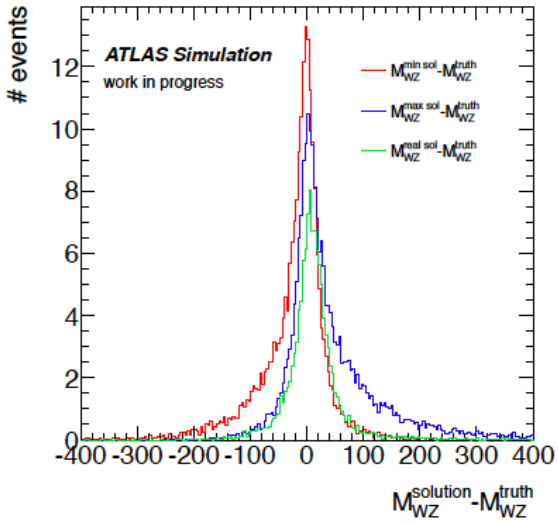

FIGURE 5.7: Difference between the reconstructed solutions and the truth WZ mass. Red and blue show the reconstructed WZ mass using the smallest and highest p_z^ν of equation 5.4 respectively, the green line shows the cases when an imaginary solution is found and the real part is kept. [12]

if they fall into the VBF-category, and only if the selection fails, they are checked if they fall into the $q\bar{q}$-category. The $q\bar{q}$-enriched category selection exploits the fact that for W and Z resonant production, a substantial fraction of the resonant mass is converted to kinetic energy of the bosons. The transverse momentum of the W and Z boson, $p_{\mathrm{T}}^{W/Z}$, therefore provides a clear separation between the signal and the WZ SM background.

5.5.1 The VBF signal region

In addition to the basic event selection described in section 5.4, at least two jets with p_{T} greater than 30 GeV and $|\eta| < 4.5$ are required for the VBS analysis. Two variables are used to isolate VBF contribution, the di-jet mass m_{jj} and eta separation $|\Delta\eta_{jj}|$ of the two p_{T} -leading jets since the VBS topology predicts larger values for these variables than the main WZ QCD background. Figure 5.8 shows the shape of the distribution of m_{jj} and $|\Delta\eta_{jj}|$ for some of the GM signal points and the SM QCD background. A cut on these variables is used to separate between the signal and validation regions.

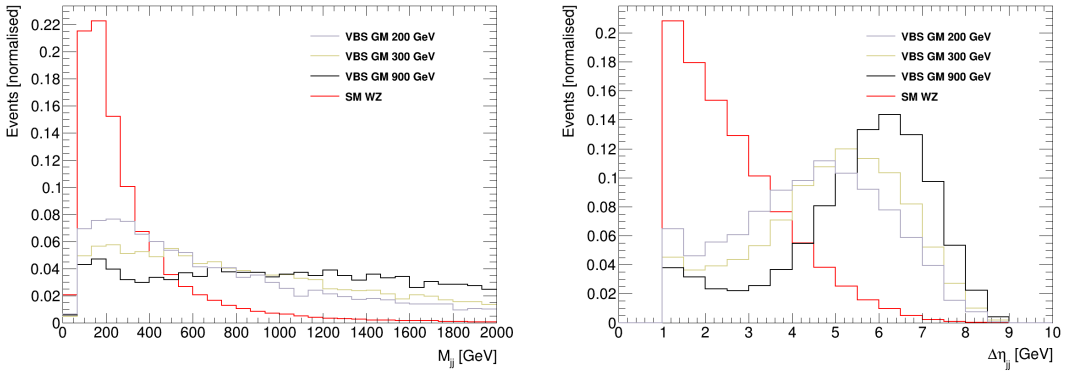

FIGURE 5.8: Distributions of m_{jj} (left) and $|\Delta\eta_{jj}|$ (right) for some of the GM VBF signal mass points and the SM backgrounds.

In order to find the optimal value for these cuts, a numerical optimisation process was used. A two-dimensional space of potential cut values was created and the point with the highest binned Poisson significance Z was chosen, defined as

$$Z = \sqrt{\sum_i 2\left((S_i + B_i)\log\left(1 + \frac{S_i}{B_i}\right) - S_i\right)}. \tag{5.5}$$

Here S_i and B_i are respectively the amounts of signal and background events in bin i of the reconstructed mass histogram. A bin size of 50 GeV was chosen for this histogram. The optimisation was performed in a $\pm 2\sigma$ mass window around the resonance mass. The significance Z was obtained from a Gaussian fit to the mass peak. The optimal values found where $m_{jj} > 500$ Gev and $|\Delta\eta_{jj}| > 3.5$. In figure 5.9 we can see as an illustration the calculated significance for different cut values for the 200 GeV GM and the 250 GeV HVT mass point. The coloured z-axis corresponds to the expected significance obtained with equation 5.5.

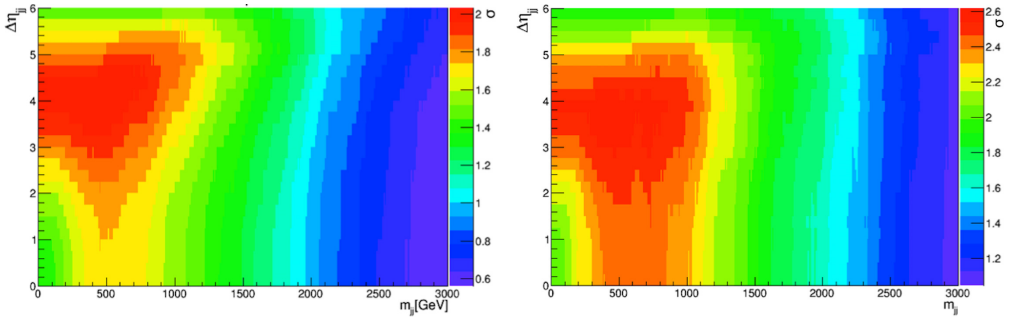

FIGURE 5.9: 2D scan of the variables m_{jj} and $|\Delta\eta_{jj}|$ for the 200 GeV GM mass point (left) and the 250 GeV HVT mass point(right), the colour corresponds to the expected signal significance Z as defined in equation 5.5.

For further rejection of backgrounds with top quarks, a b-jet veto is applied jets with p_T >20 GeV and $|\eta_{\text{jet}}| < 2.5$ [106]. Out of the possible working points corresponding to different b-tagging efficiencies, the 85% working point is selected as the baseline.

The acceptance times efficiency $\mathcal{A} \times \epsilon$ of the full selection as a function of the mass of the VBS $H_5^{\pm}$ and HVT resonance is shown in figure 5.10. For the GM signal samples, only the Z decays to e^+e^- and $\mu^+\mu^-$ were simulated since $Z \to \tau^+\tau^-$ decays give negligible contributions, but the $\mathcal{A} \times \epsilon$ shown was scaled to include all decays. As expected from figure 5.8, the acceptance times efficiency is higher for larger resonance masses, as fewer events are excluded by the VBF-selection cuts. Other important sources

of selection inefficiencies are due to non-leptonic tau decays. For HVT and $H_5^{\pm}$ the $\mathcal{A} \times \epsilon$ falls in the range of 2-8% and 3-12% respectively for resonance masses ranging between 200 and 900 GeV, the difference being due in part to the generator level selection, see section 5.2.3, and in part to different angular distributions of the final state particles.

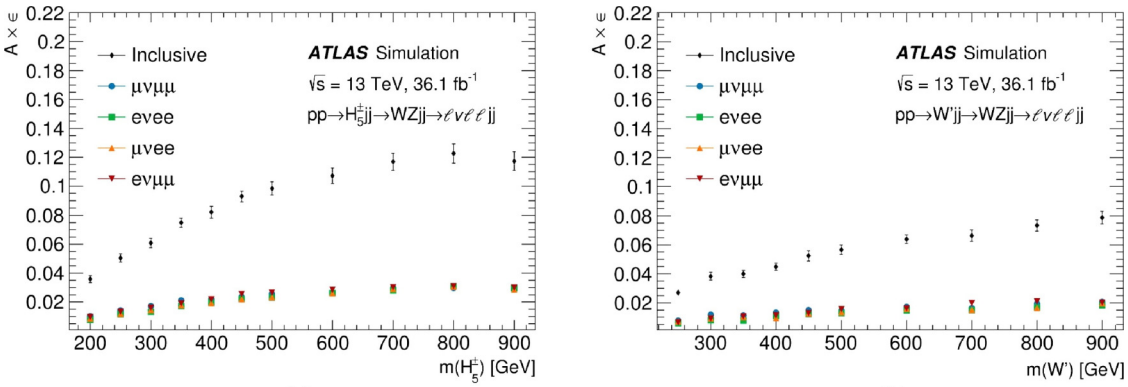

FIGURE 5.10: The signal selection acceptance times efficiency (A×ϵ), defined as the ratio of the number of MC signal events in the VBF category to the number of generated signal events, as a function of the $H_5^{\pm}$ (a) and HVT (b) resonance mass. The error bars represent the total statistical and systematic uncertainties.

5.5.2 The $q\bar{q}$ signal region

The variable $p_{\mathrm{T}}^{W/Z}$ is strongly dependent on the resonance mass. Therefore the mass-dependent cuts $p_{\mathrm{T}}^{W}/m_{WZ}$ and $p_{\mathrm{T}}^{Z}/m_{WZ}$ are used in this analysis. Figure 5.11 shows the distribution of $p_{\mathrm{T}}^{W}/m_{WZ}$ and $p_{\mathrm{T}}^{Z}/m_{WZ}$ and the SM WZ background for various resonance masses. As can be seen in this figure, an optimal cut would be similar for all masses, therefore a common cut on these quantities can be used for all mass points.

In order to optimise the cuts on the $p_{\mathrm{T}}^{W}/m_{WZ}$ and $p_{\mathrm{T}}^{Z}/m_{WZ}$ variables, the expected limits are calculated using only the SM WZ background and no systematics. A scan of different values of $p_{\mathrm{T}}^{W}/m_{WZ}$ and $p_{\mathrm{T}}^{Z}/m_{WZ}$ was performed comparing it also to the variables used in the ATLAS 8 TeV analysis [76]. In the 8 TeV analysis, the following variables exploiting the boosted W and Z boson topology were chosen : $\Delta y(W,Z)$, the rapidity separation between the W and Z boson, and $\Delta\phi(\ell^W, E_{\mathrm{T}}^{\mathrm{miss}})$, the angular separation

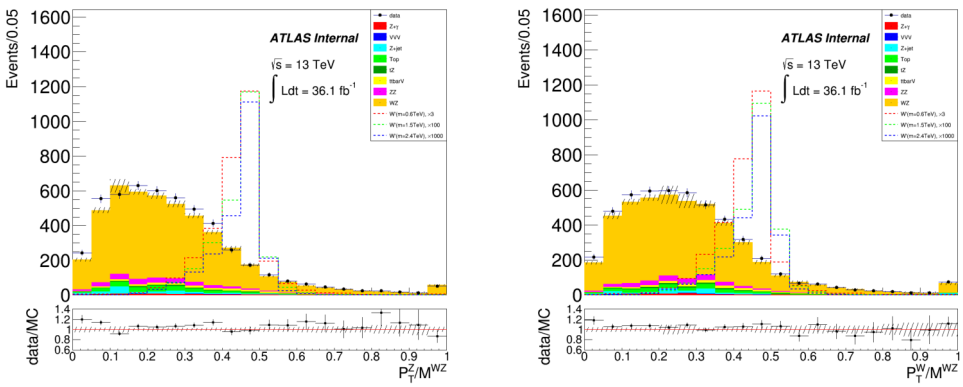

FIGURE 5.11: Distributions of $p_{\mathrm{T}}^{Z}/m_{\mathrm{WZ}}$ (left) and $p_{\mathrm{T}}^{W}/m_{\mathrm{WZ}}$ (right) for the HVT signal mass points and the backgrounds.

between the lepton from the W decay and the transverse missing energy vector. Figure 5.12 shows the expected limits for different cut values on $p_{\mathrm{T}}^{W}/m_{WZ}$ and $p_{\mathrm{T}}^{Z}/m_{WZ}$, the 8 TeV analysis cuts ($\Delta y(W,Z) < 1.5$ and $\Delta\phi(\ell^{W},E_{\mathrm{T}}^{\mathrm{miss}}) < 1.5$) in the HVT resonance mass range between 500 and 3000 GeV. For masses below 2 TeV, a cut of 0.35 on the variables $p_{\mathrm{T}}^{W}/m_{WZ}$ and $p_{\mathrm{T}}^{Z}/m_{WZ}$ yields the best results, whereas for higher masses a cut value of 0.25 is preferred. Since this analysis has the best sensitivity at low masses compared to other W and Z decays, a cut value of 0.35 was chosen for all mass points. A combination of this cut value with the 8 TeV cuts, here referred to as "All cuts", did not show any improvement.

The acceptance times efficiency $\mathcal{A} \times \epsilon$ relative to generated events increases from about 15% to 25% for resonance masses ranging from 500 GeV to 3 TeV as illustrated in Figure 5.13. For resonance masses above 2 TeV the bosons W and Z are highly boosted. This leads to a decrease in the $\mathcal{A} \times \epsilon$, especially in the electron channels. As the electrons from the $Z \rightarrow ee$ decays are too boosted to be resolved as two individual electrons due to the limited spatial resolution of the ATLAS calorimeter. This, in turn, spoils the isolation requirements. The effect is smaller for muons, as the ATLAS muon detector provide much better spatial resolution. However, the mass resolution degrades significantly at high p_{T}. For the current data set, the sensitivity decreases rapidly for high mass resonances, and therefore no steps were taken to solve this issue by changing the isolation requirements.

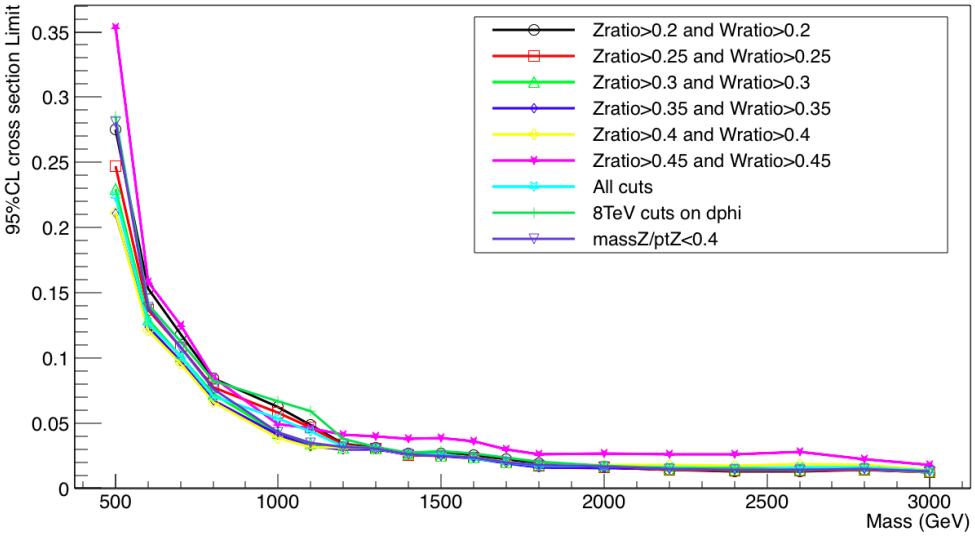

FIGURE 5.12: Expected limits in arbitrary units as a function of HVT invariant mass for different cuts on $p_{\mathrm{T}}^{\mathrm{Z}}/m_{\mathrm{WZ}}$ and $p_{\mathrm{T}}^{W}/m_{\mathrm{WZ}}$ and for 8 TeV analysis cut in the mass range between 500 and 3000 GeV.

This problem will be addressed in the full run-2 analysis, see Chapter 6.

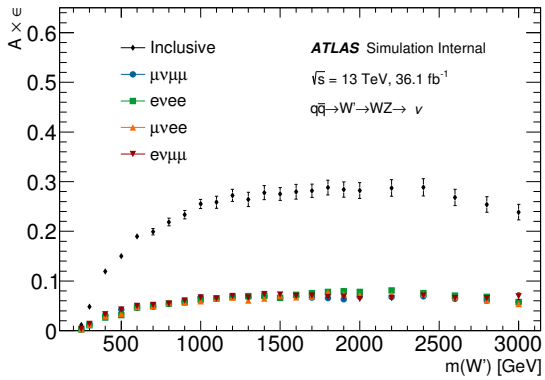

FIGURE 5.13: The signal selection acceptance times efficiency (A×ϵ), defined as the ratio of the number of MC signal events in the $q\bar{q}$ category to the number of generated signal events, as a function of the HVT resonance mass. The error bars represent the total statistical and systematic uncertainties.

5.6 Background estimation

The dominant background in the resonance search is SM production of WZ. Its normalisation and shape are estimated from MC and validated in dedicated validation regions by comparing the data and MC distributions. One validation region is constructed for each Signal Region (SR). These validation regions use the same selection as the SR but the selection criteria as defined in section 5.5 are inverted to make them orthogonal to the SR. The VBF WZ validation region is defined by inverting the requirements on the dijet variables : $100 < m_{jj} < 500$ GeV and $\Delta\eta_{jj} < 3.5$. The minimal cut on the m_{jj} variable excludes the low end of the distribution which is difficult to model. The WZ $q\bar{q}$ validation region requires the events to have $p_{\mathrm{T}}^{Z}/m_{\mathrm{WZ}} < 0.35$ and $p_{\mathrm{T}}^{W}/m_{\mathrm{WZ}} < 0.35$. These validation regions are dominated by the WZ contribution, with a purity higher than 80%. For the benchmark models, as described in section 5.2.3, the signal contamination in the $q\bar{q}$ (VBF) validation region is below 5% (1%). The reconstructed m_{WZ} mass in the validation regions is shown in figure 5.14.

Events from Z+jets, $Z\gamma$, $W\gamma$, $t\bar{t}$, single top or WW where jets or photons are misidentified as leptons (here called *fake/non-prompt* leptons), can also satisfy the selection criteria. Since the simulation of these background events is especially difficult, a data-driven method using a global matrix is used to estimate this contribution. Details of the method, here referred to as "Matrix Method", will be given in the next subsection.

Other minor backgrounds include $t\bar{t}V, ZZ, tZ, WZbj$ and triple boson production. They are estimated by MC simulation. The $tZ, WZbj$ and VVV backgrounds are added as a single contribution, here called $tZ + VVV$.

5.6.1 *Fake/non-prompt* background estimation using a global Matrix Method

The matrix method exploits differences in object characteristics between real and fake leptons on a statistical basis. Real and fake lepton categories are defined as :

— Real leptons (R) : are prompt leptons originating from the W or Z boson decays

— Fake leptons (F) : leptons produced in jets, hadrons misidentified as leptons or photon conversions.

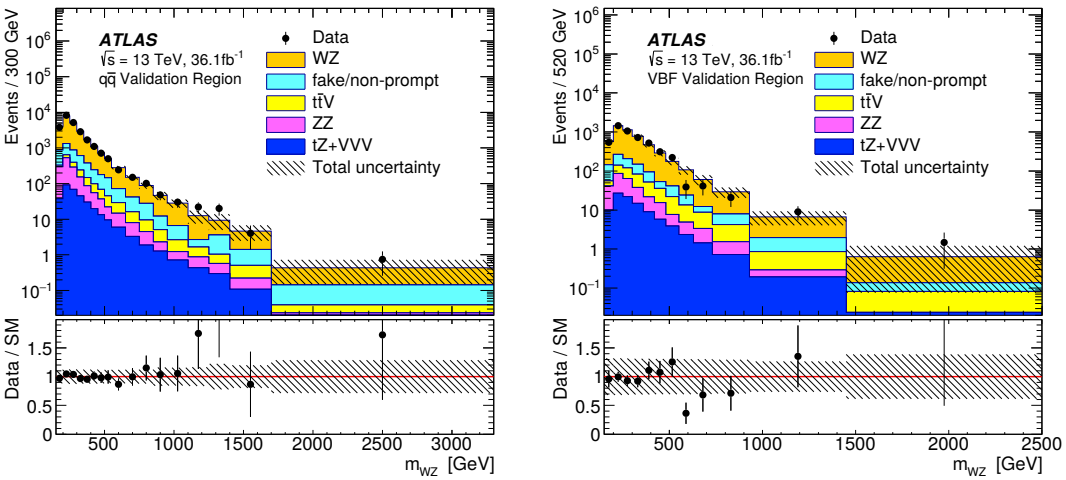

(a) (b)

FIGURE 5.14: Observed and expected distributions of the WZ invariant mass in (a) the $q\bar{q}$ validation region and (b) the VBF validation region. The points correspond to the data and the histograms to the expectations for the different SM processes. The uncertainty in the total background prediction, shown as bands, combines statistical, theory and systematic contributions. The last bin contains the overflow.

The following lepton ordering of the three leptons in the WZ final state (i, j, k) will be used : the lepton from the W decay, followed by the p_{T} -leading and p_{T} -trailing lepton of the Z decay. The final selection contains a mixture of real and fake leptons, with the following contributions :

— N_{RRR} : events with three real prompt leptons. Here the signal events and background processes with 3 prompt leptons coming from WZ, ZZ and $t + Vj$ are contributing.

— N_{FRR} : events with one fake lepton associated to the W decay and two prompt leptons associated with the Z boson. Here the main contribution are from Z+jets, $Z + \gamma$ and $t\bar{t}$ backgrounds.

— N_{RRF} and N_{RFR} : events where one fake lepton entering the Z selection. The main contributions come from the backgrounds Z+jets and $Z + \gamma$ where one of the two Z lepton is mis-paired with a fake lepton from the Z, and some contribution from the $t\bar{t}$ background.

— $N_{FFR}, N_{FRF}, N_{RFF}, N_{FFF}$: events with at least two fake leptons passing the selection criteria. Here W+jets, Z+jets, $t\bar{t}$ backgrounds are contributing. The number of events with two fakes is an order of magnitude smaller than the number of events with one fake and the number of events with three fake leptons can be neglected.

These categories are difficult to estimate directly from MC simulations, as small differences in the detailed implementation of the detector in the simulation result in big discrepancies in the predicted number of fake leptons versus the measured number. The general idea of the global Matrix Method is to estimate the number of events in each of these categories by measuring the number of events in categories that are easier to simulate than the contribution of fake leptons. Therefore leptons are classified as "loose" (L) or "tight" (T) according to the isolation and/or reconstruction quality. In this analysis, loose leptons are baseline leptons passing overlap removal but failing isolation while tight leptons are signal leptons as defined in section 5.4. Electrons may also fail the tightness requirement (Tight quality for electron coming from the W decay or Medium quality for electrons forming Z), whereas muons must fail only the isolation. The method then

assumes that the contributions from loose and tight leptons can be expressed as a linear combination of the contributions from real and fake leptons. In a three lepton final state, the matrix would be an 8×8 matrix. When neglecting the contribution from three fake leptons N_{FFF} and three loose leptons N_{LLL}, the matrix simplifies to a 7×7 matrix :

$$\begin{pmatrix} N_{TTT} \\ N_{TTL} \\ N_{TLT} \\ N_{LTT} \\ N_{TLL} \\ N_{LTL} \\ N_{LLT} \end{pmatrix} = \begin{pmatrix} e_1e_2e_3 & e_1e_2f_3 & e_1f_2e_3 & f_1e_2e_3 & e_1f_2f_3 & f_1e_2f_3 & f_1f_2e_3 \\ e_1e_2\bar{e}_3 & e_1e_2\bar{f}_3 & e_1f_2\bar{e}_3 & f_1e_2\bar{e}_3 & e_1f_2\bar{f}_3 & f_1e_2\bar{f}_3 & f_1f_2\bar{e}_3 \\ e_1\bar{e}_2e_3 & e_1\bar{e}_2f_3 & e_1\bar{f}_2e_3 & f_1\bar{e}_2e_3 & e_1\bar{f}_2f_3 & f_1\bar{e}_2f_3 & f_1\bar{f}_2e_3 \\ \bar{e}_1e_2e_3 & \bar{e}_1e_2f_3 & \bar{e}_1f_2e_3 & \bar{f}_1e_2e_3 & \bar{e}_1f_2f_3 & \bar{f}_1e_2f_3 & \bar{f}_1f_2e_3 \\ e_1\bar{e}_2\bar{e}_3 & e_1\bar{e}_2\bar{f}_3 & e_1\bar{f}_2\bar{e}_3 & f_1\bar{e}_2\bar{e}_3 & e_1\bar{f}_2\bar{f}_3 & f_1\bar{e}_2\bar{f}_3 & f_1\bar{f}_2\bar{e}_3 \\ \bar{e}_1e_2\bar{e}_3 & \bar{e}_1e_2\bar{f}_3 & \bar{e}_1f_2\bar{e}_3 & \bar{f}_1e_2\bar{e}_3 & \bar{e}_1f_2\bar{f}_3 & \bar{f}_1e_2\bar{f}_3 & \bar{f}_1f_2\bar{e}_3 \\ \bar{e}_1\bar{e}_2e_3 & \bar{e}_1\bar{e}_2f_3 & \bar{e}_1\bar{f}_2e_3 & \bar{f}_1\bar{e}_2e_3 & \bar{e}_1\bar{f}_2f_3 & \bar{f}_1\bar{e}_2f_3 & \bar{f}_1\bar{f}_2e_3 \end{pmatrix} \begin{pmatrix} N_{RRR} \\ N_{RRF} \\ N_{RFR} \\ N_{FRR} \\ N_{RFF} \\ N_{FRF} \\ N_{FFR} \end{pmatrix}. \quad (5.6)$$

Here $e(\bar{e})$ denotes the probability that a real lepton is identified as a tight (loose) lepton, and $f(\bar{f})$ denotes the probability that a fake leptons is mis-identified as a tight (loose) lepton.

Using this matrix and by neglecting terms with more than two f factors (since f is a small quantity), the number events with fake leptons $N_{fake} = N_{TTT} - e_1e_2e_3N_{RRR}$ can be expressed as :

$$\begin{aligned} N_{fake} = {} & [N_{TTL} - e_1e_2\bar{e}_3N_{RRR}]\frac{f_3}{\bar{f}_3} + [N_{TLT} - e_1\bar{e}_2e_3N_{RRR}]\frac{f_2}{\bar{f}_2} + [N_{LTT} - \bar{e}_1e_2e_3N_{RRR}]\frac{f_1}{\bar{f}_1} \\ & - [N_{TLL} - e_1\bar{e}_2\bar{e}_3N_{RRR}]\frac{f_2}{\bar{f}_2}\frac{f_3}{\bar{f}_3} - [N_{LTL} - \bar{e}_1e_2\bar{e}_3N_{RRR}]\frac{f_1}{\bar{f}_1}\frac{f_3}{\bar{f}_3} \\ & - [N_{LLT} - \bar{e}_1\bar{e}_2e_3N_{RRR}]\frac{f_1}{\bar{f}_1}\frac{f_2}{\bar{f}_2} \end{aligned} \quad (5.7)$$

The terms in equation 5.7 $N_{TTL}, N_{TLT}, N_{LTT}, N_{TLL}, N_{LTL}$ are measured with data by applying or inverting the tight requirements explained above, while the contribution from the irreducible backgrounds ($N^{irr}_{ijk} = \bar{e}_1\bar{e}_2\bar{e}_3N_{RRR}$) is estimated from MC simulation. The *fake ratios* ($F_i = \frac{f_i}{\bar{f}_i}$) are measured in data by using dedicated control regions. Since the same selection applies for both Z leptons $F_2 = F_3$. Two fake efficiencies need to be

measured for both the electron and muon, one for the W and one for the Z selection. Two Z+jets control regions are defined for this, requiring events to pass all Z selection requirements plus an additional lepton :

— Control region Z + "fake" e : A W transverse mass cut is applied ($M_{\mathrm{T}}^{W} < 30$ GeV) and a cut on the missing transverse momentum $E_{\mathrm{T}}^{\mathrm{miss}}$<25 GeV to reduce the contribution from sources with three prompt leptons. No isolation or d_0 significance cut is applied but it is required that electrons pass the Loose identification requirement.

— Control region Z + "fake" μ : the d_0 significance cut for the additional muon is inverted (d_0 significance>3.0) and no isolation is required.

The distribution of the invariant mass of opposite charged and same flavour dileptons in the Z+jets control regions is shown in figure 5.15. The fake efficiencies will be calculated using the additional lepton.

The resulting p_{T} distributions of the additional jets faking leptons, measured in the Z+jets control regions, is shown for both the Z and W requirements in Figure 5.16 for muons and in Figure 5.17 for electrons.

To calculate the fake efficiency the contribution from irreducible backgrounds (MC_{irr}) in each control region is subtracted from the total number of observed data. The resulting fake rates are determined in three bins of p_{T} as can be seen Figure 5.18 for muons and in Figure 5.19 for electrons.

5.7 Systematic uncertainties

Systematic uncertainties result from the theoretical modelling of backgrounds and from object and event reconstruction.

5.7.1 Systematic uncertainties on the MC background

The uncertainty of the normalisation of the SHERPA samples of SM WZ background is evaluated by taking into account the variations obtained with different parton density functions (PDFs) sets [108]. PDFs are a crucial input into cross-section calculations at

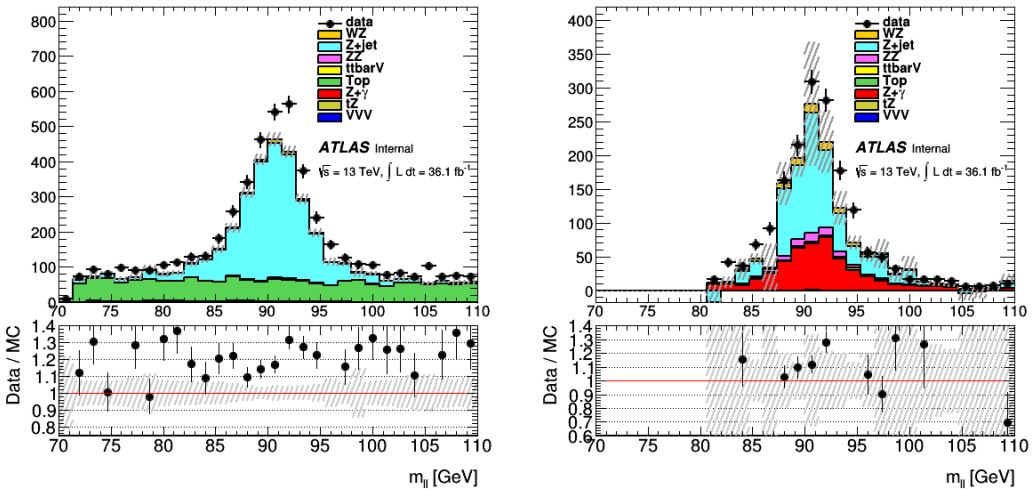

FIGURE 5.15: Invariant mass distribution of opposite charged and same flavour di-leptons in the Z+jets control region. On the left, the "fake" muon control region and on the right the "fake" electron control region. The statistical uncertainty is shown by shaded bands.

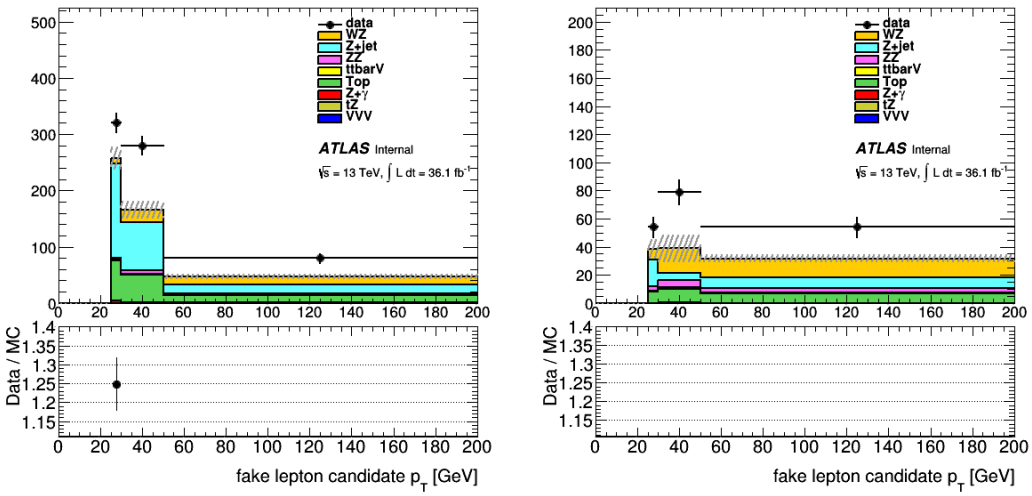

FIGURE 5.16: The transverse momentum distribution of the jet faking muons after applying to the additional lepton the Z (right) and W (left) lepton requirements. The statistical uncertainty is shown by shaded bands.

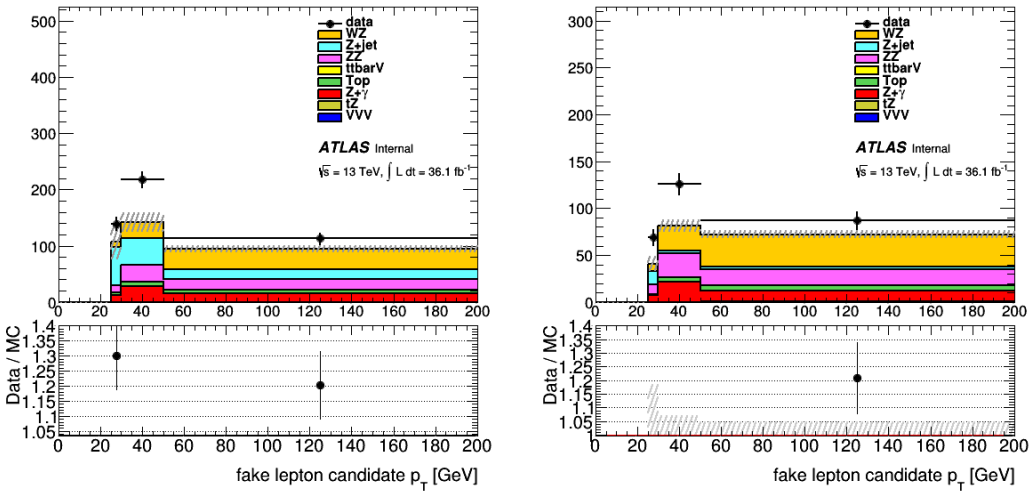

FIGURE 5.17: The transverse momentum distribution of the jet faking electrons after applying to the additional lepton the Z (right) and W (left) lepton requirements. The statistical uncertainty is shown by shaded bands.

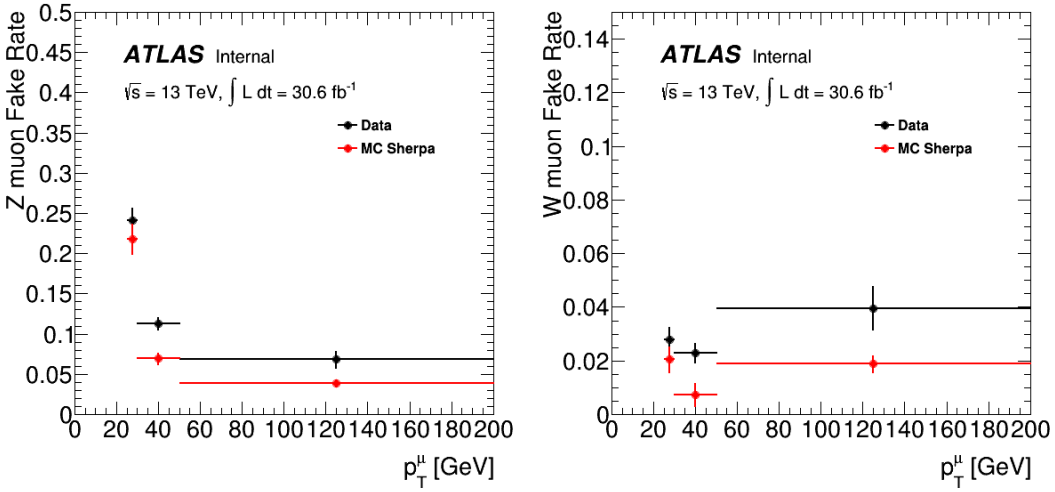

FIGURE 5.18: Distributions of the muon fake rate as a function of p_T in the Z+jets control region, using the Z muon selection on the left. The muon fake rate using the W muon selection is shown on the right.

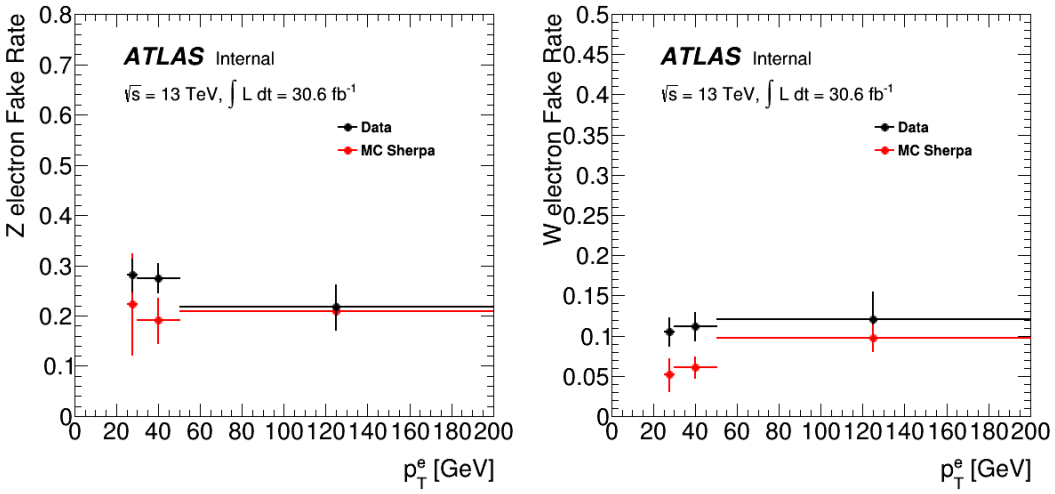

FIGURE 5.19: Distributions of the electron fake rate as a function of p_T in the Z+jets control region, using the Z electron selection on the left. The electron fake rate using the W electron selection is shown on the right.

hadron colliders : they contain the process-independent momentum structure of partons within hadrons. At leading order PDFs give the probability that a beam hadron's momentum is carried by a parton of given flavour and momentum fraction. Since PDFs cannot be directly calculated from first basis given the non-perturbative QCD-regime, they are obtained by a fit on a large number of cross-section data points. The nominal set NNPDF30_nlo_as_0118 is compared with other samples generated with the CT14nnlo and MMHT2014nlo68cl PDF sets and the uncertainty is evaluated from the maximum differences. Figure 5.20 shows the relative uncertainties on the SM WZ background shape due to PDF uncertainties. The resulting uncertainties are below 6% in all mass bins for both the VBF and $q\bar{q}$ categories.

Renormalisation is a treatment of divergences that arises in QCD calculations. The renormalisation scale μ_R is a scale used in the renormalisation of the coupling α_S. In the context of QCD, the scale can be reabsorbed into the counterterms which result in a running strong coupling $\alpha_S(\mu_R)$ also referred to as $\overline{\text{MS}}$ renormalisation scheme. There is a similar scale that arises when regularising the infrared regime, where soft QCD radiation from incoming partons leads to collinear divergences. Here, a scale μ_F is introduced,

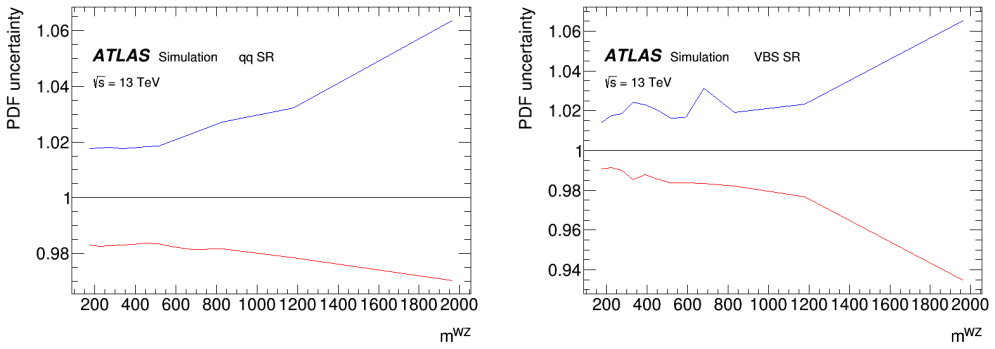

FIGURE 5.20: The relative uncertainties on the SM WZ background shape due to PDF uncertainties as function of the WZ invariant mass in the $q\bar{q}$ fiducial volume left and on the VBF fiducial volume right.

referred to as the factorisation scale. To evaluate the uncertainties associated with the arbitrarily chosen scales, μ_R and μ_F are commonly varied independently by factors of 1/2 and 2. The maximum upwards and downwards deviation with respect to the default choice ($\mu_R = \mu_F = m_{WZ}/2$) is used to estimate the scale uncertainty. The uncertainty as a function of m_{WZ} is shown in figure 5.21 for the $q\bar{q}$ and VBF selection. While these uncertainties can in principle affect the shape of the m_{WZ} distribution, the shape differences do not have a strong impact on the sensitivity of the search in practice. The PDF and scale uncertainties are therefore treated as normalisation uncertainties, taken to be 20% and 40% for the $q\bar{q}$ and VBF category respectively.

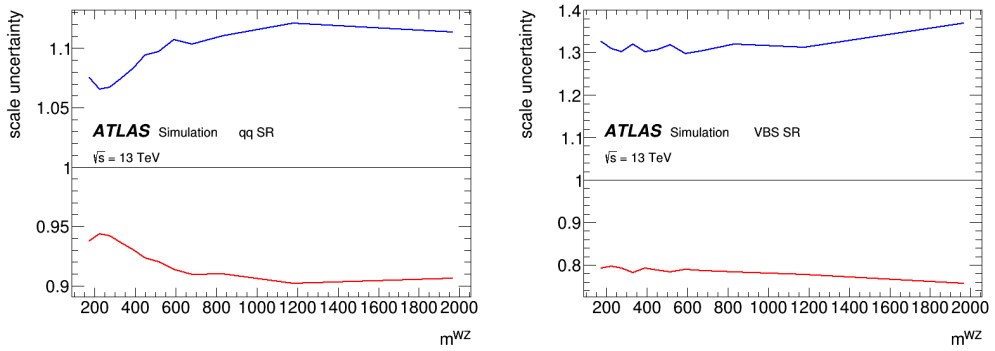

FIGURE 5.21: The uncertainties on on the SM WZ background shape caused by the choice of the scale as function of the WZ invariant mass.

Lastly, to evaluate the uncertainties associated with the parton shower modelling, MC WZ background samples using different parton shower programs, a POWHEG+PYTHIA8 and a POWHEG+HERWIG sample, are used. The per-bin difference between these two samples is added in quadrature to the statistical uncertainty of the POWHEG+HERWIG distribution. The relative uncertainty of this sample is then applied to the default SHERPA 2.2.2 distribution. Figure 5.22 shows the two Powheg samples as well as the default SHERPA with the obtained shower uncertainty band in grey.

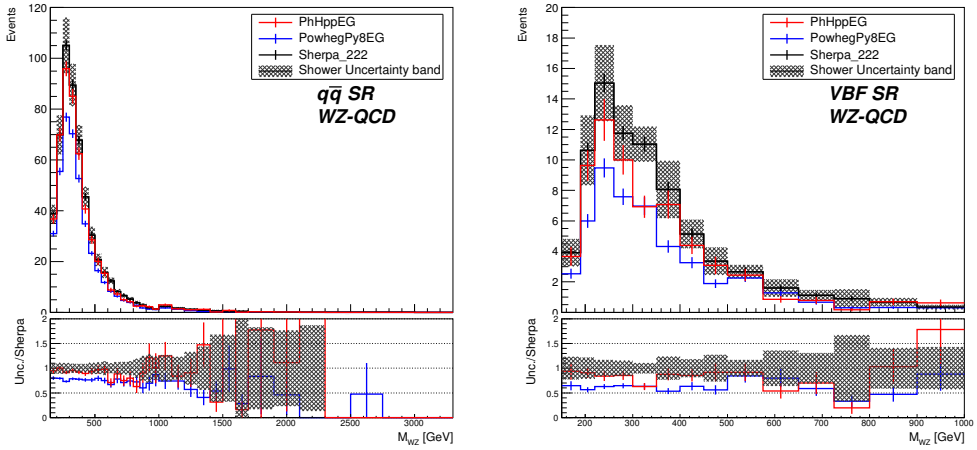

FIGURE 5.22: Comparison of the M_{WZ} distribution between SHERPA 2.2.2, POWHEG+HERWIG and POWHEG+PYTHIA8 event generators in VBF SR on the left and $q\bar{q}$ SR in the right. The parton shower uncertainty is shown by shaded grey bands.

The parton shower and MC generator uncertainties are obtained in a similar way for the WZ EW background, by comparing a MADGRAPH+PYTHIA8 samples with the default SHERPA 2.2.2 sample. Once again the per-bin difference of these two samples in addition to the statistical uncertainty of the MADGRAPH+PYTHIA8 sample is used as an estimate the generator uncertainty of the SM EW sample, as can be seen in figure 5.23.

The uncertainties assigned to the cross sections of the other background sources consist of a contribution from PDF uncertainties and QCD scale uncertainties. They are estimated to be 10% for ZZ, 13% for ttV, 20% for VVV and 15% for tZ.

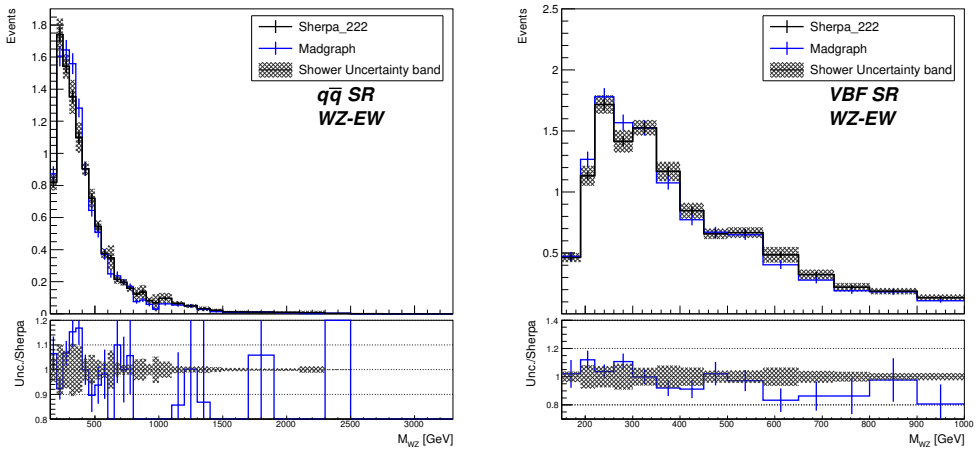

FIGURE 5.23: Comparison of the M_{WZ} distribution between SHERPA 2.2.2 and MADGRAPH+PYTHIA8 event generators in VBF SR on the left and $q\bar{q}$ SR in the right. The parton shower uncertainty is shown by shaded grey bands.

5.7.2 Systematic uncertainties on the fake background estimation

The statistical uncertainty on the final matrix method yield, will correspond to the statistical uncertainty on the terms N_{TTL}, N_{TLT}, N_{LTT}, N_{TLL}, N_{LTL} and N_{LTL} of equation 5.7. The complete list of systematic uncertainties considered in this analysis is given below separately for muon and electron channels.

For the fake electron estimation, the following sources of systematic uncertainty are considered :

— Statistical uncertainties on the fake ratios F_i.

— The bias due to the $E_{\mathrm{T}}^{\mathrm{miss}}$ cut and W transverse mass cut. To estimate the uncertainty related to this selection, the $E_{\mathrm{T}}^{\mathrm{miss}}$ cut is loosened to 20 GeV and tightened to 40 GeV and the largest difference between the new measurements and the nominal one is taken as the systematic uncertainty. The same procedure is followed for the W transverse mass requirement, which is altered to 30 and 50 GeV.

In the case of the fake muons estimation, the following sources of systematic uncertainty are considered :

— Statistical uncertainties on the fake ratios F_i.

— The bias due to the d_0 significance cut : this cut is applied to select the Z+jets control region. To estimate an uncertainty with the same procedure as above, the d_0 cut is consecutively loosened to 2.4 and tightened to 3.6.

— The bias due to the $E_{\mathrm{T}}^{\mathrm{miss}}$: this cut is applied to select the Z+jets control region. Here, the $E_{\mathrm{T}}^{\mathrm{miss}}$ cut is consecutively loosened to 20 GeV and tightened to 40 GeV, to estimate the uncertainty.

The total uncertainty on the fake background estimation is 15% (22%) for the $q\bar{q}$ (VBF) category. The difference can mainly be attributed to the lower statistics available in the VBF category.

5.7.3 Systematic uncertainties on the signal samples

The influence of uncertainties associated with the PDF sets used in the generation of the signal MC samples on the acceptance is evaluated for all the signal samples. Truth derivation samples are produced containing the PDF information and a PDF reweighting method is applied at truth particle level to estimate the uncertainties.

For the $q\bar{q}$ HVT signal, samples are produced with the NNPDF LO [109] PDF sets. The intrinsic uncertainties associated with this set are evaluated by looking at the ensemble sets and the standard deviation is taken as the uncertainty. The NNPDF set is also compared to the CTEQ6L [110] and MSTW2008lo68cl [111] sets and the difference is taken as extra uncertainties. The total PDF uncertainty is computed by adding the internal variations and PDF comparisons in quadrature. For the truth level analysis event selection cuts are applied that closely mimic those used in the reconstruction level analysis. The inclusive fiducial volume is defined as :

1. Exactly 3 leptons with $p_{\mathrm{T}} > 25$ GeV and $|\eta| < 2.5$.
2. Leading lepton $p_{\mathrm{T}} > 27$ GeV,
3. truth $E_{\mathrm{T}}^{\mathrm{miss}}$>25 GeV
4. Z mass : $|M_{\ell\ell} - 91.18| < 20$ GeV
5. $p_{\mathrm{T}}^{\mathrm{Z}}/\mathrm{m_{WZ}} > 0.35$ and $p_{\mathrm{T}}^{W}/\mathrm{m_{WZ}} > 0.35$

The relative uncertainty on the acceptance is found to vary from 2% to 5% and is shown in table 5.I.

mass [GeV]	NNPDF	CTEQ6L1	MSTW	total
500	± 1.69%	± 0.34%	± 0.23%	± 1.74%
600	± 1.89%	± 0.61%	± 0.19%	± 2.00%
700	± 2.14%	± 0.31%	± 0.77%	± 2.29%
800	± 2.21%	± 0.87%	± 1.51%	± 2.81%
1000	± 2.31%	± 1.42%	± 1.64%	± 3.17%
1100	± 2.38%	± 2.11%	± 2.78%	± 4.22%
1200	± 2.25%	± 2.56%	± 2.25%	± 4.08%
1300	± 2.44%	± 2.90%	± 2.77%	± 4.69%
1500	± 3.03%	± 2.31%	± 1.86%	± 4.24%
1600	± 2.67%	± 3.36%	± 2.48%	± 4.96%
1700	± 2.70%	± 2.80%	± 1.79%	± 4.28%
1800	± 3.02%	± 2.99%	± 2.14%	± 4.76%
1900	± 2.87%	± 3.45%	± 2.22%	± 5.00%
2000	± 3.11%	± 3.13%	± 1.66%	± 4.71%
2200	± 3.39%	± 3.73%	± 1.14%	± 5.17%
2400	± 3.46%	± 3.75%	± 1.26%	± 5.26%
2600	± 3.33%	± 3.83%	± 1.14%	± 5.20%
2800	± 3.84%	± 3.52%	± 0.19%	± 5.22%
3000	± 3.62%	± 3.44%	± 0.40%	± 5.01%
3500	± 3.55%	± 3.75%	± 0.27%	± 5.17%
4000	± 4.09%	± 1.86%	± 3.63%	± 5.78%
4500	± 3.88%	± 1.74%	± 3.02%	± 5.21%

TABLE 5.I: The relative uncertainties on the acceptance due to PDF for the HVT W' signal in the $q\bar{q}$ category.

The theory uncertainty of the VBS signal samples is evaluated in a similar way as for the quark fusion category. The truth level event selection cuts once again closely mimic those used in the reconstruction level VBF-analysis :

1. exactly 3 leptons with $p_{\mathrm{T}} > 25$ GeV and $|\eta| < 2.5$
2. truth $E_{\mathrm{T}}^{\mathrm{miss}}$>25 GeV

3. exactly two jets with $|\eta| < 4.5$
4. di-jet mass of at least 500 GeV and an η separation of 3.5

The relative uncertainty on the acceptance for the VBS GM signal samples is found to vary from 1% to 5% and is shown in table 5.II. Likewise, the relative uncertainty on the acceptance of the VBS HVT signal samples is shown in table 5.III.

mass [GeV]	NNPDF	CTQ6L1	MSTW	total
200	± 1.57%	± 2.36%	0.01%	2.83%
250	± 1.44%	± 2.75%	1.60%	3.49%
300	± 1.67%	± 2.13%	0.73%	2.80%
350	± 1.55%	± 2.89%	0.72%	3.36%
400	± 1.89%	± 2.19%	1.76%	3.39%
425	± 1.68%	± 2.01%	0.28%	2.64%
450	± 1.69%	± 2.24%	0.16%	2.81%
500	± 1.90%	± 2.27%	1.75%	3.44%
600	± 2.02%	± 2.30%	2.23%	3.79%
700	± 2.11%	± 2.34%	2.68%	4.14%
800	± 2.27%	± 2.51%	2.93%	4.48%
900	± 2.35%	± 2.58%	3.39%	4.87%

TABLE 5.II: The relative uncertainties on the acceptance due to PDF for the GM $H_5^{\pm}$ signal in the VBF category.

5.7.4 Experimental uncertainties

The uncertainty in the integrated luminosity is 2.1%. It is derived, following a methodology similar to the one in Reference [112], which describes the luminosity determination in pp collisions at $\sqrt{s} = 8$ TeV. The absolute luminosity is determined with the van der Meer (vdm) method [113], carried out under special beam conditions. The obtained absolute calibration of the luminosity must then be transferred to the routine physics running conditions and corrections must be applied to compensate for detector ageing.

mass [GeV]	NNPDF	CTQ6L1	MSTW	total
250	± 1.23%	± 1.84%	± 0.88%	± 2.38%
300	± 1.69%	± 2.04%	± 0.77%	± 2.76%
400	± 1.63%	± 1.76%	± 1.36%	± 2.76%
500	± 1.76%	± 2.17%	± 1.75%	± 3.30%
600	± 1.85%	± 2.21%	± 2.47%	± 3.80%
700	± 1.95%	± 2.37%	± 2.49%	± 3.95%
800	± 2.10%	± 2.19%	± 3.04%	± 4.30%
900	± 2.21%	± 2.60%	± 3.54%	± 4.92%
1000	± 2.33%	± 2.33%	± 3.77%	± 5.01%
1100	± 2.49%	± 2.93%	± 3.64%	± 5.29%
1200	± 2.58%	± 3.55%	± 3.53%	± 5.63%
1300	± 2.61%	± 3.01%	± 4.56%	± 6.06%
1400	± 2.77%	± 3.30%	± 4.79%	± 6.44%
1500	± 3.01%	± 3.11%	± 4.91%	± 6.55%
1600	± 3.07%	± 3.78%	± 4.39%	± 6.56%
1700	± 3.15%	± 3.18%	± 5.39%	± 7.01%
1800	± 3.21%	± 3.51%	± 4.97%	± 6.88%
1900	± 3.23%	± 3.29%	± 5.53%	± 7.20%
2000	± 3.29%	± 3.60%	± 5.57%	± 7.40%

TABLE 5.III: The relative uncertainties on the acceptance due to PDF for HVT W' signal in the VBF category.

To use the measured interaction rate, each detector and algorithm must be calibrated using dedicated vdm scans to infer the delivered luminosity. In the vdm scans the bunch intensities are greatly reduced with only a few tens of widely spaced bunches circulating. These special conditions allow reducing systematic uncertainties in the calibration procedure. To calibrate the luminosity, the visible interaction rate is measured as a function of the nominal beam separation in two orthogonal scan directions (x and y), the special vdm scans for the 2015-2016 run period were performed in August 2015 and May 2016.

5.8 Statistical procedure

The WZ invariant mass distribution, m_{WZ}, obtained as the sum of all four lepton-flavour permutations, is used as the final discriminating variable in this analysis. The bin width is chosen so that it is comparable to the expected experimental resolution of a narrow resonant signal. The expected resolution is estimated with the help of the signal MC. The width of the peak, obtained by a Gaussian fit, is plotted as a function of the resonance mass and is fitted to a polynomial function, see figure 5.24. The polynomial is then used to define the bin width. However, for the high mass tail, the last bin is enlarged to avoid bins with too low MC statistics.

5.8.1 Search as a statistical test

The analysis uses a frequentist statistical test to look for new phenomena, similar to [114] and [115]. To discover a new signal process, one defines the following hypothesis : H_0 is the null hypothesis, describing only known processes to be tested against H_1 which includes both backgrounds as well as the sought-after signal. When setting limits the model with signal and background plays the role of H_0 which is tested against the background-only hypothesis.

The outcome of a search quantifies the level of agreement of the observed data with a given hypothesis H by computing a p-value, under the assumption of H, of finding data of equal or greater incompatibility with the predictions of H. A hypothesis is regarded as excluded if its p-value is observed below a specific threshold.

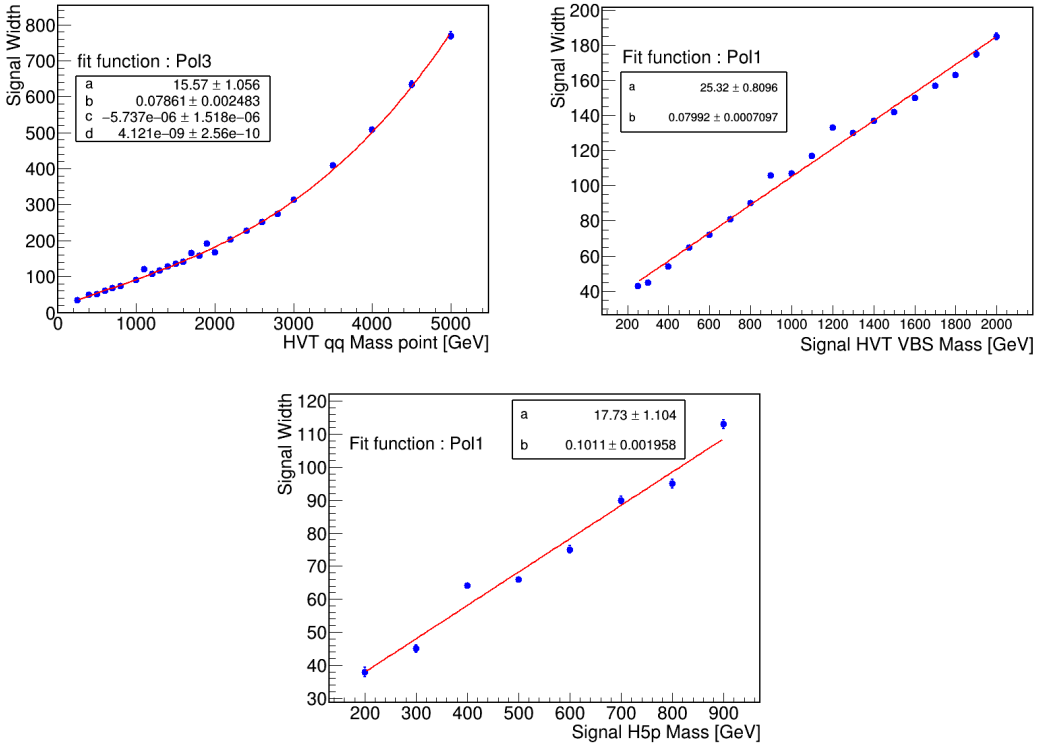

FIGURE 5.24: Width of the resonance peak as a function of the resonance mass, for the $q\bar{q}$ and the VBF signal models.

In particle physics, the p-value is usually converted into an equivalent significance, Z, defined so that a Z standard deviation upward fluctuation of a Gaussian random variable would have an upper tail area equal to p, so

$$Z = \Phi^{-1}(1 - p) \, . \tag{5.8}$$

Here Φ is the cumulative distribution of the standard Gaussian. For a signal process, the particle physics community tends to regard $Z = 5$ as an appropriate threshold to qualify as a discovery, which corresponds to $p = 2.87 \times 10^{-7}$. The actual degree of belief, however, depends on other factors, such as the degree to which it can describe the data and possible correction for multiple observations referred to as the "look-elsewhere effect".

A common procedure to establish discovery or exclusion in particle physics is based on a frequentist significance test using the likelihood ratio as a test statistic. Besides the parameters of interest, such as the rate of the signal process and backgrounds, it contains systematic uncertainties, referred to as *nuisance parameters*, whose values are not known *a priori* but must be fitted from the data.

Here, as an illustration of the use of the likelihood in an analysis with binned kinematic histograms [114]. Suppose that for each event in the signal sample one measures a variable x and uses this variable to construct a histogram $\mathbf{n} = (n_1, ..., n_N)$. If n follows a Poisson distribution then the likelihood becomes

$$L(\mu, \theta) = \left[\prod_{j=1}^{N} \frac{(\mu s_j + b_j)^{n_j}}{n_j!} \exp^{-(\mu s_j + b_j)} \right] , \tag{5.9}$$

where the parameter μ determines the strength of the signal process, with $\mu = 0$ corresponding to the background-only hypothesis and $\mu = 1$ being the nominal signal hypothesis, s_i and b_i refer to the ith bin from signal and background respectively and are functions of the nuisance parameters θ.

The maximum likelihood (ML) estimators for θ are defined as the values that give the maximum of L. It is usually easier to work with ln L. The ML estimators can be found

by finding the maximum of the likelihood ratio :

$$\lambda(\mu) = \frac{L(\mu, \hat{\hat{\theta}})}{L(\hat{\mu}, \hat{\theta})}\,, \tag{5.10}$$

since maximising the likelihood is equivalent to maximising the likelihood ratio. The double-hat notation indicates the value of the parameter that maximises L for the specified μ, so it is the ML estimator of θ. The denominator maximises the likelihood function, so $\hat{\mu}$ and $\hat{\theta}$ are their ML estimators.

From the definition of 5.10 we can see that $0 \leq \lambda \leq 1$, with λ near 1 implying a good agreement between data the hypothesised value of μ. Often the equivalent statistic t_μ is used as a basis for the statistical test

$$t_\mu = -2\ln\lambda(\mu)\,. \tag{5.11}$$

The p-value

$$p_\mu = \int_{t_{\mu,\mathrm{obs}}}^{\infty} f(t_\mu|\mu)dt_\mu\,, \tag{5.12}$$

quantifies the level of disagreement of data with the hypothesis. The value $t_{\mu,\mathrm{obs}}$ is the statistics observed from the data and $f(t_\mu|\mu)$ denotes the PDF of t_μ under the assumption of the signal strength μ.

For a discovery, $\hat{\mu}$ is constrained to be ≥ 0 in equation 5.10. For upper limits the following test statistic

$$q_\mu = \begin{cases} -2\ln\lambda(\mu) & \hat{\mu} \leq \mu, \\ 0 & \hat{\mu} > \mu\,, \end{cases} \tag{5.13}$$

is used. Higher values of q_μ represent larger incompatibility between data and the hypothesis of a signal of strength μ.

Once again the level of agreement between data and hypothesised μ value can be quantified with the p-value. For an observed value $q_{\mu,\mathrm{obs}}$, one has

$$p_\mu = \int_{q_{\mu,\text{obs}}}^{\infty} f(q_\mu|\mu) dq_\mu \, . \tag{5.14}$$

Now consider a test of the strength parameter μ, which can either be zero or nonzero and supposing the data are distributed according to a strength parameter μ'. Then, for a single parameter of interest, an approximated (asymptotic approximation) distribution $f(q_\mu|\mu')$ can be found using this equation [116] :

$$-2\ln\lambda(\mu) \simeq \frac{(\mu-\hat{\mu})^2}{\sigma^2} + O(1/\sqrt{N}) \, , \tag{5.15}$$

assuming that $\hat{\mu}$ follows a Gaussian distribution with mean μ' and standard deviation σ.

5.8.2 Statistical procedure in the WZ-Analysis

This analysis uses a binned likelihood function constructed as a product of Poisson probability terms as in equation 5.9. The systematic uncertainties described in section 5.7 enter as a set of nuisance parameters (NP) θ, which are parameterised by Gaussian or log-normal priors ; the latter ensures positive likelihood. The expected numbers of signal and background events in each bin are functions of θ. The priors act to constrain the NPs to their nominal values within their assigned uncertainties. They act as penalty terms which always increase when any nuisance parameter is shifted from its nominal value. The nominal fit result in terms of μ and σ_μ is obtained by maximising the likelihood function with respect to all parameters, also referred to as the maximised log-likelihood value. The fit is implemented using the RooStats package [117] and performed in the SR for the $q\bar{q}$ and VBF categories separately.

The numbers of background events are extracted through a background-only fit of the data in each category. Background contributions from prompt leptons, including their shapes, are taken from MC simulations. In the case of non-prompt leptons the background shapes are taken from the Matrix Method, see section 5.6.1. In the fit, the normalisation of all backgrounds is allowed to vary within their uncertainties.

The test statistics presented in equation 5.13 is used to test for discovery and to

set exclusion intervals using the CL_s method [118], which was used for the Higgs boson search at LEP. The limit set on a hypothetical signal of strength μ relative to the benchmark model is then translated into limits on the signal cross section times branching ratio, $\sigma \times \mathrm{BR}$, using the theoretical cross section and branching ratio for the given signal model.

5.9 Results

Once the fit is performed the effects of systematic uncertainties can be studied. The list of leading sources of uncertainty in the 95% confidence level (CL) upper limit on the μ value is presented in Table 5.IV together with their relative importance ($\Delta\mu/\mu$). Values are given separately for a hypothetical HVT signal of mass $m(W') = 800$ GeV in the $q\bar{q}$ category and a GM signal of mass $m(H_5^{\pm}) = 450$ GeV in the VBF category. We conclude that, apart from the statistical uncertainties, the uncertainty with the largest impact on the sensitivity of the searches is related to the WZ background modelling.

The post-fit background yields obtained are summarised in Table 5.V for the $q\bar{q}$ and VBF categories. The fit constrains the SM WZ background estimate to the observed data, which reduces the total background uncertainty, pulling the modelling uncertainties by less than one standard deviation from their pre-fit values. None of the nuisance parameters is significantly pulled or constrained relative to their pre-fit values in the background-only fit, as can be seen in figure 5.25 for VBF SR and 5.26 for the $q\bar{q}$ SR.

Figure 5.27 shows the post-fit m_{WZ} distribution for the $q\bar{q}$ and VBF categories. The largest difference between the observed data and the SM background prediction is in the VBF category. A local excess of events at a resonance mass of around 450 GeV can be seen in figure 5.27(b). The local significances for signals of $H_5^{\pm}$ and of a heavy vector W' are 2.9 and 3.1 standard deviations, respectively. The local p_0-value and significance for both models is shown in figure 5.28. The respective global significances calculated using the Look Elsewhere method as in Ref. [119] and evaluated up to a mass of 900 GeV, are 1.6 and 1.9 standard deviations. In the $q\bar{q}$ category the largest difference between the observed data and the SM background prediction is located around a mass of 700 GeV

Source	$\Delta\mu/\mu$ [%]	
	$q\bar{q}$ Category $m(W') = 800$ GeV	VBF Category $m(H_5^{\pm}) = 450$ GeV
WZ modelling : Scale, PDF	5	11
WZ modelling : Parton Shower	10	6
MC statistical uncertainty	7	8
Electron identification	4	2
Muon identification	3	3
Jet uncertainty	1	8
Missing transverse momentum	2	1
Fake/non-prompt	1	5
Total systematic uncertainty	17	21
Statistical uncertainty	53	52

TABLE 5.IV: Impact of the dominant sources of relative uncertainties on the 95% CL upper limits of the signal-strength parameter (μ) for a hypothetical HVT signal of mass $m(W') = 800$ GeV in the $q\bar{q}$ category and a GM signal of mass $m(H_5^{\pm}) = 450$ GeV in the GM category. The effect of the statistical uncertainty on the signal and background samples is also shown. Sources of systematic uncertainty with an impact of less than 2% in both categories are not shown.

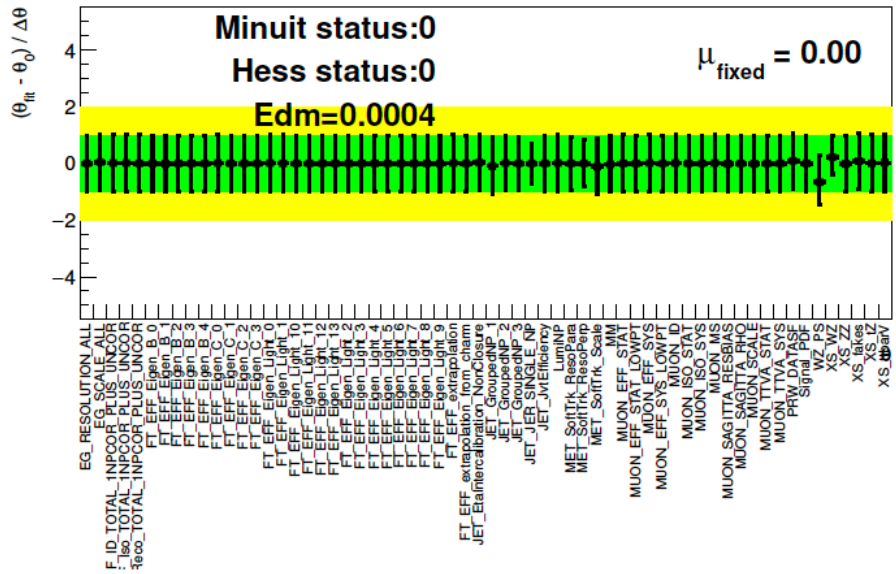

FIGURE 5.25: Nuisance parameter pulls in the VBF signal region with the background-only fit.

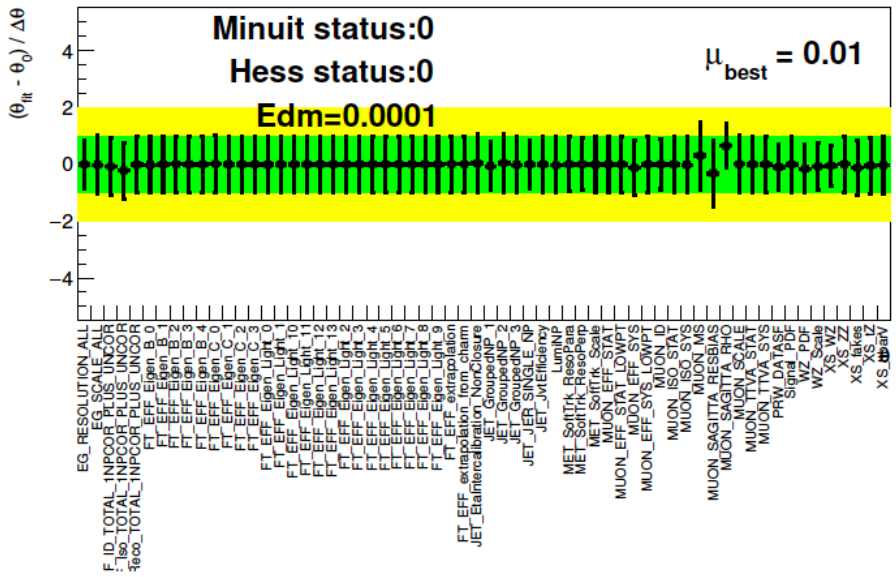

FIGURE 5.26: Nuisance parameter pulls in the $q\bar{q}$ signal region with the background-only fit.

	$q\bar{q}$ Signal Region	VBF Signal Region
WZ	521 ± 29	87 ± 12
Fake/non-prompt	64 ± 13	15 ± 4
$t\bar{t}V$	29 ± 4	4.9 ± 0.8
ZZ	18.9 ± 2.0	4.4 ± 1.0
$tZ + VVV$	14.1 ± 2.9	8.1 ± 1.8
Total Background	647 ± 25	120 ± 11
Observed	650	114

TABLE 5.V: Expected and observed yields in the $q\bar{q}$ and VBF signal regions. Yields and uncertainties are evaluated after a background-only fit to the data in the $q\bar{q}$ or VBF signal regions after applying all selection criteria. The uncertainty in the total background estimate is smaller than the sum in quadrature of the individual background contributions due to anti-correlations between the estimates of different background sources.

with a local significance of 1.2 standard deviations.

Upper limits are set on the production cross section of new resonances and their decay branching ratio into WZ. Exclusion intervals are derived using the CL_s method in the asymptotic approximation mentioned in section 5.8.1. For masses higher than 900 (700) GeV in $q\bar{q}$ (VBF) category, the small number of expected events makes the asymptotic approximation imprecise and the limits are calculated using pseudo-experiments. The limit set on the signal strength μ is then translated into a limit on the signal cross section times branching ratio, $\sigma \times \mathcal{B}(X \to WZ)$, using the theoretical cross section and branching ratio for the given signal model.

Figure 5.29 presents the observed and expected limits on $\mathcal{B}(W' \to WZ)$ at 95% CL for the HVT model in the $q\bar{q}$ category. Masses below 2260 GeV can be excluded for Model A and 2460 GeV for Model B. For resonance masses above 2 TeV, the exclusion limits become worse due to the acceptance losses at high mass. For the VBF process, the limit on $\mathcal{B}(W' \to WZ)$ is shown in Figure 5.30.

Observed and expected exclusion limits at 95% CL on $\sigma \times \mathcal{B}(H_5^{\pm} \to W^{\pm}Z)$ and on the mixing parameter $\sin\theta_H$ of the GM Model are shown in Figure 5.31 as a function of $m_{H_5^{\pm}}$. The intrinsic width of the scalar resonance, for $\sin\theta_H = 0.5$, is narrower than the

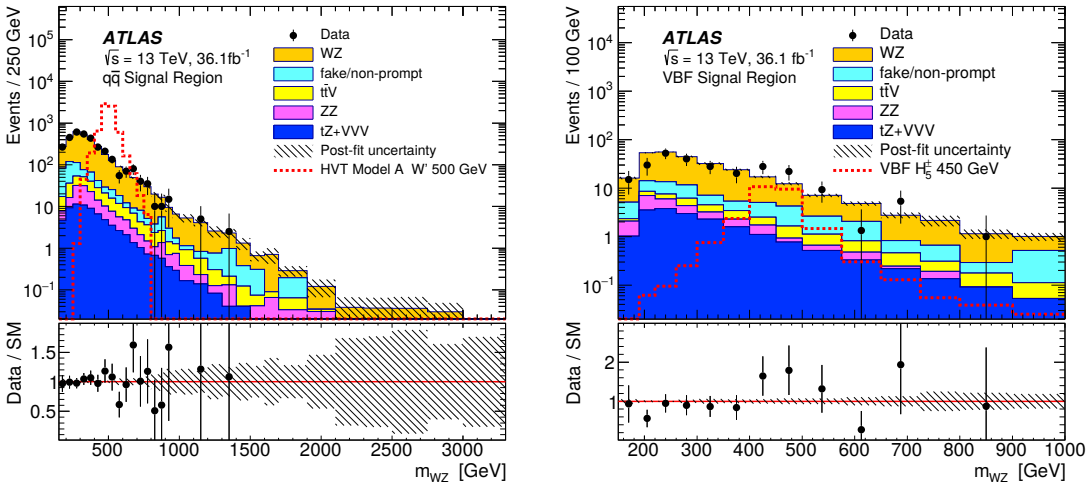

(a) (b)

FIGURE 5.27: Observed and expected distributions of the WZ invariant mass in the $q\bar{q}$ (a) and in the VBF categories (b) after applying all selection criteria. Signal predictions are overlaid, normalised to the predicted cross sections. The uncertainty in the total background prediction, shown as shaded bands, combines statistical, theory and systematic contributions. The lower panel show the ratios of the observed data to the background predictions.

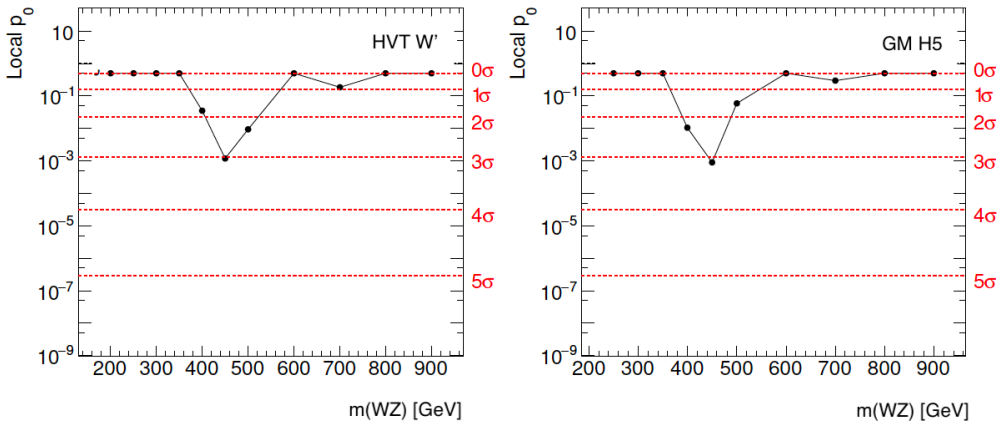

(a) (b)

FIGURE 5.28: Local p_0-values for the VBF analysis using a heavy vector W' (a) and a $H_5^{\pm}$ (b) as a signal hypothesis.

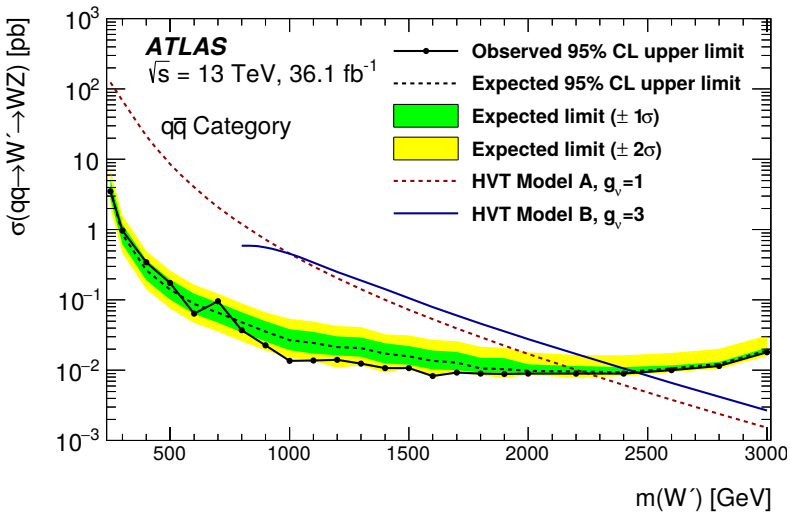

FIGURE 5.29: Observed and expected 95% CL upper limits on $\sigma \times \mathcal{B}(W' \to W^{\pm}Z)$ for the $q\bar{q}$ production of a W' boson in the HVT models as a function of its mass. The theoretical predictions for HVT Models A with $g_V = 1$ and B with $g_V = 3$ are also shown.

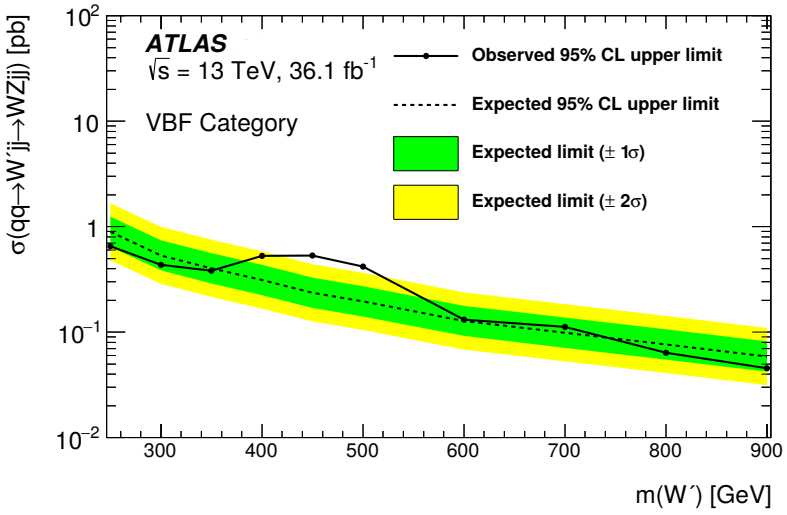

FIGURE 5.30: Observed and expected 95% CL upper limits on $\sigma \times \mathcal{B}(W' \to W^{\pm}Z)$ for the VBF production of a W' boson in the HVT Model, with parameter $c_F = 0$, as a function of its mass. The green (inner) and yellow (outer) bands represent the $\pm 1\sigma$ and $\pm 2\sigma$ uncertainty in the expected limits.

detector resolution in the mass region explored. The shaded regions show the parameter space for which the $H_5^{\pm}$ width exceeds 5% and 10% of $m_{H_5^{\pm}}$.

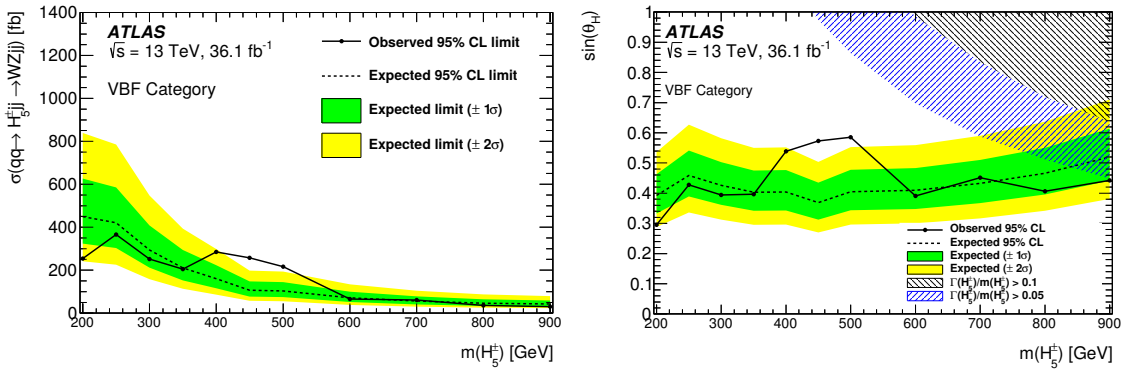

(a) (b)

FIGURE 5.31: Observed and expected 95% CL upper limits on (a) $\sigma \times \mathcal{B}(H_5^{\pm} \to W^{\pm}Z)$ and (b) the parameter $\sin\theta_H$ of the GM Model as a function of $m_{H_5^{\pm}}$. The shaded region shows where the theoretical intrinsic width of the resonance would be larger than 5% or 10% of the mass.

5.9.1 Discussion of the VBF excess

Since a small excess was observed in the VBF SR around 450 GeV, several control plots were produced to check by which particular channel contribution the excess was coming from. Figure 5.32 shows the VBF SR for the various channels. Instead of the fit, the normalisation of all MC samples except the fake background is directly taken from the MC predictions, the fake background is predicted by the matrix method. The excess is predominantly visible in the $\mu^+\mu^-\mu^{\pm}$ and $\mu^+\mu^- e^{\pm}$ channels, but the statistics in the VBF SR is very limited once split by channel contribution.

Similar searches have been performed by CMS, the search for same-sign W Boson pairs [88] allows to set limits on the parameter $\sin\theta_H$ of the GM Model as a function of $m_{H_5^{\pm\pm}}$ as shown in figure 5.33(a) (compare to figure 5.31(b)). Since the masses of all of the members of the fiveplet are, in principle, degenerate, this is testing the same parameters as the search for $H_5^{\pm}$. Primarily because of the very small SM background, this search is

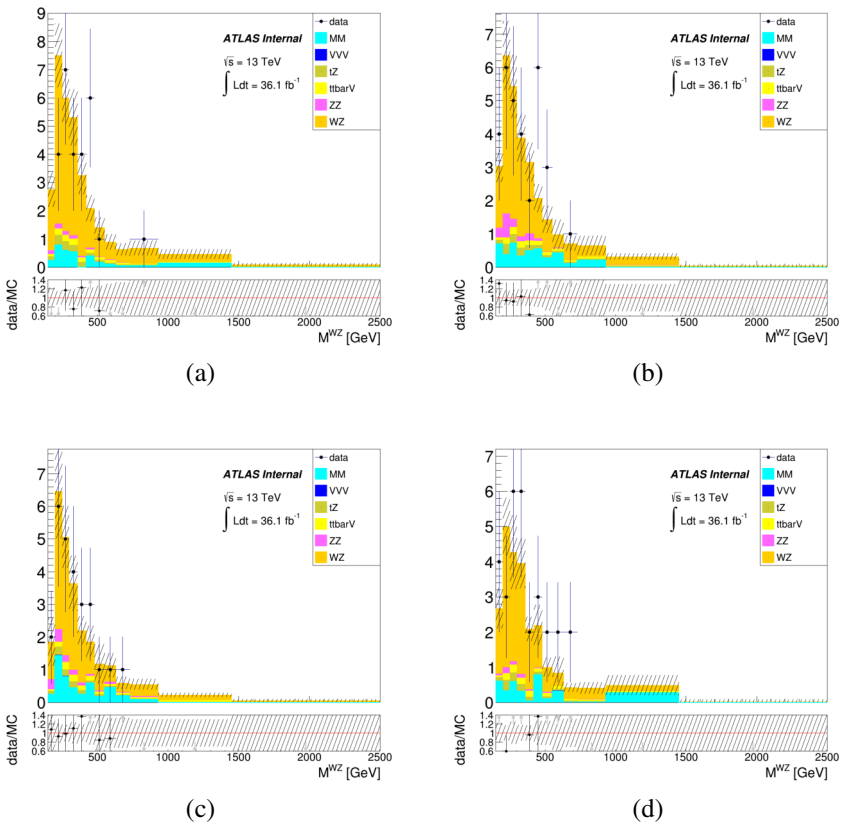

(a) (b)

(c) (d)

FIGURE 5.32: Control distributions of the invariant mass m_{WZ} separated by channels $\mu^+\mu^-\mu^\pm$ (a), $\mu^+\mu^-e^\pm$ (b), $e^+e^-e^\pm$ (c), $e^+e^-\mu^\pm$ (d). All MC expectations are scaled to the integrated luminosity of the data using the predicted MC cross sections of each sample.

able to set better limits on the parameter $\sin\theta_H$. This search is therefore excluding the small excess with confidence over 2σ. A search for resonant WZ production is performed also by the CMS Collaboration. The resulting limits on the parameter $\sin\theta_H$ of the GM Model as a function of $m_{H_5^{\pm}}$ is shown in figure 5.33(b). The ATLAS search has slightly better sensitivity so the excess is neither confirmed nor rejected by the CMS search.

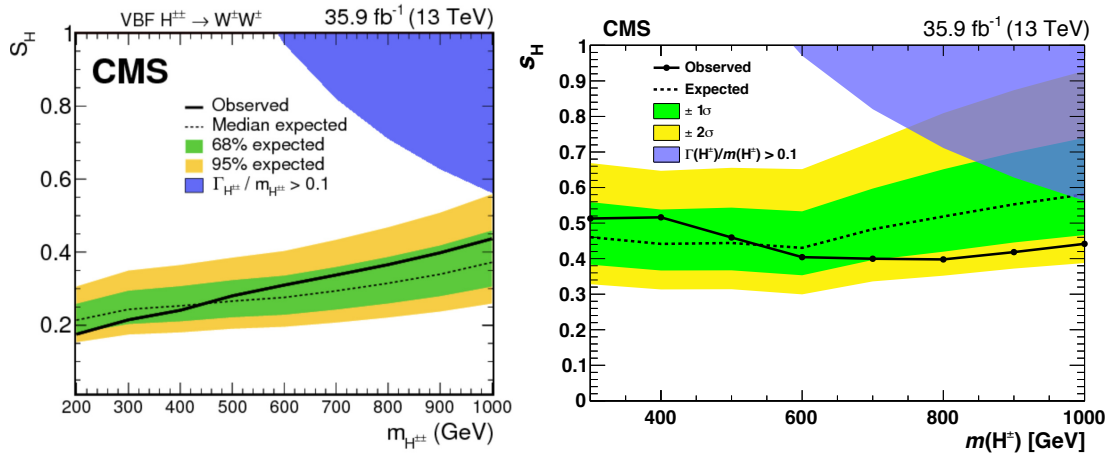

(a) (b)

FIGURE 5.33: Observed and expected 95% CL upper limits on the parameter $\sin\theta_H$ of the GM Model as a function of $m_{H_5^{\pm\pm}}$ (a) [88] and as a function of $m_{H_5^{\pm}}$ [89] by the CMS Collaboration.

As can be seen from figure 5.34 the excess is not excluded by diboson resonance searches with hadronic decays of the W and/or Z boson, as only the fully leptonic decay has sensitivity below 500 GeV.

5.10 Combination

As mentioned in section 5.1 there are many available channels to look for heavy resonances like the W'. The best limits can be obtained by combining all the various channels. The ATLAS collaboration therefore performed a combination of searches for heavy resonances decaying into VV (with $V = W$ or Z) and VH (H is the SM Higgs boson) covering all possible decay channels of the bosons as well as analyses selecting

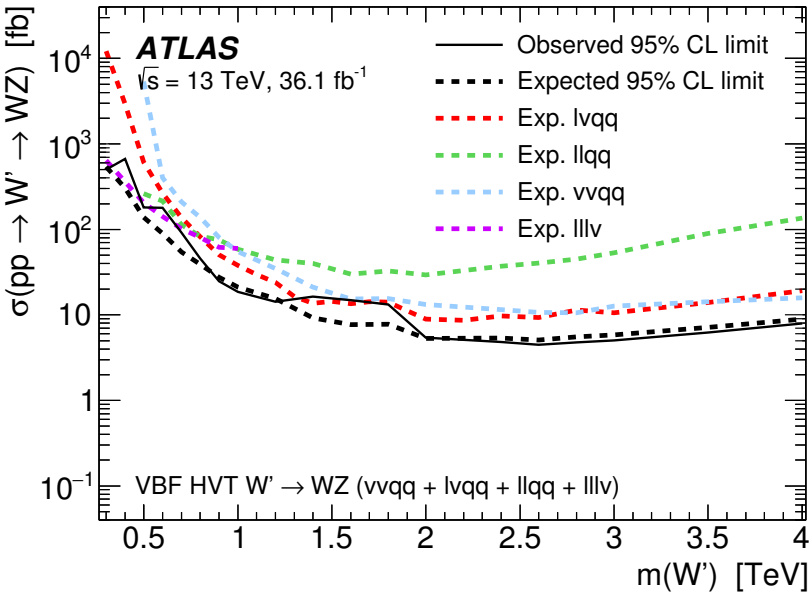

FIGURE 5.34: Observed and expected 95% CL upper limits on the W' cross section times branching fraction to WZ for the HVT benchmark model. Expected limits for individual channels and their combination are shown for the VBF production mechanisms.[77]

the leptonic $\ell\nu$ and $\ell\ell$ final states [120]. This combination therefore includes results of the $WZ \to \ell\nu\ell\ell$ analysis described above. Both the HVT Model A and Model B are tested in the quark/gluon-fusion channel (Drell-Yan). The results for the combination of $VV + VH$ can be seen in figure 5.35(a). V' refers to either the W' or the Z' of the HVT model and figure 5.35(b) shows the combination of $VV + VH + \ell\ell + \ell\nu$. The di-boson analysis provides the best limits on the weakly coupled scenario HVT Model B, excluding a heavy resonance V' up to a mass of 4.5 TeV. The di-lepton analysis provide the best limits in the strongly coupled scenario HVT Model A, excluding resonance masses below 5.5 TeV in this scenario. This search is also used to do a full parameter scan of the HVT model parameters g_f, g_H as well as g_l and g_q (see section 3.3 for details). Results of the full combination as well as constraints from EW-precision measurements [121] are shown in figure 5.36 in both the $\{g_H, g_f\}$ and $\{g_q, g_l\}$ plane. The limits of the combination greatly restraints the available parameter space except for very small coupling values to fermions $g_f \sim 0$.

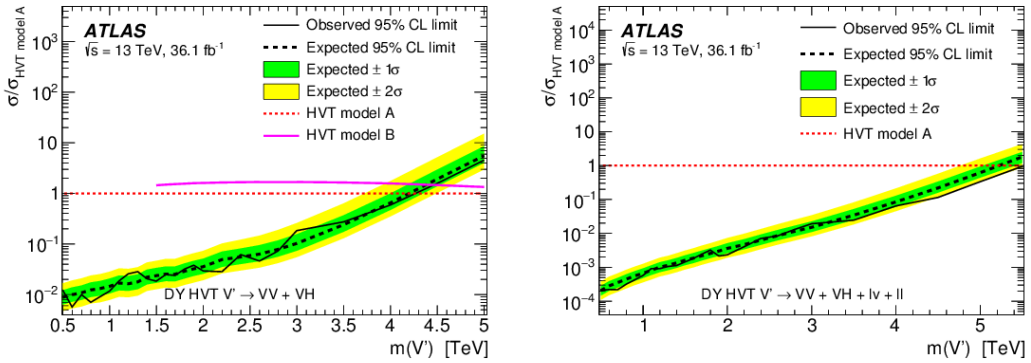

(a) (b)

FIGURE 5.35: Observed and expected 95% C.L. upper limits on the V' cross section times branching fraction to (a) VV/VH and (b) $VV/VH/\ell\ell/\ell\nu$ for the HVT benchmark model, relative to the cross section for HVT model A. The model predictions are also shown [120].

The searches for VBF-production mode have been combined for the various WW and WZ decay channels [122]. However, the combination is only performed for resonance

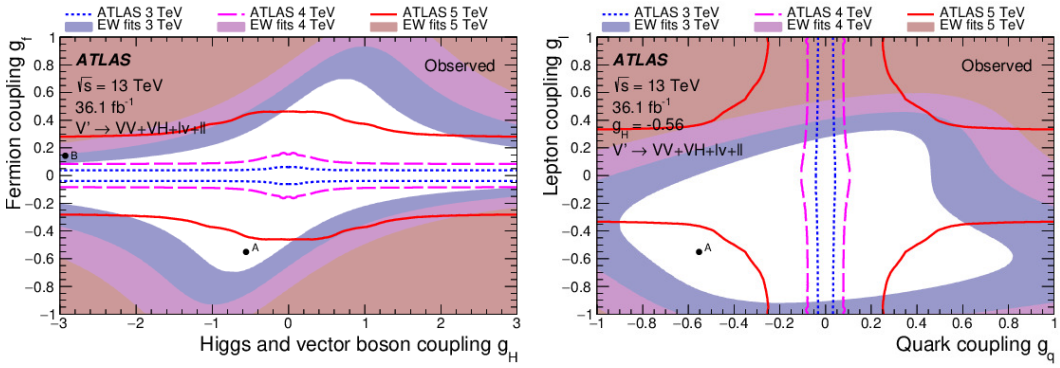

(a) (b)

FIGURE 5.36: Observed 95% C.L. exclusion contours in the HVT parameter space (a) $\{g_H, g_f\}$ and (b) $\{g_q, g_l\}$ for resonances of mass 3, 4, and 5 TeV for the combination of the VV, VH, and $\ell\nu/\ell\ell$ channels. The areas outside the curves are excluded, as are the filled regions which show the constraints from precision EW measurements. Also shown are the parameters for models A and B.

masses above 0.5 TeV. Below that mass, the $WZ \to \ell\nu\ell\ell$ analysis has by far the greatest sensitivity, as seen in figure 5.34. The resulting limits on the V' cross section times branching fraction relative to the HVT model C, which is identical to the VBF benchmark model defined in section 5.1, is shown in figure 5.37. The search has presently no sensitivity with the model parameter combination $g_H = g_V = 1$ and $g_f = 0$.

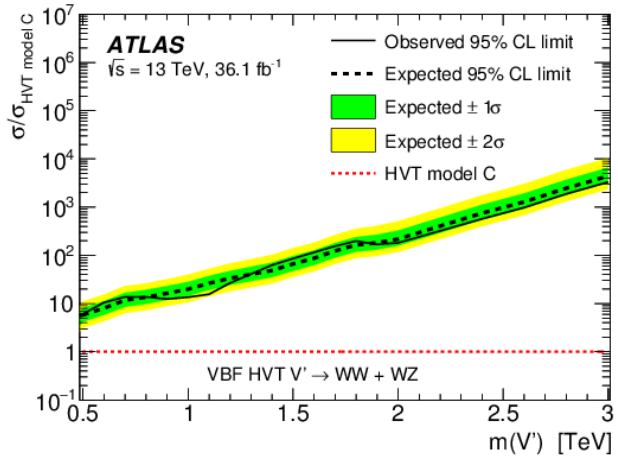

FIGURE 5.37: Observed and expected 95% C.L. upper limits on the V' cross section times branching fraction to WW or WZ for the HVT benchmark model, relative to the cross section times branching fraction for HVT model C. Results are shown for VBF production mechanisms. The model predictions are also shown. [83]

CHAPITRE 6

PREPARATION FOR FULL RUN-2 WZ ANALYSIS

Now that the paper has been published with 36 fb^{-1}, an updated analysis with the full run-2 data set is prepared, corresponding to an integrated luminosity of approximately 139 fb^{-1}. This much larger data-set will result in a substantial increase in the sensitivity of the search, in addition several ideas are implemented to improve the analysis and improve on shortcomings of the previous analysis. Here a list of some of these shortcomings as well as possible solutions :

1. Given the small excess in the Vector Boson Fusion (VBF) signal region, there is a general interest in either confirming or excluding this excess. Therefore, the VBF signal region selection should be improved as much as possible to increase the sensitivity of the analysis. In the following section a Multivariate Analysis (MVA) technique will be presented, it will be shown that machine learning helps to improve the selection. Some preliminary results with this technique will be shown in section 6.1.
2. With the increased sensitivity, it is possible to explore higher masses in the VBF signal region. Therefore Next-to-leading order (NLO) Georgi-Machacek (GM) signal samples with a higher range of resonance masses has been requested to replace the older leading order (LO) samples, while also improving the kinematic predictions of the Monte Carlo (MC) signal samples. A brief summary of this request is presented in section 6.2.
3. Looking back at the signal acceptance times efficiency in the $q\bar{q}$ category, see figure 5.13, we can observe a decrease in the acceptance for resonance masses above 2 TeV in the $\mu\nu ee$ and $e\nu ee$ channel. For these very large resonance masses, the resulting Z boson will be highly boosted. Electron-positron pairs are then treated as a single high p_{T} object because they no longer pass the isolation cuts for electrons and therefore fail the three lepton selection. To address this issue

a proposal to identify these *fat*-electron jets is presented in section 6.3.

6.1 Machine Learning algorithms for classification

In the published analysis, very simple selection cuts were applied in the VBF category using the di-jet mass, m_{jj}, and eta separation of the two p_{T} -leading jets $\Delta\eta_{jj}$. The signal selection was not mass dependent. However, these variables are highly dependent on the signal masses (see figure 5.8). Besides, there are a lot more discriminating variables that can be used in the selection, for example, the kinematic variables of the leptons and jets etc. To improve the sensitivity of the analysis, machine learning algorithms can be used to classify signal and background events. Two kinds of MVA algorithms are being studied, Artificial Neural Network (ANN) and Boosted Decision Trees (BDTs) which will be briefly discussed below. This is a binary classification task, where we want to categorise events to belong either to the VBF signal region or the background.

6.1.1 Artificial Neural Networks

ANN are learning algorithms inspired by the biological brain [123]. They are not realistic models of biological functions but are used to learn to perform tasks by considering examples. McCulloch and Pitts [124] developed an early model of the brain function in the 1940s. This model takes a set of n inputs $x_1, ..., x_n$, applies a set of weights $w_1, ..., w_n$ and adds a bias b to compute an output y, $y = f(\boldsymbol{x}, \boldsymbol{w}) = x_1 w_1 + ... + x_n w_n + b$. The McCulloch-Pitts neuron could recognise two categories of inputs by testing if $f(\boldsymbol{x}, \boldsymbol{w})$ is positive or negative. In order to correspond to the desired definition, the weights need to be set accordingly. In the 1950s the perceptron model was developed [125]. It was the first model that could learn the weights by given examples of inputs from each category using stochastic gradient descent. To make the model non-linear, an activation function a, for example $a(y) = \arctan(y)$, is applied on the output of the function f (see figure 6.1). An example of a modern ANN is a Multi-Layer Perceptron (MLP), which is simply a combination of multiple perceptrons stacked in hidden layers. Each neuron is connected to either all inputs or all neurons of the previous hidden layer, the MLP is therefore called

fully connected. A schema of an MLP with one hidden layer used for classification of the output is shown in figure 6.2.

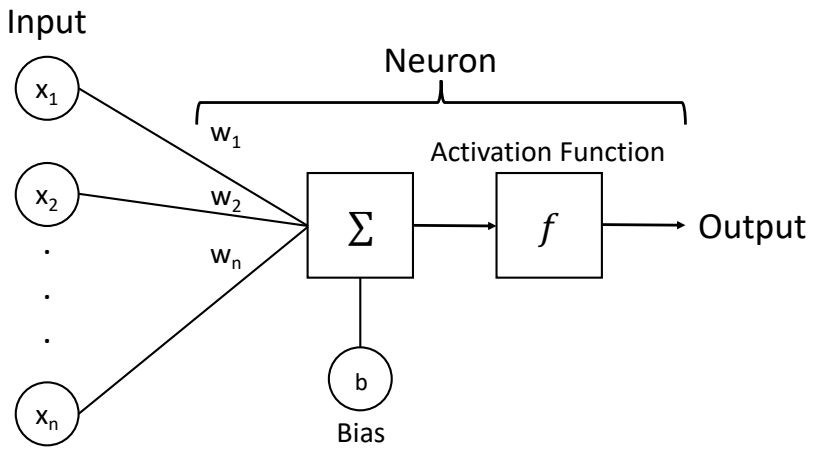

FIGURE 6.1: A Schematic representation of the perceptron.

The use of MLPs has been increasingly popular for classification tasks with the increase in computer power and new theoretical advancement allowing efficient training of deep (meaning many hidden layers) neural networks, see also [127]. In many tasks, neural networks completely outperform other machine learning algorithms and there is also an increased interest to use these techniques in the context of particle physics.

To train these machine learning models, an objective or cost function needs to be defined. Since gradient descent is used to learn the parameters (weights and biases) of the network the function needs to be differentiable. In the case of binary classification, the cross-entropy is often used, defined as :

$$H(p) = -(y \log(p) + (1 - y) \log(1 - p)) \,, \tag{6.1}$$

where p is the classification model output probability value lying between 0 and 1. To minimise the cross-entropy, which is equivalent to maximising the likelihood, gradient descent is used. A function $f(\boldsymbol{x})$ is minimised by taking a step into the negative direction of its gradient

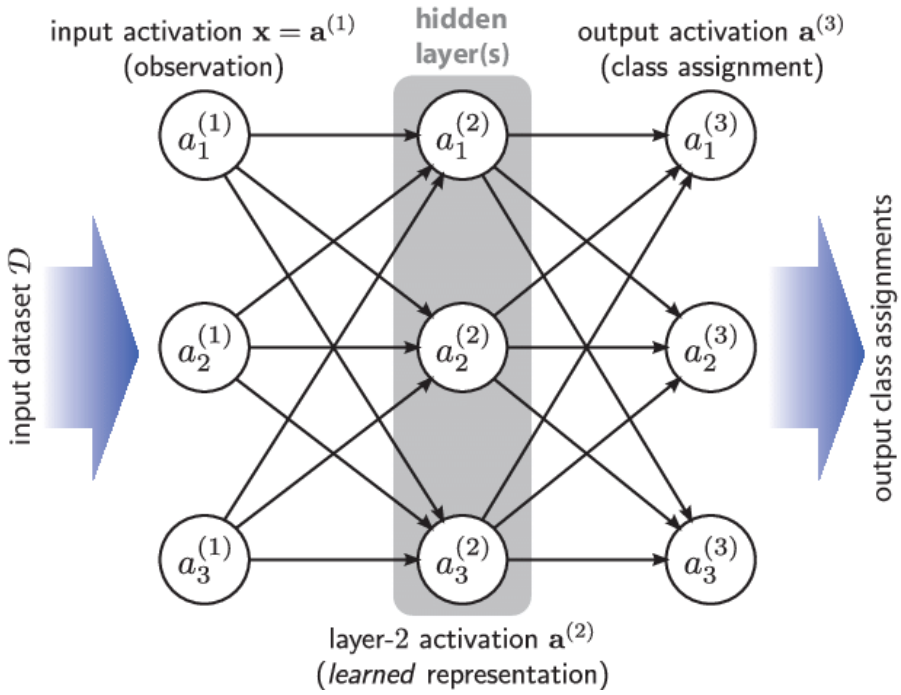

FIGURE 6.2: A Schematic representation of a fully connected MLP with one hidden layer. [126]

$$\boldsymbol{x}' = \boldsymbol{x} - \epsilon \nabla_{\boldsymbol{x}} f(\boldsymbol{x}) \,, \tag{6.2}$$

where ϵ is the learning rate, determining the size of the step. The training is done in two steps, the forward propagation, where the input information $\boldsymbol{x}$ flows through the network to produce output $\boldsymbol{y}$, and a back-propagation, where the information from the cost function flows backwards through the network to compute the gradients.

Besides the parameters that are learned in the training step, several parameters need to be set to control the algorithm's behaviour, these are called hyperparameters. Examples are the structure of the network, the number of neurons and the number of hidden layers, the activation function used, and the learning rate.

6.1.2 Boosted Decision Trees

Decision Trees are commonly used in classification tasks in physics analysis, due to their similarities to classical cut-based analysis and their relatively easy implementation. BDTs, as their name suggests, use the boosting technique. Its basic idea is to combine several "weak" classifiers to form a final powerful classifier. One example of a widely used boosting algorithm is the **AdaBoost** algorithm [128].

The boosting technique is often used in conjunction with Decision Trees, see also [129] for an example of BDT usage in particle physics. In figure 6.3 we can see a schema of a single decision tree. Each event consists of a set of features (variables), a sequence of binary splits, starting from the root node is applied to divide the sample into subsets (branches), here labelled "S" for signal and "B" for background. Each circle represents a node, also called leaves. In the terminal nodes, the final decision is taken. The splitting value at each node is chosen to give the best separation into signal and background. The criterion uses the purity in a node, defined as

$$P = \frac{\sum_S W_S}{\sum_S W_S + \sum_B W_B} \,, \tag{6.3}$$

here W_i is the weight of an event. The criterion is the Gini index defined as

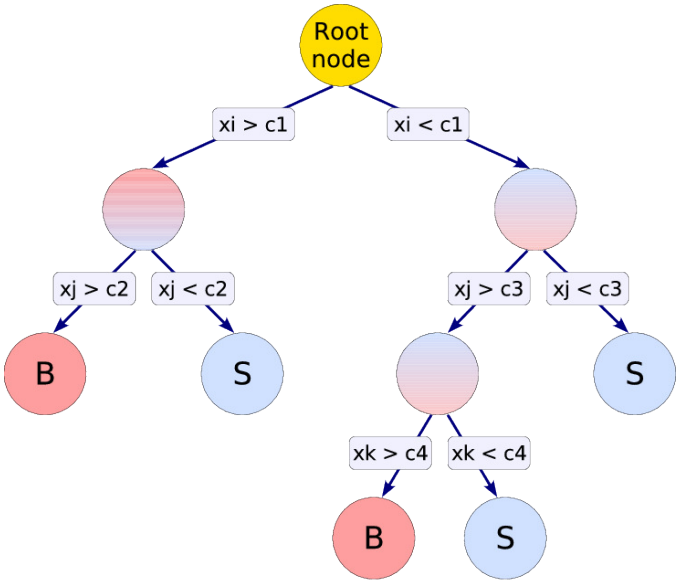

FIGURE 6.3: Schematic view of a decision tree. Starting from the root node, a sequence of binary splits using the discriminating variables x_i is applied to the data. Each split uses the variable that at this node gives the best separation between signal and background when being cut on. The leaf nodes at the bottom end of the tree are labelled "S" for signal and "B" for background depending on the majority of events that end up in the respective nodes. [130]

$$\text{Gini} = \left(\sum_{i=1}^{n} W_i\right) P(1-P)\,, \tag{6.4}$$

n is the number of events in that branch. The index is 0 if the sample is pure signal or pure background. The splitting value can then be learned by minimising the Gini index in each branch.

Now, with the boosting technique, several of these small trees are combined to form a complex classifier. At the beginning, all events have the same weight, but if they are misclassified their weight is increased (boosted). Then in the second tree, the weights are no longer equal and formerly misclassified events will have a greater impact on the Gini index. This procedure is repeated until each event has been evaluated by all trees. The final score is a weighted average over all trees in the ensemble.

6.1.3 Usage of MVA techniques for the VBF selection

For the full run-2 analysis the rather simple cut-based selection of VBF events is going to be replaced by a Machine Learning algorithm to increase sensitivity. Both the BDT and ANN methods have been tried.

The first step consists of identifying variables that are useful for classification. The choice of variables is similar to the ones used in the SM EW WZ measurement, which uses a BDT selection in their signal region [131]. A total of 22 suitable variables are identified for the selection. Variables related to the kinematic properties of the two tagging jets are the invariant mass of the two jets, m_{jj}, the transverse momenta of the jets, the pseudorapidity and the difference in the pseudorapidity angle between the two jets, $\Delta\eta_{jj}$, as well as the jet multiplicity. Variables related to the kinematic properties of the vector bosons are the transverse momenta of the W and Z bosons and the two variables used for the $q\bar{q}$ signal region selection, $p_{\mathrm{T}}^{W}/m_{WZ}$ and $p_{\mathrm{T}}^{Z}/m_{WZ}$, and finally, the centrality of the WZ system relative to the tagging jets, defined as $\zeta_{\text{lep}} = \min(\Delta\eta_{-}, \Delta\eta_{+})$, with $\Delta\eta_{-} = \min(\eta_l^W, \eta_{l2}^Z, \eta_{l1}^Z) - \min(\eta_{j1}, \eta_{j2})$ and $\Delta\eta_{+} = \max(\eta_{j1}, \eta_{j2}) - \max(\eta_l^W, \eta_{l2}^Z, \eta_{l1}^Z)$. The invariant mass is not used as an input parameter to allow the methods to be insensitive to the specific mass point used for the training (see also [132]). However, a label was

added as a variable identifying every signal mass point (0 for a 200 GeV signal, 1 for a 250 GeV signal etc.). The goal is to have a parameterised classifier, that can smoothly interpolate between mass points and replace sets of classifiers trained at individual values. This makes the training easier since only one training is necessary for all mass points while assuring an optimal performance over the whole mass range. The background was assigned a random label corresponding to the same probability distribution as the signal, similar to what is done in [132].

Two optimisations are performed, one for the GM $H_5^{\pm}$ and one for the Heavy Vector Triplet (HVT) W' signal. Since some of the simulated background predictions suffer from large uncertainties (for example the fake/non-prompt), only the well modelled SM WZ and $WZjj$ contributions are considered for the training. These backgrounds constitute the large majority of the SM background processes.

The performance of a machine learning algorithm is judged on how well it performs on new, previously unseen inputs and not the ones used in training. The ability to perform well on unobserved inputs is called generalisation. The generalisation error is usually estimated on a test set of examples, that are separate from the training set. The performance of the algorithm has then two objectives :

1. Making the training error small.
2. Minimizing the gap between training and test error.

These two factors are the two main challenges in ML : underfitting and overfitting. Underfitting occurs when a model is not able to obtain a sufficiently small error on the training set. Overfitting results in a large gap between training and test error. Underfitting is controlled by the capacity of a model, which is basically its ability to fit a wide variety of functions. Models with low capacity may result in underfitting but high capacity models can lead to overfitting, so there is a trade-off in the capacity choice. Typically, the training error decreases when increasing the capacity before rising due to overfitting. Therefore there is an optimal value for the capacity, see also figure 6.4 for an illustration. The capacity is defined by the choice of hyperparameters, if we increase for example the number of hidden layers or the number of trees in the ensemble, the capacity is increased.

To limit overfitting and to reduce the generalisation error, regularisation techniques are used. There are various regularisation techniques, some of these will be presented in the specific implementation of ANN in the WZ full run-2 analysis.

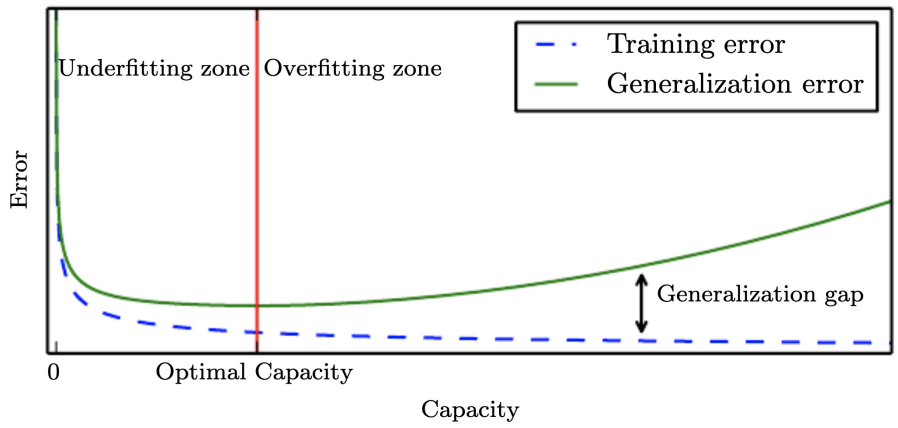

FIGURE 6.4: Typical relationship between capacity and error. Training and test error behave differently. At the left end of the graph, training error and generalization error are both high. This is the underfitting regime. As we increase capacity, training error decreases, but the gap between training and generalization error increases. Eventually, the size of this gap outweighs the decrease in training error, and we enter the overfitting regime, where capacity is too large, above the optimal capacity. [123]

As mentioned above each method has its set of hyperparameters which are not adapted by the learning algorithm. To find optimal hyperparameters and not bias the test sample, a validation set of examples has to be set aside. Below a simple breakdown of the steps we have to perform to train our models :

1. Define models with a set of hyperparameters.
2. Separate the signal and background samples into three categories : one for training the models, the training set, one for optimising hyperparameters, the validation set, and one to estimate the generalisation error, the test set.
3. Set up control and signal region based on the algorithm output.
4. Compare obtained significance with simple cut-based analysis.

The ANN was implemented with the Keras package [133], a high-level neural network python interface running on top of widely used TensorFlow package [134]. The rectified

linear unit [135], or ReLU, defines as $g(z) = \max\{0, z\}$, was used as an activation function, which is the default recommendation in modern neural networks [123]. This function is piece-wise linear, which make them easy to optimise with gradient-based methods. The output activation function is a sigmoid, meaning the output of the ANN will take values between 0 and 1. The stochastic gradient descent optimiser [136, 137] was used, as implemented in the Keras package. The optimiser takes as input the learning rate, see eq. 6.2, and whether to use a technique called Nesterov's Accelerated Gradient (NAG) or Nesterov's momentum [138]. The momentum method is a technique for accelerating gradient descent, inspired by the physical momentum. Given an objective function $f(\theta)$ to be minimised, Nestov's momentum is given by :

$$v_{t+1}^{\text{NAG}} = \mu v_t - \epsilon \nabla f(\theta_t + \mu v_t) \tag{6.5}$$

$$\theta_{t+1} = \theta_t + v_{t+1}\,, \tag{6.6}$$

where μ is the momentum coefficient. NAG is a first-order optimization method with better convergence rate guaranteed than gradient descent [138].

To avoid overfitting, several regularisation techniques are employed, the Dropout technique and early stopping. Dropout [139] is a regularisation technique that can be thought of an easy implementation of a bagging method [123]. The bagging methods consists of training and evaluating multiple models on each test example. For large neural networks and large training sets, this results in a large run-time and memory usage. Dropout, on the other hand, provides an inexpensive approximation to train and evaluate a bagged ensemble of neural networks. Dropout applies a random sample binary mask on the hidden units in the network each time an example is loaded. The probability of sampling one is a hyperparameter fixed before training. The early stopping technique tries to achieve lower validation error by exploiting the usual training behaviour of large capacity models. When these large models capable of overfitting are trained, it is often observed that the training error decreases steadily over time but the validation error reaches a minimum and then rises again, as illustrated in figure 6.5. The criteria for early

stopping was chosen as the measured loss in the validation set. A patience parameter is required which specifies the number of epochs to wait before early stopping is performed, when no decrease in validation loss is observed.

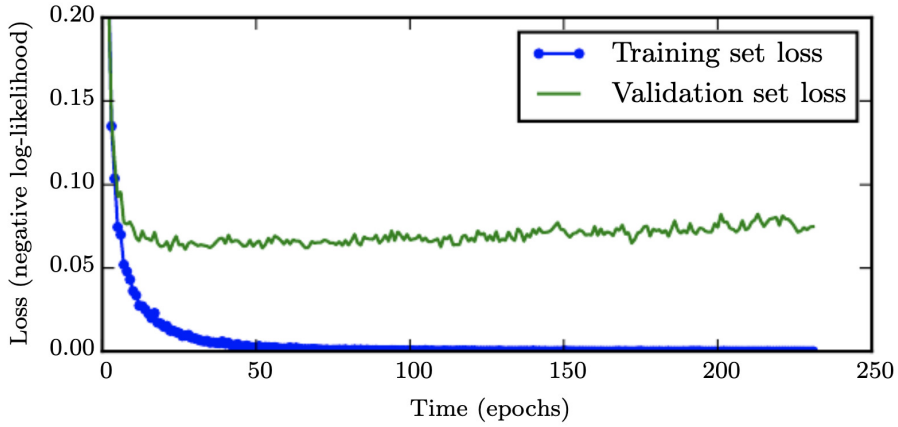

FIGURE 6.5: Typical learning curves showing how the negative log-likelihood loss changes overtime (indicated as number of training iterations over the data-set, or epochs). The training objective decreases consistently over time, but the validation set average loss eventually begins to increase again. [123]

In table 6.I an overview of the hyperparameters used in this analysis is presented for the ANN implementation. These hyperparameters are optimised via a random search, similar to Ref. [140]. The range within a random value is chosen as shown in the same table. In this paper, it is suggested that randomly chosen trials are more efficient for hyper-parameter optimization than trials on a grid, especially in cases where some of the hyperparameters are more important than others.

The BDTs with **AdaBoost** are implemented with the scikit-learn tool [141]. There are fewer hyperparameters in this model compared to the ANN. The necessary hyper-parameters are the following : the maximum depth of each tree, the learning rate, and the number of trees in the boosting ensemble. These hyperparameters are optimised in a similar way as for the ANN. A table with the necessary hyperparameter and the range which was used in the random optimisation is shown in table 6.II.

An illustration of the cross-entropy loss, as defined in eq. 6.1, as a function of the training time (measured in epochs) is shown in figure 6.6. Whereas the loss of the training

Number of hidden layers	1–6
Number of neurons per layer	50–300
Learning rate	0.005–0.05
Dropout probability	0.00–0.6
Patience (early stopping)	1-20
Nesterov momentum	0.6

TABLE 6.I: Overview of the hyperparameters used in the ANN model for the VBF event selection as well as a range used in the random search optimisation.

Maximal Depth of tree	1–5
Number of estimators in ensemble	100–1000
Learning rate	0.001–0.05

TABLE 6.II: Overview of the hyperparameters used in the BDT model for the VBF event selection as well as a range used in the random search optimisation.

sample is always decreasing, the validation loss is stagnating and slowly rising at the end, causing the early stopping mechanism to end the training after ≈ 50 epochs.

Once the ANN and BDT models are trained, the output variable can be used to differentiate between background and signal. Both the BDT and ANN output variable for the training sample is shown in figure 6.7. For both methods we can observe a clear separation between signal and background, signal and control regions can be constructed by cutting on the output value of the two methods.

An approximate significance formula is used with a given cut to estimate the significance Z of observing n events given a prediction of b with variance σ, defined as :

$$Z = \sqrt{2\left(n \ln\left[\frac{n(b+\sigma^2)}{b^2+n\sigma^2}\right] - \frac{b^2}{\sigma^2}\ln\left[1+\frac{\sigma^2(n-b)}{b(b+\sigma^2)}\right]\right)}. \tag{6.7}$$

This formula is similar to equation 5.5 but includes an approximation for Gaussian systematic uncertainties. For now, only statistical uncertainties are considered. The obtained significance assuming an integrated luminosity of 140 fb^{-1} and only considering

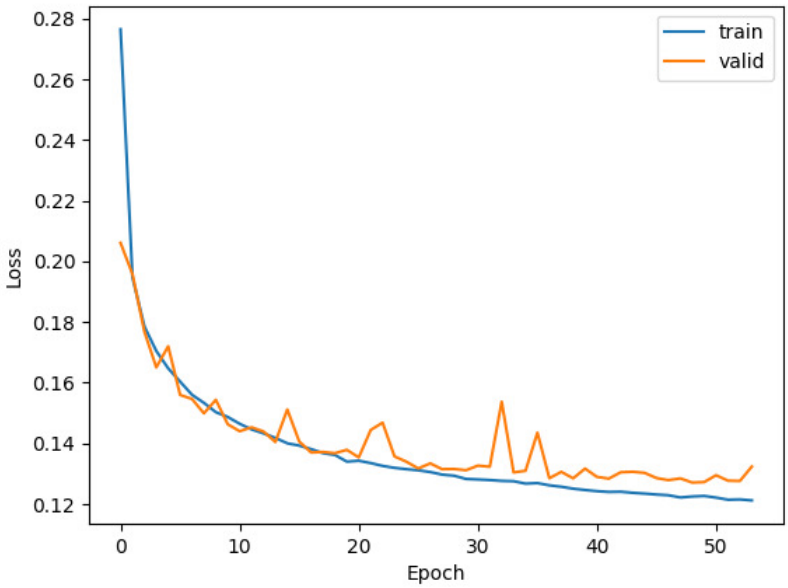

FIGURE 6.6: The cross-entropy loss as a function of the training time (epoch) during the training of the ANN for the WZ VBF selection.

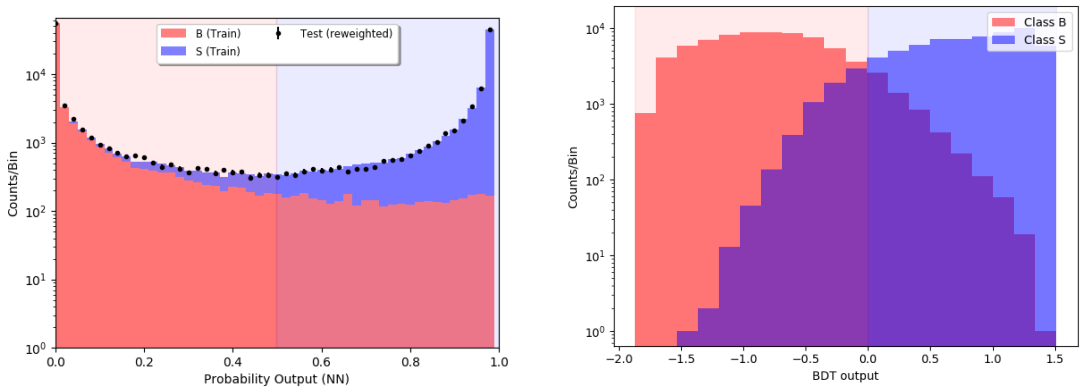

(a) (b)

FIGURE 6.7: In figure (a) the ANN output variable for signal and background training events (stacked) with the validation set overlaid as black points. A typical cut would be applied at around 0.5 to separate background and signal events, with both regions shaded either blue (signal) and red (background). Figure (b) shows the BDT output variable for signal and background training events.

the SM WZ background as a function of the cut value is shown in figure 6.8, (a) for the ANN model and (b) for the BDT model. The maximum in the validation curve indicates the optimal cut value for both models.

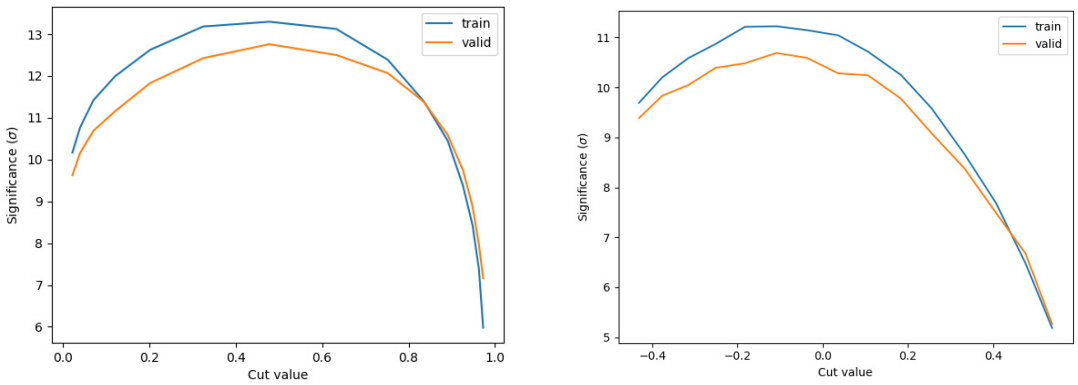

(a) (b)

FIGURE 6.8: Approximated significance using equation 6.7 as a function of the ANN model in (a) and for the BDT model in (b).

Using the sample approximate significance formula as before we can calculate an approximate significance using the ANN and the VBF cut selection that was used in the published paper ($m_{jj} > 500$ GeV and $|\Delta\eta_{jj}| < 3.5$). Some preliminary results using some of the GM signal mass points are shown in table 6.III to illustrate how this method helps to significantly reduce the background contribution and improve the sensitivity. For this comparison, the cut on the ANN output variable is chosen so that the number of signal events is comparable to the number of events observed with the cut selection. The samples are normalised to 140 fb^{-1} and the parameter $\sin\theta_H$ is set to 0.25, for the background only the Standard Model (SM) WZ contribution is considered. The results were obtained with the best performing ANN where the choice of hyperparameters was obtained using some 20 trainings with the random search optimisation technique described above. An overview of the hyperparameters that obtained the highest significance are detailed in table 6.IV.

$H_5^\pm$ Mass [GeV]	200	200	900	900
Selection	VBF cuts	ANN	VBF cuts	ANN
Number of signal events	13.9	14.0	2.98	2.76
Number of background events	121.5	32.0	7.88	2.41
Approximate significance	1.24	2.33	1.00	1.54

TABLE 6.III: Preliminary comparison of the number of signal and background events as well as the approximate significance obtained with these numbers between the VBF cut selection and the ANN for two mass points of the GM model. Samples are normalised to 140 fb^{-1}.

Number of hidden layers	2
Number of neurons per layer	300
Learning rate	0.013
Dropout probability	0.24
Patience (early stopping)	18
Nesterov momentum	0.6

TABLE 6.IV: Overview of the hyperparameters used in the best performing ANN model for the VBF event selection.

6.2 GM NLO signal sample production

To improve upon the signal samples used in the published analysis, new signal models for the GM $H_5^\pm$ signal models at NLO were requested. The GMCALC [100] v.1.3.0 is used to produce the NLO parameter cards in conjunction with the NLO model file available from [142]. The Monte Carlo generator MADGRAPH+PYTHIA 8 is used for the production. Since a much higher sensitivity is expected for the full run-2 analysis, the signal samples are extended up to a mass of 2 TeV. Since this sample contains taus decaying also hadronically, loose lepton filter is applied after showering requiring at least three leptons within a pseudorapidity range of $|\eta| < 2.7$ and with a minimum transverse momentum of $p_\text{T} > 3.5$ GeV. As for the previous samples, the parameter $\sin\theta_H$ was set to 0.5 for lower masses below 900 GeV and 0.25 for masses above in order to pass theoretical

constraints. A list of the requested mass points, cross section and filter efficiencies is shown in table 6.V.

$H_5^{\pm}$ Mass	Number of events	$\sin\theta_H$	Cross-section [fb]	Filter efficiency
200	120.000	0.5	24.5	44.4
250	120.000	0.5	17.4	44.9
300	120.000	0.5	13.4	46.0
350	120.000	0.5	10.4	47.8
400	120.000	0.5	8.24	48.7
450	120.000	0.5	6.30	49.3
500	120.000	0.5	5.34	50.1
600	120.000	0.5	3.70	50.7
700	120.000	0.5	2.40	52.1
800	120.000	0.5	1.76	53.1
900	120.000	0.25	0.317	51.6
1000	120.000	0.25	0.222	53.6
1200	120.000	0.25	0.1197	52.4
1400	120.000	0.25	0.0842	53.1
1600	120.000	0.25	0.0439	52.2
1800	120.000	0.25	0.0286	53.6
2000	120.000	0.25	0.0154	54.6

TABLE 6.V: Overview of the GM signal samples to be produced at NLO.

Figure 6.9 shows a comparison of some of the jet kinematics of the GM $H_5^{\pm}$ 500 GeV mass point generated at LO and at NLO. Both are compared in the same fiducial region. The distributions are very similar but some small differences can be observed in the predictions, which can be due to the presence of softer additional jets that are produced at NLO.

6.3 Fat-electron selection

As mentioned above the highly boosted resonances with very large masses will result in highly boosted $Z \to ee$ decays that are reconstructed with low efficiency. Chloé

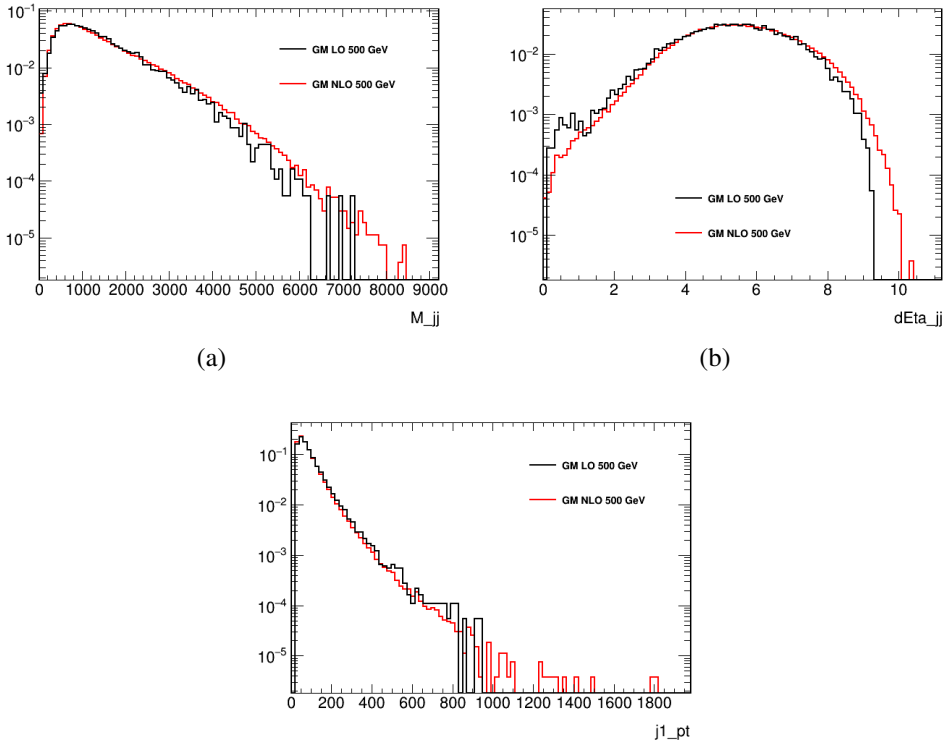

(a) (b)

(c)

FIGURE 6.9: Comparison of jet kinematic distribution of GM $H_5^{\pm}$ 500 GeV samples produced at LO and NLO. (a) shows the invariant mass of the dijet system M_{jj}, (b) shows the pseudorapidity separation of the two jets $\Delta\eta_{jj}$ and (c) shows the p_{T} distribution of one of the VBS jets.

Lefebvre, a current student of the UdeM ATLAS group is therefore developing a new selection algorithm in this high mass region. With the current selection criteria, the two electrons of the Z decay are reconstructed as a single object. The new method exploits the jet sub-structure, to identify these events. A BDT method is implemented using AdaBoost, as for the VBF signal selection. Inputs are the jet kinematics, its p_{T} , η and ϕ, the invariant mass of the jets as well as the number of tracks measured in the tracks and the electromagnetic fraction. A simulated HVT W' with a resonance mass of 4 TeV is for the training, the signals are selected jets of $Z \rightarrow ee$ and the background are all other jets in the same sample.

CHAPITRE 7

CONCLUSION AND OUTLOOK

This thesis describes the search for resonant WZ in the fully leptonic final state with the ATLAS detector. A short overview of relevant aspects of the Standard Model (SM) is presented. Several theoretical problems are highlighted, for example the fine tuning problem of the Higgs boson. One of the theoretically well-motivated extensions of the SM is presented in more detail, the composite Higgs models. These models try to address some of the problems of the SM, especially the above-mentioned fine tuning problem, by enlarging the symmetry group and describing the Higgs as a bound state of a new strongly interacting sector. In contrast to the SM, it is now the strong sector which causes symmetry breaking. A large variety of composite Higgs models exists. As an example, the Minimal Composite Higgs Model (MCHM) is presented. In the MCHM, the Higgs boson is a pseudo-Goldstone boson, which is protected from loop correction, thus solving the hierarchy problem. As a result of an extended symmetry, additional vector resonances are added to the SM. To test the model, it is essential to look for these resonances, especially as the lowest mass states should be accessible by the Large Hadron Collider. Two benchmark models are presented predicting scalar and vector resonances which decay to WZ, the phenomenological Heavy Vector Triplet (HVT) model predicting heavy vector resonances W' and the Georgi-Machacek (GM) model predicting charged Higgs $H_5^{\pm}$.

A short overview of the accelerator and ATLAS detector is given describing how the various particles produced in proton-proton collisions are measured by the detector. By combining the various measurements of all parts of the detector, searches for new resonances can be performed. An important process in the SM, the Vector Boson Scattering (VBS) is presented. Studies of VBS processes are an important tool to test properties of the Higgs boson since in the SM, it is the Higgs boson that restores unitarity in the VBS scattering amplitudes. Additionally, this process has a very clean experimental signature and is therefore an ideal candidate to look for new resonances as predicted by the com-

posite Higgs models. If for some reason the additional resonances do not couple to SM fermions, VBS searches will be the most sensitive ones.

Finally an analysis is presented searching for resonant WZ production in fully leptonic final states (electrons and muons) using 36.1 fb^{-1} of $\sqrt{s} = 13$ TeV pp data collected by the ATLAS experiment at the Large Hadron Collider (LHC) during the 2015 and 2016 run periods. This is an experimentally very clean channel which could provide better limits at low masses than the semi-leptonic one despite the lower production rate. Two different production modes are considered using quark–antiquark annihilation and vector-boson fusion. The data in the $q\bar{q}$ fusion category are found to be consistent with Standard Model predictions. The results are used to derive upper limits at 95% CL on the cross section times branching ratio of the HVT Model A (Model B) as a function of the resonance mass, with no evidence of heavy resonance production for masses below 2260 (2460) GeV.

In the case of the Vector Boson Fusion (VBF) production processes, limits on the production cross section times branching ratio are obtained as a function of the mass of a charged member of a heavy vector triplet or the fiveplet scalar in the GM model. The results show a local excess of events over the Standard Model expectations at a resonance mass of around 450 GeV. The local significances for signals of $H_5^{\pm}$ and of a heavy vector W' boson are 2.9 and 3.1 standard deviations respectively. The respective global significances calculated considering the Look Elsewhere effect are 1.6 and 1.9 standard deviations respectively.

7.1 Possible Improvements

Several possible improvements to the analysis are discussed in Chapter 6, the full run-2 analysis will feature a VBF Multivariate Analysis (MVA) selection, replacing the simple cut-based analysis used in the published paper. The new selection will greatly improve the signal acceptance times efficiency while reducing the background contamination of the signal region. A greatly improved sensitivity to the benchmark models is therefore expected. To improve the signal samples, new Next-to-leading order (NLO) signal samples will be produced for the GM model.

Further improvement is also expected by including a *fat*-electron selection. An algorithm will specifically target boosted $Z \rightarrow ee$ decays. In the published analysis, a decrease in acceptance for these boosted electrons was observed, as they no longer pass the isolation cuts for electrons.

7.2 Outlook

The full run-2 analysis will allow to either reject or confirm the small excess observed in the published analysis. Many improvements in the analysis and the greatly increased integrated luminosity available, will allow to substantially improve the current exclusion limits if no sign of a signal is found.

BIBLIOGRAPHIE

[1] ATLAS collaboration, *A neural network clustering algorithm for the ATLAS silicon pixel detector*, *JINST* **9** (2014) P09009 [1406.7690].

[2] ATLAS collaboration, *Training and validation of the ATLAS pixel clustering neural networks*, Tech. Rep. ATL-PHYS-PUB-2018-002, CERN, Geneva, Mar, 2018.

[3] B. Freund, *Search for resonant WZ Production in the fully leptonic final state in Proton-Proton Collisions at* $\sqrt{s} = 13$ *TeV with the ATLAS Detector*, *PoS* **LHCP2018** (2018) 008.

[4] ATLAS Collaboration, *Observation of a new particle in the search for the Standard Model Higgs boson with the ATLAS detector at the LHC*, *Physics Letters B* **716** (2012) 1 .

[5] CMS Collabotarion, *Observation of a new boson at a mass of 125 GeV with the CMS experiment at the LHC*, *Physics Letters B* **716** (2012) 30 .

[6] S. L. Glashow, *Partial-symmetries of weak interactions*, *Nuclear Physics* **22** (1961) 579 .

[7] A. Salam, *Weak and Electromagnetic Interactions*, *Conf. Proc.* **C680519** (1968) 367.

[8] S. Weinberg, *A model of leptons*, *Phys. Rev. Lett.* **19** (1967) 1264.

[9] C. Burgess and G. Moore, *The Standard Model : A Primer*, *Cambridge University Press* (2013) .

[10] G. Hooft, *Renormalizable Lagrangians for massive Yang-Mills fields*, *Nuclear Physics B* **35** (1971) 167 .

[11] W. Commons, "File :Standard Model of Elementary Particles.svg — Wikimedia Commons, the free media repository." https://commons.wikimedia.org/w/index.php?title=File:Standard_Model_of_Elementary_Particles.svg&oldid=341423479, [Online; accessed 26-April-2019].

[12] J. M. Ramos, *WZ diboson measurements with the ATLAS experiment at the LHC and Performance of resistive Micromegas in view of HL-LHC applications*, *CERN-THESIS-2013-199* (2013) .

[13] NNPDF collaboration, *Parton distributions from high-precision collider data*, *Eur. Phys. J. C* **77** (2017) 663 [1706.00428].

[14] T. Aoyama, M. Hayakawa, T. Kinoshita and M. Nio, *Tenth-Order QED Contribution to the Electron $g-2$ and an Improved Value of the Fine Structure Constant*, *Phys. Rev. Lett.* **109** (2012) 111807.

[15] C. N. Yang and R. L. Mills, *Conservation of Isotopic Spin and Isotopic Gauge Invariance*, *Phys. Rev.* **96** (1954) 191.

[16] S. L. Glashow, *Partial Symmetries of Weak Interactions*, *Nucl. Phys.* **22** (1961) 579.

[17] J. Goldstone, A. Salam and S. Weinberg, *Broken Symmetries*, *Phys. Rev.* **127** (1962) 965.

[18] K. A. Olive et al. (Particle Data Group), *The Review of Particle Physics*, *Chin. Phys. C* **38, 090001** (2014) .

[19] L. Álvarez-Gaumé and J. Ellis, *Eyes on a prize particle*, *Nature Physics* **7** (2010) 2 EP .

[20] ALEPH, DELPHI, L3, OPAL, SLD, LEP Electroweak Working Group, SLD Electroweak Group, SLD Heavy Flavour Group collaboration, *Precision*

electroweak measurements on the Z resonance, *Phys. Rept.* **427** (2006) 257 [hep-ex/0509008].

[21] D. R. Green, P. Meade and M.-A. Pleier, *Multiboson interactions at the LHC*, *Rev. Mod. Phys.* **89** (2017) 035008 [1610.07572].

[22] R. Contino, *The Higgs as a Composite Nambu-Goldstone Boson*, in *Physics of the large and the small, TASI 09, proceedings of the Theoretical Advanced Study Institute in Elementary Particle Physics, Boulder, Colorado, USA, 1-26 June 2009*, pp. 235–306, 2011, 1005.4269, DOI.

[23] M. Gonzalez-Garcia and M. Maltoni, *Phenomenology with massive neutrinos*, *Physics Reports* **460** (2008) 1 .

[24] A. Wulzer, *Behind the Standard Model*, in *Proceedings, 2015 European School of High-Energy Physics (ESHEP2015) : Bansko, Bulgaria, September 02 - 15, 2015*, 2019, 1901.01017.

[25] G. Hinshaw, D. Larson, E. Komatsu, D. N. Spergel, C. L. Bennett, J. Dunkley et al., *NINE-YEARWILKINSON MICROWAVE ANISOTROPY PROBE(WMAP) OBSERVATIONS : COSMOLOGICAL PARAMETER RESULTS*, *The Astrophysical Journal Supplement Series* **208** (2013) 19.

[26] Planck collaboration, *Planck 2018 results. VI. Cosmological parameters*, 1807.06209.

[27] P. Langacker and M. Luo, *Implications of precision electroweak experiments for m_t, ρ_0, $sin^2\theta_W$, and grand unification*, *Phys. Rev. D* **44** (1991) 817.

[28] ATLAS collaboration, *Measurement of the Higgs boson mass in the $H \to ZZ^* \to 4\ell$ and $H \to \gamma\gamma$ channels with $\sqrt{s} = 13$ TeV pp collisions using the ATLAS detector*, *Phys. Lett. B* **784** (2018) 345 [1806.00242].

[29] M. C. Brak, *The Hierarchy Problem in the Standard Model and Little Higgs Theories*, *Master Thesis* (2004) .

[30] L. J. Hall and M. Suzuki, *Explicit R-Parity Breaking in Supersymmetric Models*, *Nucl. Phys. B* **231** (1984) 419.

[31] K. Lane and S. Mrenna, *The Collider Phenomenology of Technihadrons in the Technicolor Straw Man Model*, *Phys. Rev. D* **67** (2003) 115011 [hep-ph/0210299].

[32] M. Bona et al., *Model-independent constraints on $\Delta F = 2$ operators and the scale of new physics*, *JHEP* **2008** (2008) 049.

[33] B. Holdom, *Techniodor*, *Physics Letters B* **150** (1985) 301 .

[34] K. Yamawaki, M. Bando and K.-i. Matumoto, *Scale-Invariant Hypercolor Model and a Dilaton*, *Phys. Rev. Lett.* **56** (1986) 1335.

[35] G. F. Giudice, C. Grojean, A. Pomarol and R. Rattazzi, *The Strongly-Interacting Light Higgs*, *JHEP* **06** (2007) 045 [hep-ph/0703164].

[36] G. Panico and A. Wulzer, *The Composite Nambu-Goldstone Higgs*, *Lect. Notes Phys.* **913** (2016) pp.1 [1506.01961].

[37] K. Agashe, R. Contino and A. Pomarol, *The minimal composite Higgs model*, *Nuclear Physics B* **719** (2005) 165 .

[38] N. Arkani-Hamed, A. G. Cohen, E. Katz and A. E. Nelson, *The Littlest Higgs*, *JHEP* **07** (2002) 034 [hep-ph/0206021].

[39] D. E. Kaplan and M. Schmaltz, *The Little Higgs from a simple group*, *JHEP* **10** (2003) 039 [hep-ph/0302049].

[40] B. Bellazzini, C. Csáki and J. Serra, *Composite Higgses*, *Eur. Phys. J.* **C74** (2014) 2766 [1401.2457].

[41] B. Bellazzini, C. Csáki, J. Hubisz, J. Serra and J. Terning, *Composite Higgs sketch*, *JHEP* **2012** (2012) 3.

[42] D. Pappadopulo, A. Thamm, R. Torre and A. Wulzer, *Heavy vector triplets : bridging theory and data*, *JHEP* **2014** (2014) 60.

[43] S. P. Martin, *A Supersymmetry primer*, hep-ph/9709356.

[44] H. Georgi and M. Machacek, *Doubly charged Higgs bosons*, *Nuclear Physics B* **262** (1985) 463 .

[45] M. Einhorn, D. Jones and M. Veltman, *Heavy particles and the ρ parameter in the standard model*, *Nuclear Physics B* **191** (1981) 146 .

[46] C. Degrande, K. Hartling, H. E. Logan, A. D. Peterson and M. Zaro, *Automatic predictions in the Georgi-Machacek model at next-to-leading order accuracy*, *Phys. Rev. D* **93** (2016) 035004 [1512.01243].

[47] K. Hartling, K. Kumar and H. E. Logan, *The decoupling limit in the Georgi-Machacek model*, *Phys. Rev. D* **90** (2014) 015007.

[48] K. Hartling, K. Kumar and H. E. Logan, *Indirect constraints on the Georgi-Machacek model and implications for Higgs boson couplings*, *Phys. Rev. D* **91** (2015) 015013.

[49] H. E. Logan and M. B. Reimer, *Characterizing a benchmark scenario for heavy Higgs boson searches in the Georgi-Machacek model*, *Phys. Rev. D* **96** (2017) 095029.

[50] CMS collaboration, *Study of Vector Boson Scattering and Search for New Physics in Events with Two Same-Sign Leptons and Two Jets*, *Phys. Rev. Lett.* **114** (2015) 051801.

[51] R. Voss and A. Breskin, eds., *The CERN Large Hadron Collider, accelerator and experiments*. Geneva : CERN, 2009.

[52] CERN image, *available from* http://maalpu.org/lhc/images/LHC.images.htm, date retrieved (2016).

[53] CERN, *Incident in LHC sector 3-4* https://home.cern/news/press-release/cern/incident-lhc-sector-3-4, date retrieved (2019).

[54] ATLAS Collaboration, "Luminosity Public Results." https://twiki.cern.ch/twiki/bin/view/AtlasPublic/LuminosityPublicResultsRun2, date retrieved (2019).

[55] ATLAS Collaboration, *The ATLAS experiment at the CERN large hadron collider*, *Journal of Instrumentation* **3** (2008) S08003.

[56] A. Miucci, *The ATLAS insertable b-layer project*, *Journal of Instrumentation* **9** (2014) C02018.

[57] K. Potamianos, *The upgraded Pixel detector and the commissioning of the Inner Detector tracking of the ATLAS experiment for Run-2 at the Large Hadron Collider*, *PoS* **EPS-HEP2015** (2015) 261 [1608.07850].

[58] I. Bird, *Computing for the Large Hadron Collider*, *Annual Review of Nuclear and Particle Science* **61** (2011) 99 [https://doi.org/10.1146/annurev-nucl-102010-130059].

[59] e. a. Aderholz, Michael, *Models of Networked Analysis at Regional Centres for LHC Experiments (MONARC), Phase 2 Report, 24th March 2000*, Tech. Rep. CERN-LCB-2000-001. KEK-2000-8, CERN, Geneva, Apr, 2000.

[60] ATLAS Collaboration, "Electron efficiency measurements with the ATLAS detector using the 2015 LHC proton-proton collision data." ATLAS-CONF-2016-024, 2016.

[61] ATLAS Collaboration, *Muon reconstruction performance of the ATLAS detector in proton–proton collision data at* $\sqrt{s} = 13$ *TeV*, *Eur. Phys. J. C* **76** (2016) 292 [1603.05598].

[62] G. C. Blazey et al., *Run II jet physics*, in *QCD and weak boson physics in Run II. Proceedings, Batavia, USA, March 4-6, June 3-4, November 4-6, 1999*, pp. 47–77, 2000, hep-ex/0005012, http://lss.fnal.gov/cgi-bin/find_paper.pl?conf-00-092.

[63] S. Catani, Y. L. Dokshitzer, M. H. Seymour and B. R. Webber, *Longitudinally invariant K_t clustering algorithms for hadron hadron collisions*, *Nucl. Phys. B* **406** (1993) 187.

[64] M. Wobisch and T. Wengler, *Hadronization corrections to jet cross-sections in deep inelastic scattering*, in *Monte Carlo generators for HERA physics. Proceedings, Workshop, Hamburg, Germany, 1998-1999*, pp. 270–279, 1998, hep-ph/9907280.

[65] Y. L. Dokshitzer, G. D. Leder, S. Moretti and B. R. Webber, *Better jet clustering algorithms*, *JHEP* **08** (1997) 001 [hep-ph/9707323].

[66] M. Cacciari, G. P. Salam and G. Soyez, *The anti-k_t jet clustering algorithm*, *JHEP* **04** (2008) 063 [0802.1189].

[67] ATLAS collaboration, "Performance of missing transverse momentum reconstruction with the ATLAS detector in the first proton–proton collisions at $\sqrt{s}$ = 13 TeV." ATL-PHYS-PUB-2015-027, 2015.

[68] ATLAS collaboration, *Performance of missing transverse momentum reconstruction with the ATLAS detector using proton-proton collisions at $\sqrt{s}$ = 13 TeV*, *Eur. Phys. J. C* **78** (2018) 903 [1802.08168].

[69] CERN, "HL-LHC Project Schedule." https://project-hl-lhc-industry.web.cern.ch/content/project-schedule, date retrieved (2019).

[70] ATLAS Collaboration, *Letter of Intent for the Phase-I Upgrade of the ATLAS Experiment*, Tech. Rep. CERN-LHCC-2011-012. LHCC-I-020, CERN, Geneva, Nov, 2011.

[71] S. Majewski, G. Charpak, A. Breskin and G. Mikenberg, *A thin multiwire chamber operating in the high multiplication mode*, *Nuclear Instruments and Methods in Physics Research* **217** (1983) 265 .

[72] Y. Giomataris, P. Rebourgeard, J. Robert and G. Charpak, *Micromegas : a high-granularity position-sensitive gaseous detector for high particle-flux environments*, *Nuclear Instruments and Methods in Physics Research Section A: Accelerators, Spectrometers, Detectors and Associated Equipment* **376** (1996) 29 .

[73] ATLAS Collaboration, *Technical Design Report for the ATLAS Inner Tracker Strip Detector*, Tech. Rep. CERN-LHCC-2017-005. ATLAS-TDR-025, CERN, Geneva, Apr, 2017.

[74] R. Frühwirth, *Application of kalman filtering to track and vertex fitting*, *Nuclear Instruments and Methods in Physics Research Section A: Accelerators, Spectrometers, Detectors and Associated Equipment* **262** (1987) 444 .

[75] *The Optimization of ATLAS Track Reconstruction in Dense Environments*, Tech. Rep. ATL-PHYS-PUB-2015-006, CERN, Geneva, Mar, 2015.

[76] ATLAS collaboration, *Search for WZ resonances in the fully leptonic channel using pp collisions at $\sqrt{s} = 8$ TeV with the ATLAS detector*, *Phys. Lett. B* **737** (2014) 223 [1406.4456].

[77] ATLAS collaboration, *Combination of searches for heavy resonances decaying into bosonic and leptonic final states using 36 fb^{-1} of proton-proton collision data at $\sqrt{s} = 13$ TeV with the ATLAS detector - Auxiliary figure*, .

[78] ATLAS collaboration, *Search for new high-mass phenomena in the dilepton final state using 36 fb^{-1} of proton-proton collision data at $\sqrt{s} = 13$ TeV with the ATLAS detector*, *JHEP* **2017** (2017) 182.

[79] ATLAS collaboration, *Search for a new heavy gauge-boson resonance decaying into a lepton and missing transverse momentum in 36^{-1} of pp collisions at $\sqrt{s}$ = 13 TeV with the ATLAS experiment*, *Eur. Phys. J. C* **78** (2018) 401.

[80] ATLAS collaboration, *Search for High-Mass Resonances Decaying to $\tau\nu$ in pp Collisions at $\sqrt{s}$ = 13 TeV with the ATLAS Detector*, *Phys. Rev. Lett.* **120** (2018) 161802.

[81] CMS collaboration, *Search for high-mass resonances in final states with a lepton and missing transverse momentum at $\sqrt{s}$ = 13 TeV*, *JHEP* **2018** (2018) 128.

[82] CMS collaboration, *Search for a W′ boson decaying to a τ lepton and a neutrino in proton-proton collisions at $\sqrt{s}$ = 13 TeV*, *Phys. Lett. B* **792** (2019) 107 [1807.11421].

[83] ATLAS collaboration, *Search for new phenomena in dijet events using* 37 fb^{-1} *of pp collision data collected at $\sqrt{s}$ = 13 TeV with the atlas detector*, *Phys. Rev. D* **96** (2017) 052004.

[84] CMS collaboration, *Search for dijet resonances in proton-proton collisions at $\sqrt{s}$ = 13 TeV and constraints on dark matter and other models*, *Physics Letters B* **769** (2017) 520 .

[85] ATLAS collaboration, *Searches for heavy diboson resonances in pp collisions at $\sqrt{s}$ = 13 TeV with the ATLAS detector*, *JHEP* **09** (2016) 173 [1606.04833].

[86] CMS collaboration, *Search for massive resonances decaying into WW, WZ or ZZ bosons in proton-proton collisions at $\sqrt{s}$ = 13 TeV*, *JHEP* **2017** (2017) 162.

[87] V. Khachatryan et al., *Search for new resonances decaying via WZ to leptons in proton-proton collisions at $\sqrt{s}$=8TeV*, *Physics Letters B* **740** (2015) 83 .

[88] CMS collaboration, *Observation of Electroweak Production of Same-Sign W Boson Pairs in the Two Jet and Two Same-Sign Lepton Final State in Proton-Proton Collisions at $\sqrt{s}$ = 13 TeV*, *Phys. Rev. Lett.* **120** (2018) 081801.

[89] CMS collaboration, *Measurement of electroweak WZ boson production and search for new physics in WZ + two jets events in pp collisions at* $\sqrt{s}$ *= 13 TeV*, 1901.04060.

[90] ATLAS collaboration, *Search for heavy resonances decaying into WW in the* $e\nu\mu\nu$ *final state in pp collisions at* $\sqrt{s}$ = 13 *TeV with the ATLAS detector*, *Eur. Phys. J. C* **78** (2018) 24.

[91] GEANT4 collaboration, *GEANT4 : A simulation toolkit*, *Nucl. Instrum. Meth. A* **506** (2003) 250.

[92] ATLAS collaboration, "The simulation principle and performance of the ATLAS fast calorimeter simulation FastCaloSim." ATL-PHYS-PUB-2010-013, 2010.

[93] T. Gleisberg, S. Hoeche, F. Krauss, M. Schonherr, S. Schumann, F. Siegert et al., *Event generation with SHERPA 1.1*, *JHEP* **02** (2009) 007 [0811.4622].

[94] S. Alioli, P. Nason, C. Oleari and E. Re, *A general framework for implementing NLO calculations in shower Monte Carlo programs : the POWHEG BOX*, *JHEP* **2010** (2010) 43.

[95] M. Bähr, S. Gieseke, M. A. Gigg, D. Grellscheid, K. Hamilton, O. Latunde-Dada et al., *Herwig++ physics and manual*, *Eur. Phys. J. C* **58** (2008) 639.

[96] T. Sjöstrand, S. Mrenna and P. Z. Skands, *A brief introduction to PYTHIA 8.1*, *Comput. Phys. Commun.* **178** (2008) 852 [0710.3820].

[97] M. Brucherseifer, F. Caola and K. Melnikov, *On the NNLO QCD corrections to single-top production at the LHC*, *Phys. Lett. B* **736** (2014) 58 [1404.7116].

[98] LHC Higgs Cross Section Working Group collaboration, *Handbook of LHC Higgs Cross Sections : 4. Deciphering the Nature of the Higgs Sector*, 1610.07922.

[99] C. Anastasiou, L. J. Dixon, K. Melnikov and F. Petriello, *High precision QCD at hadron colliders : Electroweak gauge boson rapidity distributions at NNLO*, *Phys. Rev.* **D69** (2004) 094008 [hep-ph/0312266].

[100] K. Hartling, K. Kumar and H. E. Logan, *GMCALC : a calculator for the Georgi-Machacek model*, 1412.7387.

[101] LHC Higgs Cross Section Working Group collaboration, *Handbook of LHC Higgs Cross Sections : 4. Deciphering the nature of the Higgs sector*, 1610.07922.

[102] ATLAS Collaboration, *Jet energy measurement with the ATLAS detector in proton–proton collisions at* $\sqrt{s}$ = 7 *TeV*, *Eur. Phys. J. C* **73** (2013) 2304 [1112.6426].

[103] ATLAS collaboration, "Tagging and suppression of pileup jets with the ATLAS detector." ATLAS-CONF-2014-018, 2014.

[104] ATLAS collaboration, "Jet Calibration and Systematic Uncertainties for Jets Reconstructed in the ATLAS Detector at $\sqrt{s}$ = 13 TeV." ATL-PHYS-PUB-2015-015, 2015.

[105] ATLAS Collaboration, *Performance of b-jet identification in the ATLAS experiment*, *Journal of Instrumentation* **11** (2016) P04008.

[106] ATLAS Collaboration, *Optimisation of the ATLAS b-tagging performance for the 2016 LHC Run*, Tech. Rep. ATL-PHYS-PUB-2016-012, CERN, Geneva, Jun, 2016.

[107] ATLAS collaboration, *Measurements of b-jet tagging efficiency with the ATLAS detector using* $t\bar{t}$ *events at* $\sqrt{s}$ = 13 *TeV*, *JHEP* **2018** (2018) 89.

[108] A. Buckley, J. Ferrando, S. Lloyd, K. Nordström, B. Page, M. Rüfenacht et al., *LHAPDF6 : parton density access in the LHC precision era*, *Eur. Phys. J. C* **75** (2015) 132.

[109] NNPDF collaboration, *Parton distributions for the LHC Run II*, *JHEP* **04** (2015) 040 [1410.8849].

[110] S. Kretzer, H. L. Lai, F. I. Olness and W. K. Tung, *CTEQ6 parton distributions with heavy quark mass effects*, *Phys. Rev. D* **69** (2004) 114005.

[111] A. D. Martin, W. J. Stirling, R. S. Thorne and G. Watt, *Parton distributions for the LHC*, *Eur. Phys. J.* **C63** (2009) 189 [0901.0002].

[112] ATLAS collaboration, *Luminosity determination in pp collisions at* $\sqrt{s} = 8$ *TeV using the ATLAS detector at the LHC*, *Eur. Phys. J.* **C76** (2016) 653 [1608.03953].

[113] S. van der Meer, *Calibration of the effective beam height in the ISR*, Tech. Rep. CERN-ISR-PO-68-31. ISR-PO-68-31, CERN, Geneva, 1968.

[114] G. Cowan, K. Cranmer, E. Gross and O. Vitells, *Asymptotic formulae for likelihood-based tests of new physics*, *Eur. Phys. J. C* **71** (2011) 1554.

[115] Particle Data Group collaboration, *Review of particle physics*, *Phys. Rev. D* **98** (2018) 030001.

[116] A. Wald, *Tests of statistical hypotheses concerning several parameters when the number of observations is large*, *Transactions of the American Mathematical Society* **54** (1943) 426.

[117] L. Moneta, K. Cranmer, G. Schott and W. Verkerke, *The RooStats project*, in *Proceedings of the 13th International Workshop on Advanced Computing and Analysis Techniques in Physics Research. February 22-27*, p. 57, Jan, 2010, 1009.1003.

[118] A. L. Read, *Presentation of search results : the* CL_s *technique*, *Journal of Physics G: Nuclear and Particle Physics* **28** (2002) 2693.

[119] The ATLAS Collaboration, The CMS Collaboration, The LHC Higgs Combination Group, *Procedure for the LHC Higgs boson search combination in Summer 2011*, Tech. Rep. CMS-NOTE-2011-005. ATL-PHYS-PUB-2011-11, CERN, Geneva, Aug, 2011.

[120] ATLAS collaboration, *Combination of searches for heavy resonances decaying into bosonic and leptonic final states using* 36 fb^{-1} *of proton-proton collision data at* $\sqrt{s} = 13$ TeV *with the ATLAS detector*, *Phys. Rev. D* **98** (2018) 052008.

[121] F. del Aguila, J. de Blas and M. Pérez-Victoria, *Electroweak limits on general new vector bosons*, *JHEP* **2010** (2010) 33.

[122] ATLAS collaboration, *Combination of searches for heavy resonances decaying into bosonic and leptonic final states using 36* fb^{-1} *of proton-proton collision data at* $\sqrt{s} = 13$ *TeV with the ATLAS detector*, *Phys. Rev. D* **98** (2018) 052008 [1808.02380].

[123] I. Goodfellow, Y. Bengio and A. Courville, *Deep Learning*. MIT Press, 2016.

[124] W. S. McCulloch and W. Pitts, *A logical calculus of the ideas immanent in nervous activity*, *The bulletin of mathematical biophysics* **5** (1943) 115.

[125] F. Rosenblatt, *The perceptron : A probabilistic model for information storage and organization in the brain*, *Psychological Review* (1958) 65.

[126] P. E. Rauber, S. Fadel, A. Falcao and A. Telea, *Visualizing the hidden activity of artificial neural networks*, *IEEE Transactions on Visualization and Computer Graphics* **23** (2016) 1.

[127] G. E. Hinton, S. Osindero and Y.-W. Teh, *A Fast Learning Algorithm for Deep Belief Nets*, *Neural Computation* **18** (2006) 1527 [https://doi.org/10.1162/neco.2006.18.7.1527].

[128] Y. Freund and R. E. Schapire, *Experiments with a new boosting algorithm*, in *Proceedings of the Thirteenth International Conference on International*

Conference on Machine Learning, ICML'96, (San Francisco, CA, USA), pp. 148–156, Morgan Kaufmann Publishers Inc., 1996, http://dl.acm.org/citation.cfm?id=3091696.3091715.

[129] B. P. Roe, H.-J. Yang, J. Zhu, Y. Liu, I. Stancu and G. McGregor, *Boosted decision trees as an alternative to artificial neural networks for particle identification*, *Nuclear Instruments and Methods in Physics Research Section A: Accelerators, Spectrometers, Detectors and Associated Equipment* **543** (2005) 577 .

[130] A. Hocker et al., *TMVA - Toolkit for Multivariate Data Analysis*, physics/0703039.

[131] ATLAS collaboration, *Observation of electroweak $W^{\pm}Z$ boson pair production in association with two jets in pp collisions at $\sqrt{s}$ = 13 TeV with the ATLAS detector*, *Submitted to : Phys. Lett.* (2018) [1812.09740].

[132] P. Baldi, K. Cranmer, T. Faucett, P. Sadowski and D. Whiteson, *Parameterized neural networks for high-energy physics*, *Eur. Phys. J. C* **76** (2016) 235.

[133] F. Chollet et al., "Keras." https://keras.io, 2015.

[134] M. Abadi et al., "TensorFlow : Large-scale machine learning on heterogeneous systems." https://www.tensorflow.org/, 2015.

[135] V. Nair and G. E. Hinton, *Rectified Linear Units Improve Restricted Boltzmann Machines*, in *Proceedings of the 27th International Conference on International Conference on Machine Learning*, ICML'10, (USA), pp. 807–814, Omnipress, 2010, http://dl.acm.org/citation.cfm?id=3104322.3104425.

[136] H. Robbins and S. Monro, *A stochastic approximation method*, *Ann. Math. Statist.* **22** (1951) 400.

[137] L. Bottou, *Large-scale machine learning with stochastic gradient descent*, in *Proceedings of COMPSTAT'2010*, Y. Lechevallier and G. Saporta, eds., (Heidelberg), pp. 177–186, Physica-Verlag HD, 2010.

[138] I. Sutskever, J. Martens, G. Dahl and G. Hinton, *On the importance of initialization and momentum in deep learning*, in *International conference on machine learning*, pp. 1139–1147, 2013.

[139] R. K. Srivastava, K. Greff and J. Schmidhuber, *Highway Networks*, *arXiv e-prints* (2015) [1505.00387].

[140] J. Bergstra and Y. Bengio, *Random search for hyper-parameter optimization*, *Journal of Machine Learning Research* **13** (2012) 281.

[141] F. Pedregosa, G. Varoquaux, A. Gramfort, V. Michel, B. Thirion, O. Grisel et al., *Scikit-learn : Machine learning in Python*, *Journal of Machine Learning Research* **12** (2011) 2825.

[142] "GM Model files." https://feynrules.irmp.ucl.ac.be/wiki/GeorgiMachacekModel, [Online; accessed 29-April-2019].

Annexe I

Data and signal samples

Information about the $q\bar{q}$ signal samples is summarised in Table I.I. Information about the VBF HVT signal samples is summarised in Table I.II. A generator cut of $m_{jj} > 150$ GeV was applied on these samples. The GM signal samples were produced in the mass range 200 to 900 GeV with $\sin(\theta_H) = 0.5$. Information about these samples are summarised in Table I.III. As these samples contain only electronic and muonic final states, additional samples were the W decays to a tau and a tau neutrino were produced. Information about these samples are summarised in Table I.IV. For these sampled a minimum p_{T} of 15 GeV (10 GeV) of the jets (leptons) are required at generator level as well as $|\eta|$ requirements of < 5 for jets and $|\eta| < 2.7$ for leptons.

The list of SM background MC samples used for background estimate is shown in Table I.V.

DSID	Mass	Events	Filter eff.	Cross-section [fb]	k-factor
302263	250	30000	1.00	4103	1.00
302264	300	30000	1.00	2258	1.00
302265	400	30000	1.00	716.3	1.00
302266	500	30000	1.00	283.9	1.00
302267	600	30000	1.00	132.2	1.00
302268	700	18000	1.00	69.23	1.00
302269	800	25000	1.00	39.41	1.00
302270	900	30000	1.00	23.80	1.00
302271	1000	45000	1.00	15.09	1.00
302272	1100	18000	1.00	9.921	1.00
302273	1200	30000	1.00	6.751	1.00
302274	1300	10000	1.00	4.676	1.00
302275	1400	30000	1.00	3.313	1.00
302276	1500	29000	1.00	2.391	1.00
302277	1600	30000	1.00	1.749	1.00
302278	1700	28000	1.00	1.298	1.00
302279	1800	30000	1.00	0.9720	1.00
302280	1900	30000	1.00	0.7350	1.00
302281	2000	18000	1.00	0.5610	1.00
302282	2200	35000	1.00	0.3334	1.00
302283	2400	45000	1.00	0.2028	1.00
302284	2600	30000	1.00	0.1258	1.00
302285	2800	29000	1.00	0.07925	1.00
302286	3000	20000	1.00	0.05036	1.00
302287	3500	25000	1.00	0.01700	1.00
302288	4000	30000	1.00	0.00600	1.00
302289	4500	25000	1.00	0.00200	1.00
302290	5000	30000	1.00	0.00100	1.00

TABLE I.I: Summary of HVT signal MC simulation.

DSID	Mass	Events	Filter eff.	Cross-section [fb]	k-factor
307730	250	49000	1.00	24.196	1.00
307731	300	50000	1.00	10.54	1.00
309528	350	39000	1.00	4.484	1.00
307732	400	49000	1.00	2.30	1.00
309529	450	40000	1.00	1.310	1.00
307733	500	49000	1.00	0.7975	1.00
307734	600	47000	1.00	0.3408	1.00
307735	700	50000	1.00	0.1663	1.00
307736	800	50000	1.00	0.088	1.00
307737	900	47000	1.00	0.04986	1.00
307738	1000	49000	1.00	0.02961	1.00
307739	1100	48000	1.00	0.01814	1.00
307740	1200	48000	1.00	0.01171	1.00
307741	1300	50000	1.00	0.007622	1.00
307742	1400	49000	1.00	0.005076	1.00
307743	1500	49000	1.00	0.003449	1.00
307744	1600	50000	1.00	0.002391	1.00
307745	1700	50000	1.00	0.001673	1.00
307746	1800	50000	1.00	0.001192	1.00
307747	1900	50000	1.00	0.0008536	1.00
307748	2000	50000	1.00	0.0006183	1.00

TABLE I.II: Summary of HVT signal MC simulation for the VBS analysis.

DSID	Mass	Events	Filter eff.	Cross-section [fb]	k-factor
305028	200	40000	1.00	7.0596	1.00
309501	250	40000	0.77361	7.71	1.00
305029	300	40000	1.00	3.9238	1.00
309501	350	40000	0.77472	4.582	1.00
305030	400	40000	1.00	2.4428	1.00
309501	450	40000	0.78052	3.275	1.00
305031	500	40000	1.00	1.6113	1.00
305032	600	40000	1.00	1.1005	1.00
305033	700	40000	1.00	0.77398	1.00
305034	800	40000	1.00	0.55433	1.00
305035	900	40000	1.00	0.40394	1.00

TABLE I.III: Summary of GM signal MC simulations with electron and muon final states for the VBS analysis. The mass points 250, 350 and 450 GeV also contain the $ll\tau\nu_\tau$ final states.

DSID	Mass	Events	Filter eff.	Cross-section [fb]	k-factor
307181	200	45000	0.3296	3.521	1.00
307182	300	42000	0.3486	2.149	1.00
307183	400	42000	0.3544	1.356	1.00
307184	500	45000	0.3495	0.802	1.00
307185	600	45000	0.3541	0.5888	1.00
307186	700	45000	0.3613	0.3853	1.00
307187	800	44000	0.3582	0.2775	1.00
307188	900	45000	0.3581	0.2570	1.00

TABLE I.IV: Summary of GM signal MC simulations with $ll\tau\nu_\tau$ final states for the VBS analysis.

DSID	Process	Generators	PDF	Events	Filter eff.	Cross-section [pb]	k-factor
361601	$WZ \to \ell\nu\ell\ell$	Powheg+Pythia8	NLO CT10	4890000	1.00	4.5023	1.00
363999	$WZ \to \ell\nu\ell\ell$	Powheg+Herwig	NLO CT10	1000000	1.00	2.0	1.00
364253	$WZ \to \ell\nu\ell\ell$	Sherpa 2.2.2	NNPDF30NNLO	5485580	1.00	4.583	1.00
364284	WZ VBS EW : $WZ \to \ell\nu\ell\ell$	Sherpa 2.2.2	NNPDF30NNLO	16M	1.00	0.047	1.0
364499	WZ VBS EW : $WZ \to \ell\nu\ell\ell$	MadGraph+Pythia8	NNPDF30NLO	500000	1.00	0.059	1.0
361603	$q\bar{q} \to ZZ \to \ell\ell\ell\ell$	Powheg+Pythia8	NLO CT10	3920000	1.00	1.2673	1.08
361604	$q\bar{q} \to ZZ \to \ell\ell\nu\nu$	Powheg+Pythia8	NLO CT10	981000	1.00	0.92498	1.08
361073	$gg \to \ell\ell\ell\ell$	Sherpa	CT10	502000	1.00	0.020931	$1.67 \cdot 0.91$
361106	$Z \to ee$	Powheg+Pythia8	CTEQ6L1	19916520	1.00	1901.2	1.026
361107	$Z \to \mu\mu$	Powheg+Pythia8	CTEQ6L1	19916520	1.00	1901.2	1.026
361108	$Z \to \tau\tau$	Powheg+Pythia8	CTEQ6L1	19197457	1.00	1901.2	1.026
361100	$W^+ \to e\nu$	Powheg+Pythia8	CTEQ6L1	29878800	1.00	11278.0	1.0198
361101	$W^+ \to \mu\nu$	Powheg+Pythia8	CTEQ6L1	29892400	1.00	11299.0	1.0179
361102	$W^+ \to \tau\nu$	Powheg+Pythia8	CTEQ6L1	29837800	1.00	11306.0	1.0172
361103	$W^- \to e\nu$	Powheg+Pythia8	CTEQ6L1	19902600	1.00	8290.8	1.0348
361104	$W^- \to \mu\nu$	Powheg+Pythia8	CTEQ6L1	19948400	1.00	8287.1	1.0352
361105	$W^- \to \tau\nu$	Powheg+Pythia8	CTEQ6L1	19951400	1.00	8282.6	1.0358
301535	$Z\gamma \to ee\gamma$ ($10 < p_{\mathrm{T}}^{\gamma} < 35$)	Sherpa	CT10	4957800	1.00	52.706	1.00
301899	$Z\gamma \to ee\gamma$ ($35 < p_{\mathrm{T}}^{\gamma} < 70$)	Sherpa	CT10	500000	1.00	5.242	1.00
301900	$Z\gamma \to ee\gamma$ ($70 < p_{\mathrm{T}}^{\gamma} < 140$)	Sherpa	CT10	246400	1.00	0.38455	1.00
301901	$Z\gamma \to ee\gamma$ ($p_{\mathrm{T}}^{\gamma} > 140$)	Sherpa	CT10	250000	1.00	0.047209	1.00
301536	$Z\gamma \to \mu\mu\gamma$ ($10 < p_{\mathrm{T}}^{\gamma} < 35$)	Sherpa	CT10	4981400	1.00	52.708	1.00
301902	$Z\gamma \to \mu\mu\gamma$ ($35 < p_{\mathrm{T}}^{\gamma} < 70$)	Sherpa	CT10	498600	1.00	5.2455	1.00
301903	$Z\gamma \to \mu\mu\gamma$ ($70 < p_{\mathrm{T}}^{\gamma} < 140$)	Sherpa	CT10	249800	1.00	0.38548	1.00
301904	$Z\gamma \to \mu\mu\gamma$ ($p_{\mathrm{T}}^{\gamma} > 140$)	Sherpa	CT10	249200	1.00	0.04724	1.00
301905	$Z\gamma \to \tau\tau\gamma$ ($35 < p_{\mathrm{T}}^{\gamma} < 70$)	Sherpa	CT10	499000	1.00	5.249	1.00
301906	$Z\gamma \to \tau\tau\gamma$ ($70 < p_{\mathrm{T}}^{\gamma} < 140$)	Sherpa	CT10	249800	1.00	0.38482	1.00
301907	$Z\gamma \to \tau\tau\gamma$ ($p_{\mathrm{T}}^{\gamma} > 140$)	Sherpa	CT10	249000	1.00	0.047025	1.00
301908	$Z\gamma \to \nu\nu\gamma$ ($35 < p_{\mathrm{T}}^{\gamma} < 70$)	Sherpa	CT10	498400	1.00	4.0365	1.00
301909	$Z\gamma \to \nu\nu\gamma$ ($70 < p_{\mathrm{T}}^{\gamma} < 140$)	Sherpa	CT10	249000	1.00	0.97151	1.00
301910	$Z\gamma \to \nu\nu\gamma$ ($p_{\mathrm{T}}^{\gamma} > 140$)	Sherpa	CT10	248600	1.00	0.17115	1.00
410000	$t\bar{t}$ ($\geqslant 1\ell$)	Powheg+Pythia6	NLO CT10	19958779	0.543	696.11	1.1949
410066	$t\bar{t}W + 0p$	Madgraph+Pythia8	NNPDF23LO	1992400	1.00	0.17656	1.25
410067	$t\bar{t}W + 1p$	Madgraph+Pythia8	NNPDF23LO	1943800	1.00	0.14062	1.25
410068	$t\bar{t}W + 2p$	Madgraph+Pythia8	NNPDF23LO	999200	1.00	0.13680	1.25
410111	$t\bar{t}ee + 0p$	Madgraph+Pythia8	NNPDF23LO	299600	1.00	0.0096235	1.35
410112	$t\bar{t}ee + 1p$	Madgraph+Pythia8	NNPDF23LO	299700	1.00	0.017344	1.35
410113	$t\bar{t}\mu\mu + 0p$	Madgraph+Pythia8	NNPDF23LO	300000	1.00	0.0096462	1.35
410114	$t\bar{t}\mu\mu + 1p$	Madgraph+Pythia8	NNPDF23LO	300000	1.00	0.017361	1.35
410115	$t\bar{t}\tau\tau + 0p$	Madgraph+Pythia8	NNPDF23LO	299700	1.00	0.0098874	1.35
410116	$t\bar{t}\tau\tau + 1p$	Madgraph+Pythia8	NNPDF23LO	299200	1.00	0.017790	1.35
410049	tZ (3ℓ)	Madgraph+Pythia6		995000	1.0	0.0090636	1.0
410011	t (t-channel)	Powheg+Pythia6	NLO CT10	4988200	1.0	43.739	1.0094
410012	$\bar{t}$ (t-channel)	Powheg+Pythia6	NLO CT10	4989800	1.0	25.778	1.0193
410015	Wt (2ℓ)	Powheg+Pythia6	NLO CT10	997200	1.0	3.5835	1.054
410016	$W\bar{t}$ (2ℓ)	Powheg+Pythia6	NLO CT10	997600	1.0	3.5814	1.054
410025	t (s-channel) ($\geqslant 1\ell$)	Powheg+Pythia6	NLO CT10	997800	1.0	2.0517	1.6806
410026	$\bar{t}$ (s-channel) ($\geqslant 1\ell$)	Powheg+Pythia6	NLO CT10	997400	1.0	1.2615	1.7088
361620	$WWW \to 3\ell 3\nu$	Sherpa	CT10	59800	1.00	0.008343	1.00
361621	$WWZ \to 4\ell 2\nu$	Sherpa	CT10	59600	1.00	0.001734	1.00
361622	$WWZ \to 2\ell 4\nu$	Sherpa	CT10	59800	1.00	0.0034299	1.00
361623	$WZZ \to 5\ell 1\nu$	Sherpa	CT10	49800	1.00	0.00021783	1.00
361624	$WZZ \to 3\ell 3\nu$	Sherpa	CT10	49800	0.44444	0.0019248	1.00
361625	$ZZZ \to 6\ell 0\nu$	Sherpa	CT10	35000	1.00	1.7059e-05	1.00
361626	$ZZZ \to 4\ell 2\nu$	Sherpa	CT10	34600	0.22542	0.00044125	1.00
361627	$ZZZ \to 2\ell 4\nu$	Sherpa	CT10	35000	0.44815	0.0004453	1.00

TABLE I.V: Summary of background MC samples.

Annexe II

Control plots of events in the VBF signal region with invariant mass m_{WZ} between 360< m_{WZ} <550 GeV

The events selected in the VBF signal region around the mass window of 360< m_{WZ} <550 GeV were investigated. Figures II.1 to II.14 show different kinematic distributions for the leptons in the events and the bosons reconstructed with them, split per decay channel. All the backgrounds shown in the figures are estimated using MC and only statistical uncertainties are shown.

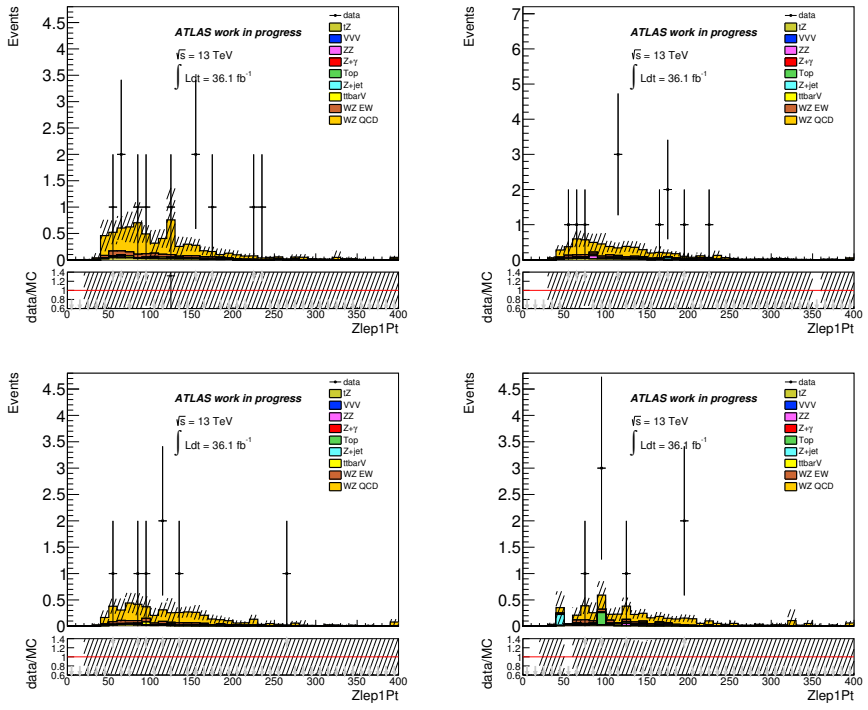

FIGURE II.1: Distributions of the Z leading lepton p_{T} for the $\mu\mu\nu\mu$ top left, $\mu\mu\nu e$ top right, $ee\nu\mu$ bottom left and $eee\nu e$ bottom right decay channels.

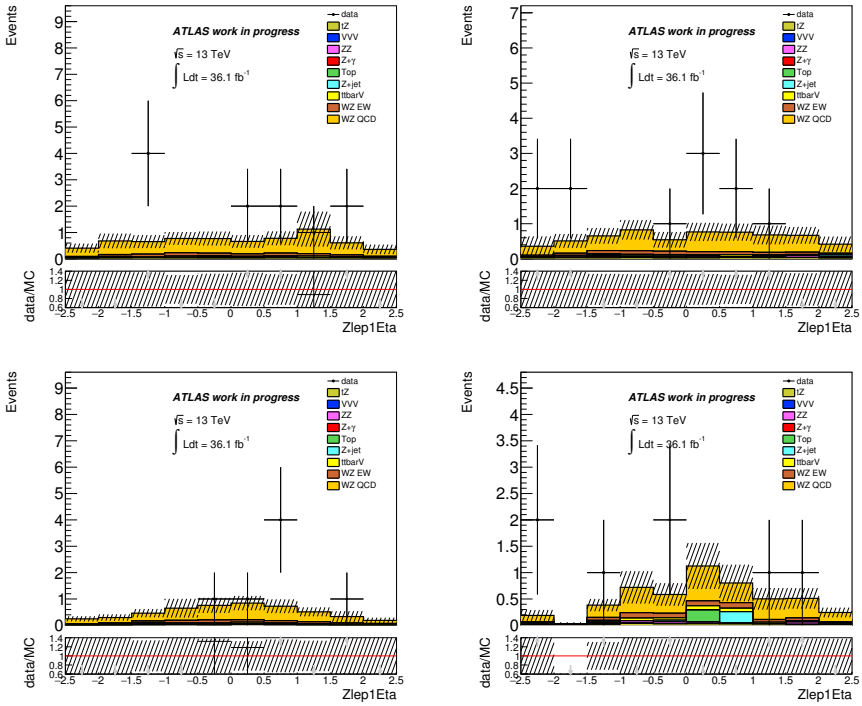

FIGURE II.2: Distributions of the Z leading lepton η for the $\mu\mu\nu\mu$ top left, $\mu\mu\nu e$ top right, $ee\nu\mu$ bottom left and $eee\nu e$ bottom right decay channels.

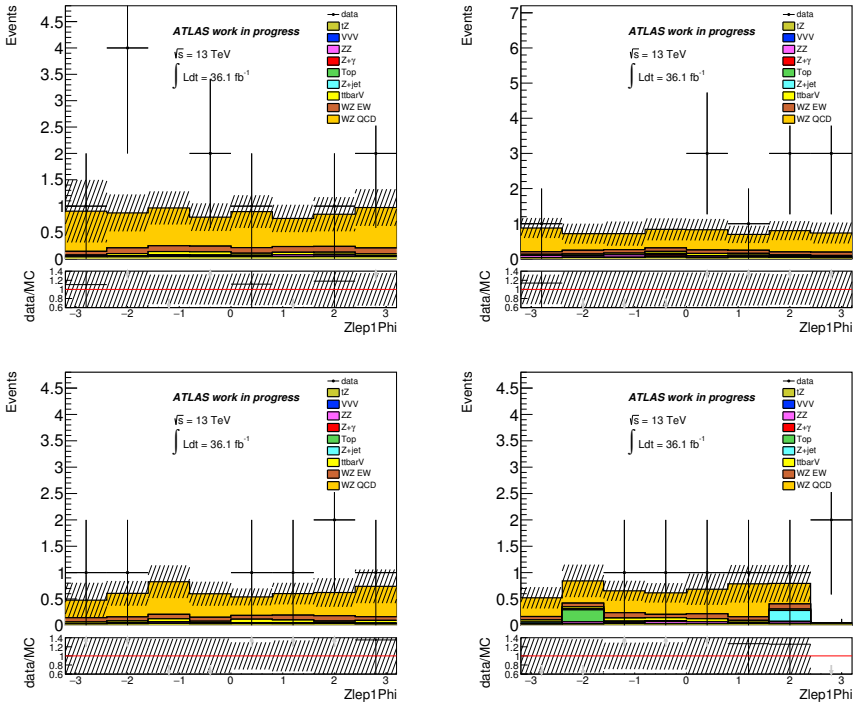

FIGURE II.3: Distributions of the Z leading lepton Φ for the $\mu\mu\nu\mu$ top left, $\mu\mu\nu e$ top right, $ee\nu\mu$ bottom left and $eee\nu e$ bottom right decay channels.

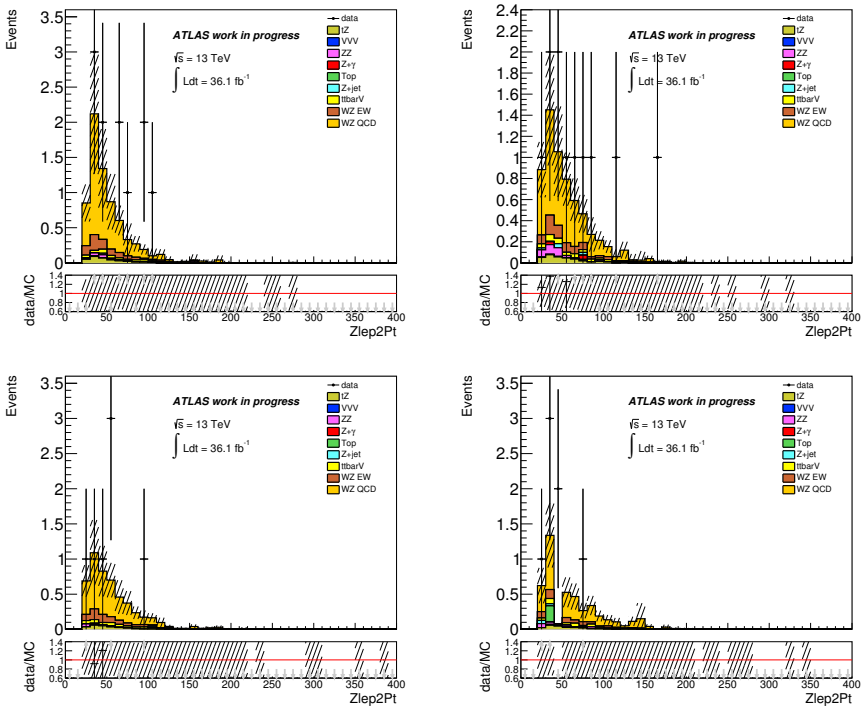

FIGURE II.4: Distributions of the Z sub-leading lepton p_{T} for the $\mu\mu\nu\mu$ top left, $\mu\mu\nu e$ top right, $ee\nu\mu$ bottom left and $ee\nu e$ bottom right decay channels.

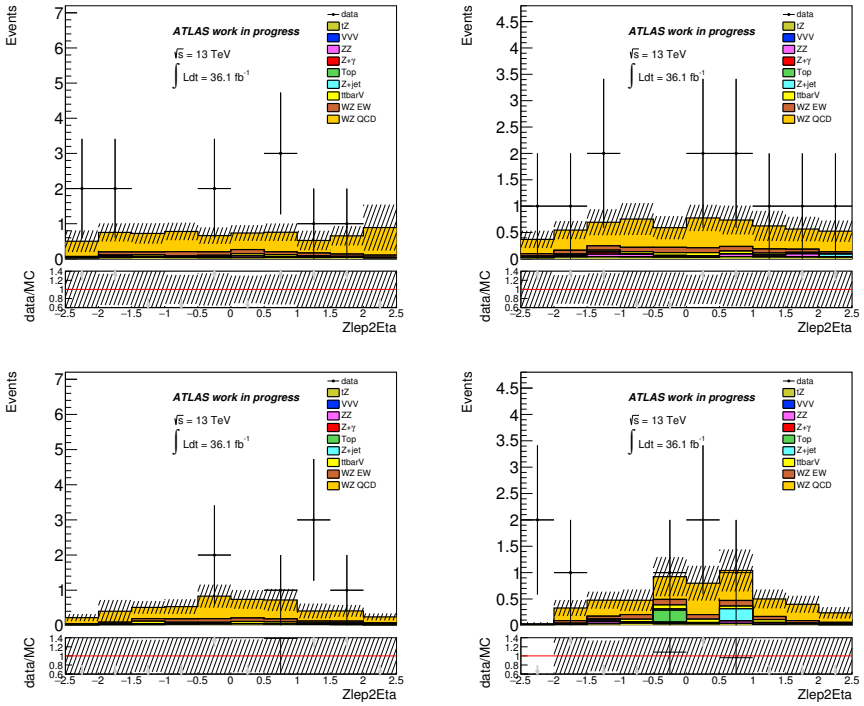

FIGURE II.5: Distributions of the Z sub-leading lepton η for the $\mu\mu\nu\mu$ top left, $\mu\mu\nu e$ top right, $ee\nu\mu$ bottom left and $ee\nu e$ bottom right decay channels.

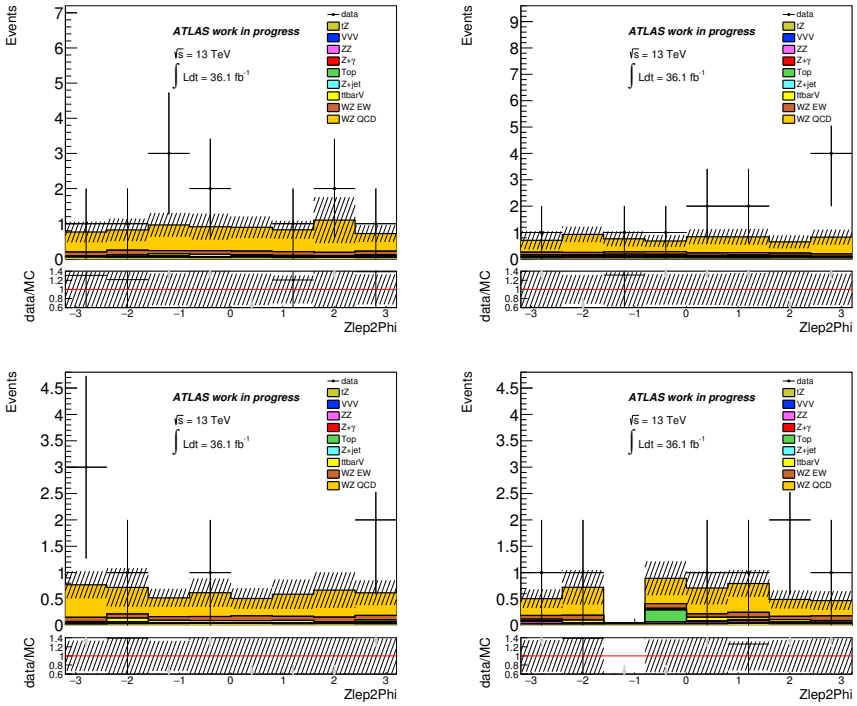

FIGURE II.6: Distributions of the Z sub-leading lepton Φ for the $\mu\mu\nu\mu$ top left, $\mu\mu\nu e$ top right, $ee\nu\mu$ bottom left and $ee\nu e$ bottom right decay channels.

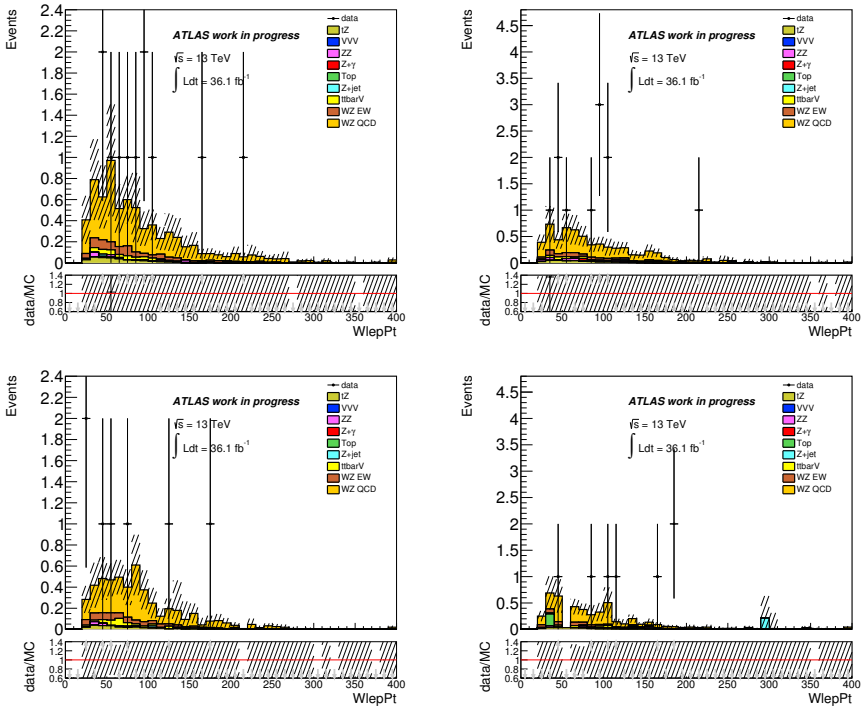

FIGURE II.7: Distributions of the W lepton p_{T} for the $\mu\mu\nu\mu$ top left, $\mu\mu\nu e$ top right, $ee\nu\mu$ bottom left and $ee\nu e$ bottom right decay channels.

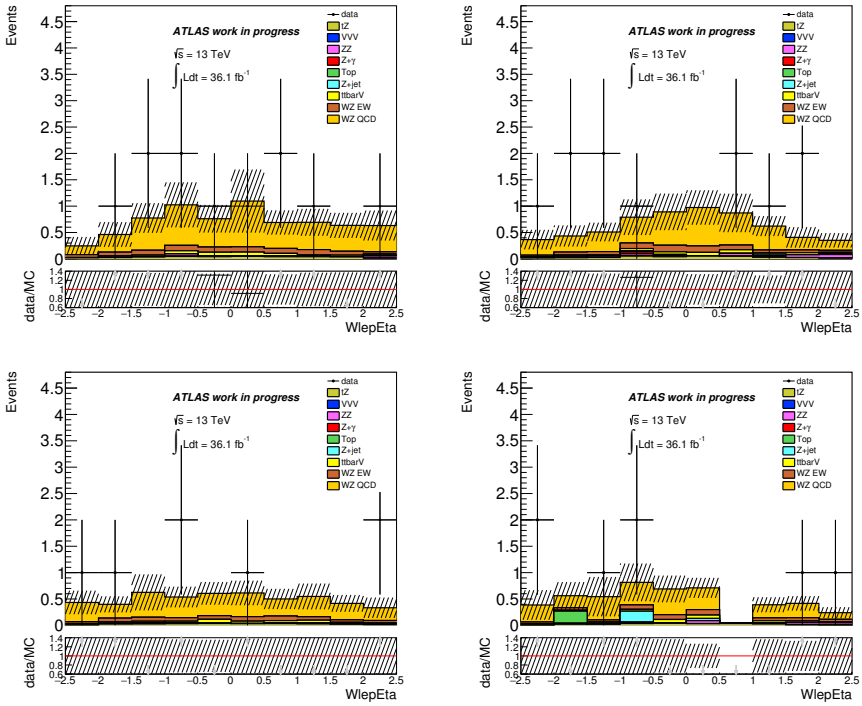

FIGURE II.8: Distributions of the W lepton η for the $\mu\mu\nu\mu$ top left, $\mu\mu\nu e$ top right, $ee\nu\mu$ bottom left and $ee\nu e$ bottom right decay channels.

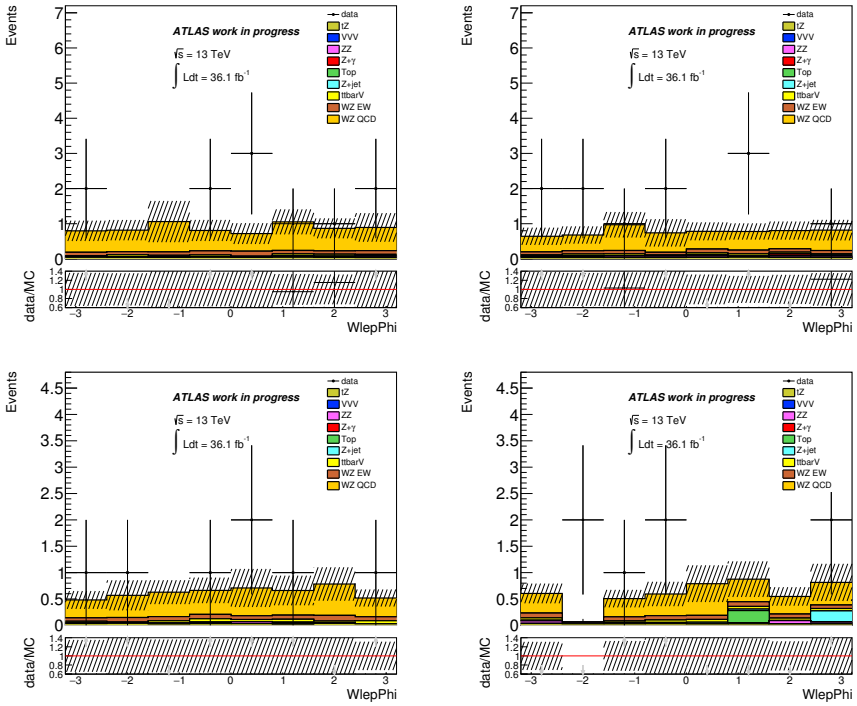

FIGURE II.9: Distributions of the W lepton Φ for the $\mu\mu\nu\mu$ top left, $\mu\mu\nu e$ top right, $ee\nu\mu$ bottom left and $ee\nu e$ bottom right decay channels.

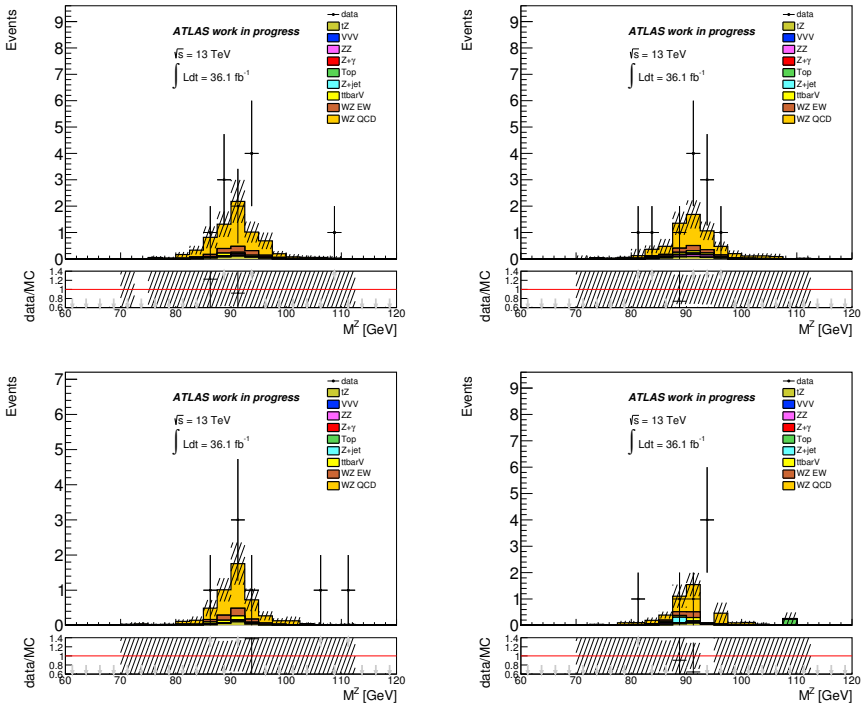

FIGURE II.10: Distributions of the Z boson invariant mass for the $\mu\mu\nu\mu$ top left, $\mu\mu\nu e$ top right, $ee\nu\mu$ bottom left and $ee\nu e$ bottom right decay channels.

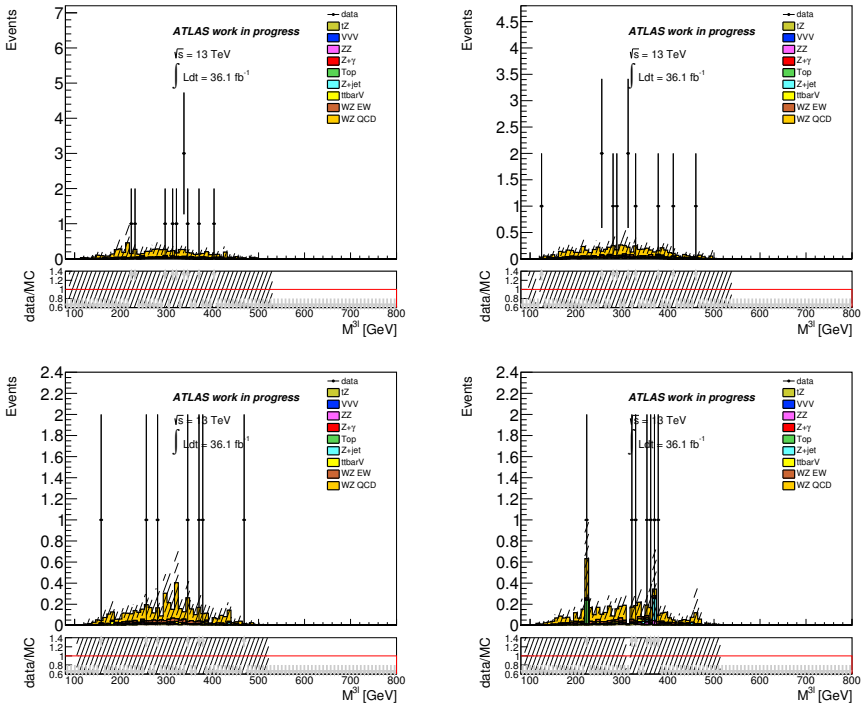

FIGURE II.11: Distributions of the three lepton invariant mass for the $\mu\mu\nu\mu$ top left, $\mu\mu\nu e$ top right, $ee\nu\mu$ bottom left and $ee\nu e$ bottom right decay channels.

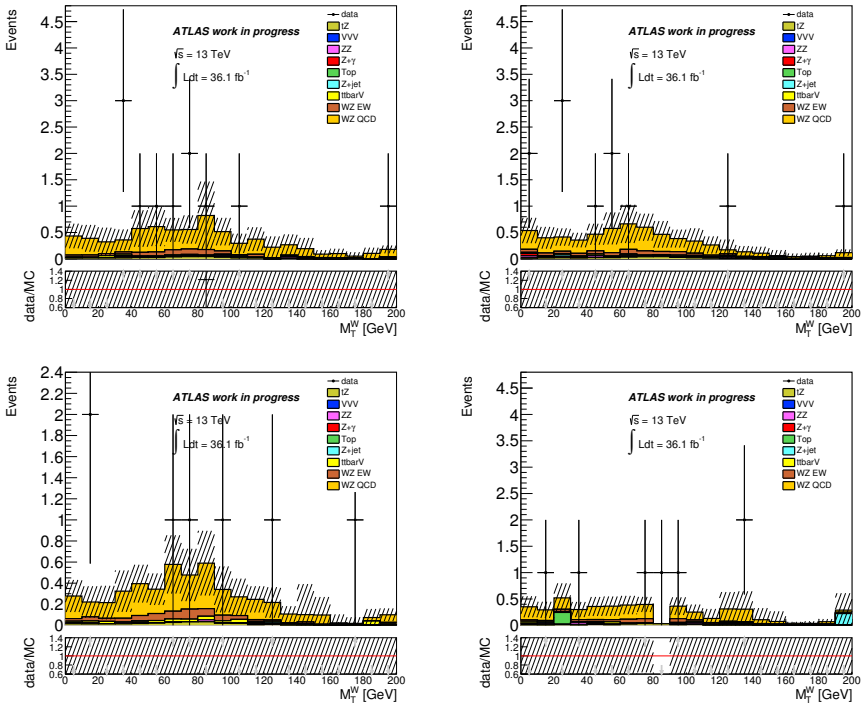

FIGURE II.12: Distributions of the W boson transverse mass for the $\mu\mu\nu\mu$ top left, $\mu\mu\nu e$ top right, $ee\nu\mu$ bottom left and $ee\nu e$ bottom right decay channels.

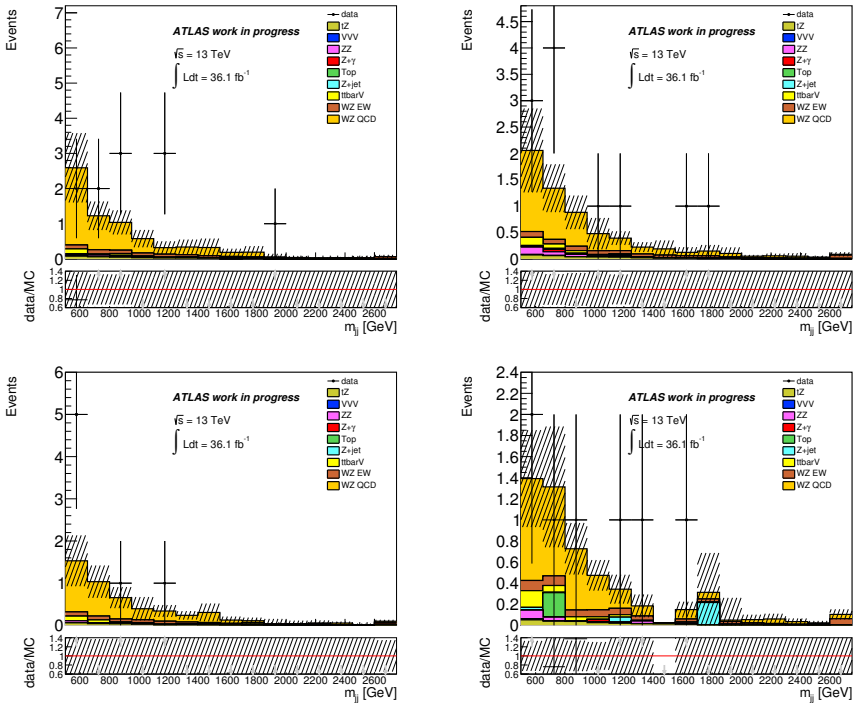

FIGURE II.13: Distributions of the di-jet invariant mass for the $\mu\mu\nu\mu$ top left, $\mu\mu\nu e$ top right, $ee\nu\mu$ bottom left and $ee\nu e$ bottom right decay channels.

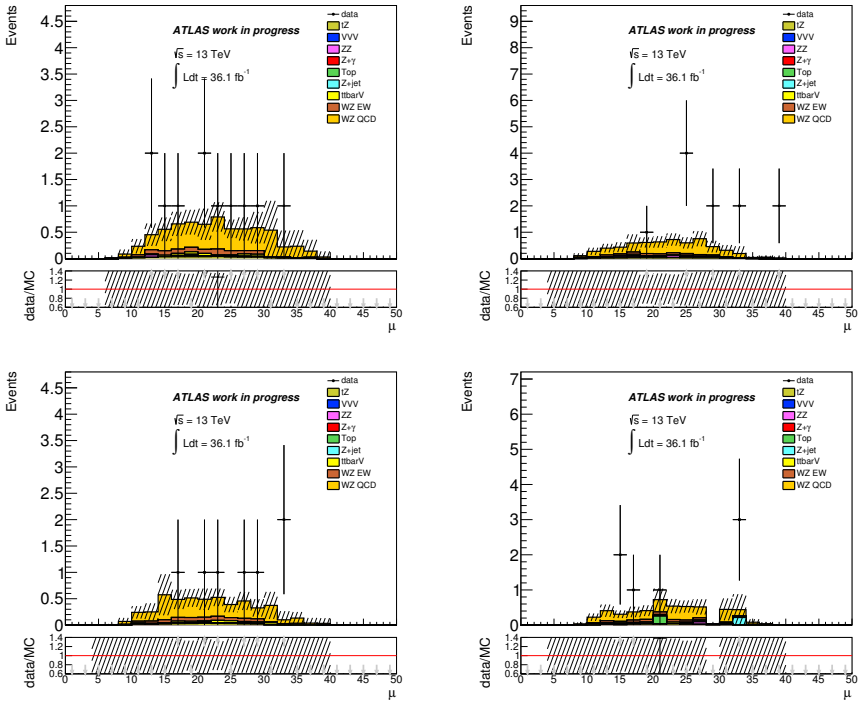

FIGURE II.14: Distributions of the average number of interactions per bunch crossing for the $\mu\mu\nu\mu$ top left, $\mu\mu\nu e$ top right, $ee\nu\mu$ bottom left and $eee\nu$ bottom right decay channels.